

FABRICATION AND TESTING OF DUAL-WAVELENGTH PHOTON SIEVES

By

HSIU-HSIN CHUNG

A DISSERTATION PRESENTED TO THE GRADUATE SCHOOL
OF THE UNIVERSITY OF FLORIDA IN PARTIAL FULFILLMENT
OF THE REQUIREMENTS FOR THE DEGREE OF
DOCTOR OF PHILOSOPHY

UNIVERSITY OF FLORIDA

2006

Copyright 2005

by

Hsiu-hsin Chung

This document is dedicated to my parents and my loving husband.

ACKNOWLEDGMENTS

First of all I would like to thank my advisor, Dr. Paul Holloway, for his guidance, encouragement, and perseverance in seeing this project to its completion. I would also like to thank Dr. Rolf Hummel, Dr. Wolfgang Sigmund, Dr. Anthony Brenann and Dr. David Tanner for being my committee and for their valuable advice.

I would like to thank Dr. Mark Davison for his technical guidance and Dr. O. Shenderova for simulation input. I would like to acknowledge the Major Analytical and Instrumentation Center (MAIC) staff for their training on instruments. A special thank you is due to Kwangje Woo, for his help in photon sieve property characterizations.

I would like to thank all the members of Dr. Holloway's group for their help and kindness. Many thanks go to Narada Bradman for his great help, inspiring discussions, and mental support. All the work in process development presented in my dissertation is a result of the collaboration with Narada. I would also like to thank Philip Chung for his warm friendship and editorial comments during the writing of this dissertation. Of course I could not forget Ludie, who always cheers me up at the awful moments of my life during the past four years.

I would like to thank my wonderful parents, who love and support me without any condition my entire life. Finally I would like to thank my husband, Yusuf, for his tremendous support, encouragement, and kindness. Without him being on my side, I would not have made it to this point in my life.

TABLE OF CONTENTS

	<u>page</u>
ACKNOWLEDGMENTS	4
LIST OF TABLES	viii
LIST OF FIGURES	ix
ABSTRACT	xiv
CHAPTER	
1 INTRODUCTION	1
2 LITERATURE REVIEW	3
2.1 Refraction vs. Diffraction	3
2.2 Diffraction Theories	5
2.2.1 Huygens Principle, Huygens-Fresnel Principle, and Obliquity Factor	5
2.2.2 Fraunhofer Diffraction	8
2.2.2.1 Single slit and double slit	8
2.2.2.2 Airy pattern – Fraunhofer diffraction from a circular aperture	9
2.2.3 Fresnel Diffraction	11
2.3 Frenel Zone Plate (FZP)	14
2.3.1 Resolution of Image System and Zone Plates	16
2.3.2 Secondary Maxima for Fresnel Zone Plates	17
2.3.3 Amplitude versus Phase Zone Plate	18
2.4 Photon Sieve	21
2.4.1 Advantages of Photon Sieves over Fresnel Zone Plates	23
2.4.1.1 Suppress higher diffraction order and improve focus	23
2.4.1.2 Overcoming the limitation of the resolution of FZP	25
2.4.2 Disadvantage of Photon Sieves over Fresnel Zone Plates	27
2.4.3 Apodization	28
2.4.4 Applications of Photon Sieves	30
2.5 Chromatic Aberration	31
2.6 Justification of Research	32
3 PHOTON SIEVE FABRICATION	33
3.1 Introduction	33

3.2	Process Development.....	34
3.2.1	Substrate Preparation.....	36
3.2.2	Film Deposition.....	37
3.2.2.1	E-beam evaporator: system and operation.....	37
3.2.2.2	Deposition controller.....	42
3.2.3	Resist Coating.....	43
3.2.3.1	Electron-beam resists.....	43
3.2.3.2	Spin-coating.....	44
3.2.4	Pattern Formation.....	48
3.2.5	Reactive Ion Etch (RIE).....	50
3.2.6	Various Process Methods: Procedures and Results.....	51
3.2.6.1	Reversed image etching.....	51
3.2.6.2	Lift-off.....	58
3.2.6.3	Direct wet etching.....	61
3.2.6.4	Direct dry etching.....	63
3.3	Discussions.....	65
4	PHOTON SIEVE PROPERTIES.....	69
4.1	Introduction.....	69
4.2	Simulation of Photon Sieves Properties.....	70
4.2.1	Focal Length and Lens Diameter.....	70
4.2.2	K-factor.....	71
4.2.3	Apodized vs. Unapodized Photon Sieves.....	71
4.3	Photon Sieve Pattern Generation.....	74
4.3.1	Single-wavelength Photon Sieve.....	77
4.3.2	Dual-wavelength Photon Sieve.....	78
4.4	Characterizations.....	80
4.4.1	Perkin-Elmer 16U Grating Spectrometer.....	80
4.4.2	Charge-Coupled Device (CCD) Camera.....	83
4.4.3	Focal Length Characterization.....	86
4.4.4	Full Width Half Maximum (FWHM) Characterization.....	88
4.5	Results.....	91
4.5.1	Focal Length Characterization.....	91
4.5.2	Full Width Half Maximum (FWHM) and Peak Intensity of PSFs.....	93
4.6	Discussions.....	102
4.7	Conclusions.....	111
5	CONCLUSIONS.....	114
5.1	Photon Sieve Fabrication.....	114
5.2	Photon Sieve (PS) Properties.....	115
6	FUTURE WORKS.....	118

LIST OF REFERENCES.....	120
BIOGRAPHICAL SKETCH.....	127

LIST OF TABLES

<u>Table</u>	<u>page</u>
2-1 Step profiles and their calculated diffraction efficiency	20
2-2 Equations of the apodization functions shown in Figure 2-25	29
3-1 Acronyms and abbreviations shown in Figure 3-2.....	36
3-2 Densities and Z-ratios of materials used in the experiment.	43
3-3 Experiment parameters of plasma-etching recipes for RIE process.....	51
4-1 Text file of the 6-sector dual-wavelength photon sieve.	76
4-2 Number of holes and open hole area for the 4 single-wavelength photon sieves and 6-sector.	77
4-3 FWHM and peak intensity at X- and Y-axes for each PSF measured with each of the three light spectra – 500 nm, 600 nm, and white lights.....	99

LIST OF FIGURES

<u>Figure</u>	<u>page</u>
2-1 Schematic drawing of Snell's law of refraction.....	4
2-2 Double-slit diffraction of light reflected from a double wave pattern in water	4
2-3 Illustration of Huygens' principle for spherical waves	5
2-4 Diffraction at a small aperture.....	6
2-5 The obliquity factor $K(\theta)$	7
2-6 Fraunhofer diffraction through (a) single slit (b) double slit apertures.....	8
2-7 Intensity pattern for diffraction from the double slit as shown in Figure 2-6(b).....	9
2-8 An Airy pattern recorded on a slide film and then digital-processed.....	10
2-9 Bessel function of the zeroth, first, second, etc. kind.....	11
2-10 Fresnel diffraction by a single slit.....	12
2-11 Comparison between Fresnel and Fraunhofer diffraction through a single slit	12
2-12 Cornu spiral	14
2-13 Fresnel half period zone for plane wavefront.....	14
2-14 Dark center and bright center Fresnel zone plates	15
2-15 The Rayleigh and Sparrow criteria for resolving the overlapping point images from two distant point sources	16
2-16 Secondary maxima from a zone plate	18
2-17 Kinoform Fresnel zone plates	19
2-18 Three fabrication steps result an eight-phase-level Fresnel lens.....	20
2-19 Quaternary Fresnel zone plate design and SEM image of a fabricated PZP.....	21

2-20	Schematic drawing of a photon sieve.....	21
2-21	Diagram showing point-to-point imaging with a photon sieve.....	22
2-22	A photon sieve and a FZP together with experimental and calculated results.....	24
2-23	The relation between the contribution of focal amplitude and the ratio of the pinhole diameter over underlying zone width (d/w ratio).....	26
2-24	Some commonly used apodization functions in linear scale.....	29
2-25	Maskless, zone-plate-array lithography	30
2-26	Chromatic aberration of a refractive lens.....	31
3-1	Schematic drawing of a cross-sectioned photon sieve	33
3-2	Flowchart of various processing methods.....	35
3-3	Three-state cascade DI water rinse bath with N ₂ bubblers on the wet bench	36
3-4	Schematic drawing of e-beam evaporator system.....	37
3-5	Photograph of electron-beam deposition chamber and control rack.....	38
3-6	Detailed structures inside bell jar of an e-beam evaporator	38
3-7	Silver spitting	41
3-8	Standard deposition monitor (a) and quartz crystal oscillator (b).....	43
3-9	P6700 series spin coater	45
3-10	Relationship between the spin speed and thickness	46
3-11	Optical photographs of spin coating defects	47
3-12	Photograph of the PlasmaTherm SLR770.....	50
3-13	Optical micrograph of an apodized photon sieve manufactured by reversed image etching method	52
3-14	Process flow of the “reversed image etching” method.....	53
3-15	SEM micrograph of residual dots within the pinholes after plasma etching of Ag and Ni	54
3-16	Schematic drawing of interaction volume for various electron-specimen interactions	55

3-17	Residual dots (a) SE image (b) BSE image.....	56
3-18	Indication of investigated area for Auger spectrum	57
3-19	Auger spectra from a general area with residual dots	57
3-20	Argon sputtering depth profile from the area with residual dots	58
3-21	Process flow of the “lift-off” method.....	59
3-22	Optical micrograph of a photon sieve manufactured by the lift-off method.....	60
3-23	Schematic drawing of sidewall residue.....	61
3-24	Process flow of the “direct wet etching” method.....	62
3-25	Optical micrographs of the photon sieve manufactured by direct wet etching	63
3-26	SEM micrographs of the veil-like matter at the edge of holes.....	63
3-27	A photon sieves with clean edge manufactured by direct dry etching method.....	64
3-28	Process flow of the “direct dry etching” method	65
4-1	Simulation result of the optimum K value	71
4-2	Simulated one-dimensional PSFs for apodized and unapodized photon sieves.....	72
4-3	A simulation of the PSF (a) peak intensity and (b) FWHM as a function of a and b.....	73
4-4	The DesignCAD pattern of the 6-sector dual-wavelength photon sieve.....	75
4-5	Schematic drawing of single-wavelength photon sieve patterns.....	77
4-6	Optical micrograph for the 605 single wavelength photon sieve.....	78
4-7	Schematic drawing of dual-wavelength photon sieve patterns	79
4-8	Optical micrographs of dual-wavelength photon sieves (a) 6-sector (b) 5in6-70%.80	
4-9	Schematic drawing of the modified Perkin-Elmer 16U grating spectrometer	81
4-10	The measurement result of intensity versus wavelength for the tungsten lamp used in the optical bench	82
4-11	Gratings (a) transmission amplitude grating (b) blazed reflection grating	82
4-12	An illustration of the CCD read-out mechanism.....	84

4-13 Saturated PSF	85
4-14 A sample of PSF measurement taken by WinCamD CCD camera.....	86
4-15 Schematic drawing of the relationship between object distance (S), image distance (S'), and focal length (F).....	87
4-16 A sample PSF (lens 610) to show the definition of FWHM	88
4-17 PSF of the refractive lens	90
4-18 Peak intensity of PSFs from 510 with 500 nm light obtained at various image distances	91
4-19 Focal length characterization for single-wavelength photon sieves under 500 nm and 600 nm lights	92
4-20 PSFs at focal point.....	93
4-21 Top view of PSF for photon sieves under monochromatic 600 nm light	94
4-22 Top view of PSF for photon sieves under polychromatic white light.....	95
4-23 PSFs under 600 nm light for all 13 photon sieves.....	96
4-24 PSFs under 500 nm light for all 13 photon sieves.....	97
4-25 PSFs under white light for all 13 photon sieves.....	97
4-26 FWHM and maximum intensity for photon sieves under 600 nm light.....	100
4-27 FWHM and maximum intensity for photon sieves under 500 nm light.....	100
4-28 FWHM and maximum intensity for photon sieves under white light.....	101
4-29 Shape of focal spots.....	102
4-30 Characteristic light rays of 600 nm light passed through (a) 6in5-50% and (b) 6in5-75%	104
4-31 Characteristic light rays of 600 nm light passed through PS 5in6-50%.....	105
4-32 Characteristic light rays of polychromatic white light which have passed through a PS lens of (a) 610 and (b) 510	106
4-33 Realistic sketch of the image formation for a dual-wavelength photon sieve with white light illumination	107

4-34	Comparison of FWHMs and intensities between 6in5-50% (red center PS) and 5in6-50% (blue center PS) under 500 nm and 600 nm light sources	109
4-35	The performance of photon sieves when switching the light sources from 500 nm to 600 nm.....	110

Abstract of Dissertation Presented to the Graduate School
of the University of Florida in Partial Fulfillment of the
Requirements for the Degree of Doctor of Philosophy

FABRICATION AND TESTING OF DUAL-WAVELENGTH PHOTON SIEVES

By

Hsiu-hsin Chung

May 2006

Chair: Paul H. Holloway

Major Department: Materials Science and Engineering

A photon sieve (PS) is a diffractive lens composed of pinholes distributed in a similar way to the Fresnel zones in a Fresnel zone plate lens. In this research, multiple dual-wavelength PSs are designed, fabricated and tested to determine the advantages and disadvantages of combining the diffractive elements into a single lens from two photon sieves which were designed for different wavelengths.

Both single- and dual-wavelength PSs were fabricated by first electron beam depositing a 3 nm adhesion layer of nickel, followed by a 100 nm layer of silver on a glass substrate. In the optimized procedure, the metallized substrate was then coated both with PMMA and ZEP7000, a positive electron-beam lithography resist with excellent resistance to dry-etching. After patterning of the underlying polymer and metal films, the ZEP7000 and polymer were removed to result in the pattern of pinholes in the metal layer on the substrate that constituted the photon sieve.

Multiple single- and dual-wavelength PS designs were tested using a modified Perkin-Elmer 16U grating spectrometer with a WinCamD charge-coupled device (CCD)

camera. The photon sieves were apodized and were designed to have a focal length of 50 mm, lens diameter of 3 mm, and a K-factor (ratio of hole spacing to diameter) of 1.2. The distributions of the two groups of pinholes for dual wavelength PSs were categorized as concentric and sectional designs. The point spread function (PSF) of each photon sieve was obtained using the CCD camera. The peak intensity and the full width half maximum (FWHM) of each PSF were used to evaluate the focusing ability of each photon sieve.

The measured focal lengths were in the range between 50.9 to 51.7 mm, i.e., very close to the nominal focal length of 50 mm. The FWHMs and peak intensities data demonstrated that the focusing ability of a dual-wavelength PS was degraded by about 10% and 50%, respectively, as compared to a single-wavelength PS using either polychromatic or monochromatic light. When switching between two monochromatic (500 or 600 nm) light sources, dual-wavelength PSs focused both wavelengths with limited performance, while the ability of a single-wavelength PSs to focus at the designed focal length was severely degraded at a wavelengths 100 nm or more away from the designed value (500 or 600 nm). The fact that PSs are highly dispersive for non-designed wavelengths would make them good candidates for a simple focusing filter lens for polychromatic light. Dual-wavelength PSs can be used for an imaging device that does not require the filtering of polychromatic light, but at the cost of intensity. The results from concentric dual-wavelength photon sieves also demonstrated that the pinholes located in the center zone of a photon sieve dominated the lens properties.

CHAPTER 1 INTRODUCTION

Refractive optics has long been used for imaging, especially for visible light. However, high absorption coefficients for refractive lens materials limit their use at short wavelengths. Diffractive optics, such as Fresnel zone plates, provides an effective solution for focusing short wavelength electromagnetic radiation, such as X-rays [1, 2]. In addition to the ability to focus the short wavelength light, diffractive optics also exhibits potential advantages over refractive optics such as significantly less weight and less volume.

A photon sieve is a diffractive lens composed of pinholes distributed in a similar way to the Fresnel zones. Recently, it has been shown that photon sieves can achieve a sharper focus by suppressing the secondary maxima and higher order diffraction effects [3], as compared to a Fresnel zone plate. However, the lens properties of diffractive optics are wavelength-dependent. If a photon with a wavelength different from the designated value passes through a diffractive lens, chromatic aberration will be observed. Researchers [4-6] have discussed multiple solutions to correct this chromatic aberration. Since all of the experimental corrections involve multiple lenses, no single diffraction lens is free of chromatic aberration.

The goal for this project is to study the properties of a photon sieve that is designed to focus two wavelengths simultaneously. In this research, multiple dual-wavelength photon sieves are designed, fabricated and tested to determine the advantages and disadvantages of combining the diffractive elements from two photon sieves (designed

for different wavelengths) into a single lens. A dual-wavelength photon sieve would offer significant advantages in many applications. Considering the small size and light weight, the multi-wavelength photon sieve would be ideal for unmanned aerial vehicles (UAVs), smart missiles, and construction of a fly's eye.

A background and literature review of the diffraction theory of light and a review of photon sieve and Fresnel zone plate diffractive lenses is presented in Chapter 2. In Chapter 3, the process development and four different process methods to fabricate photon sieves are outlined. Some problems and issues encountered during the photon sieve fabrication are discussed in Chapter 3 as well. The optical bench set-up, photon sieves testing and the testing results are described in Chapter 4. Finally, the conclusions and future works are presented in Chapter 5 and Chapter 6, respectively.

CHAPTER 2 LITERATURE REVIEW

Due to strong absorption of high-energy radiation, refractive lenses have been replaced by diffractive lenses for focusing X-rays. The properties of diffractive lenses are wavelength dependent. There have been many efforts [4-6] to create achromatic diffractive lens systems. However, a true single achromatic diffractive lens has not yet been achieved, including the designs in this research. The purpose of this research is to study the lens properties and to develop an understanding of the advantages and limitations of dual-wavelength photon sieves.

Photon sieves, proposed by Kipp et al in 2001 [3], are a relatively new type of diffractive lens. Since a photon sieve is a collection of pinholes distributed in Fresnel zone regions, there is an opportunity to alter the pinhole distribution patterns and to combine two groups of pinholes that can be used to focus two different wavelengths. In this review of the literature, the diffractive lens properties already explored will be reviewed and related to photon sieves. This review of the literature covers the following topics: (a) diffraction theories, (b) Fresnel zone plate, (c) photon sieve, and (d) dual-wavelength photon sieves. It is important to note that only the pertinent diffraction theories are discussed in this review, and the reader is encouraged to consult other bibliographic references in optics for more detailed studies [7-9].

2.1 Refraction vs. Diffraction

Refraction occurs when waves travel from a medium with a given refractive index into a medium with another index. The wave changes direction at the boundary between

the two media. The “point of incidence” is the point where the light ray intersects the surface. The line constructed at this point which is perpendicular to the surface is called the “surface normal.” The angle of incidence (θ_1) and angle of refraction (θ_2) are shown in Figure 2-1. According to Fermat’s principle – light travels with the shortest path – the laws of refraction can be derived, such as Snell’s law ($n_1 \sin \theta_1 = n_2 \sin \theta_2$) [7].

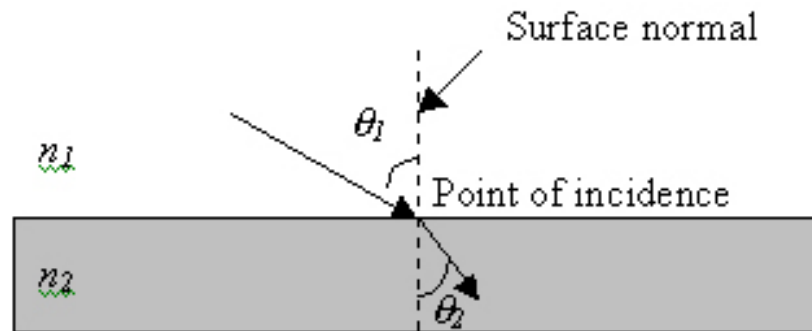


Figure 2-1. Schematic drawing of Snell’s law of refraction.

However, diffraction is the bending and spreading of waves when they meet an array of obstacles and then undergo interference. The obstacles can be either opaque or transparent since the wavefront is changed in amplitude and/or phase when diffraction occurs. A very common example would be water waves causing diffraction of reflected light by a double-slit in a ripple-tank, as shown in Figure 2-2.

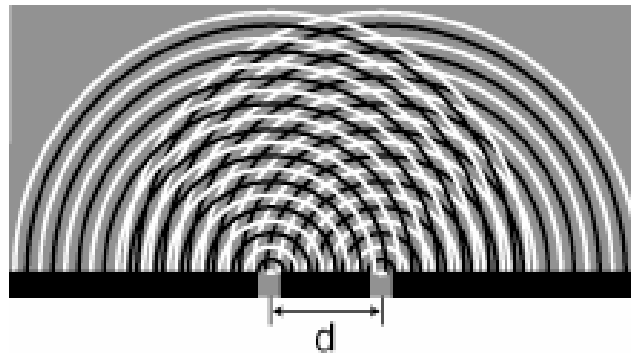


Figure 2-2. Double-slit diffraction of light reflected from a double wave pattern in water [10].

2.2 Diffraction Theories

To understand diffraction, it is first helpful to recall Huygens' principle, which explains how wave propagates, and the Huygens-Fresnel principle that explains why no back wave is formed during the wave propagation. After a brief introduction of how light propagates based on these principles, the diffraction phenomenon is then discussed.

There are two types of diffraction: Fraunhofer and Fresnel. When the light source and the observation screen are far apart and light is essentially parallel, the conditions are met for Fraunhofer diffraction, also known as far-field diffraction. If the observation screen or light source is moved close to the aperture (less than a few wavelengths), Fresnel diffraction occurs.

2.2.1 Huygens Principle, Huygens-Fresnel Principle, and Obliquity Factor

In 1678, a Dutch physicist named Christian Huygens, presented the concept of wave propagation which is known as Huygens' principle [8]. This principle states that every point on a primary wavefront serves as the source of spherical secondary wavelets such that the primary wavefront at some later time is the envelope of these wavelets [7, 11]. When a light wave propagates through free space at the speed of light, the light rays associated with this wavefront propagate in straight lines, as shown in Figure 2-3.

Huygen's principle provides the insight into the nature of wave propagation necessary to explain how wave theory can account for the laws of geometric optics.

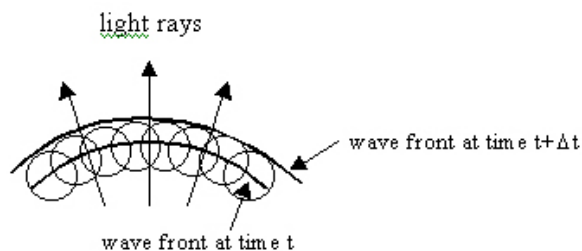


Figure 2-3. Illustration of Huygens' principle for spherical waves [11].

However, Huygens' principle does not indicate the direction of the wave propagation in time. Why does a spherical wave continue to expand outward from its source, but not re-converge inward back to the source? Augustin Jean Fresnel, a French physicist, resolved this problem in 1816 by slightly modifying the Huygens' principle [8]. The corresponding Huygens-Fresnel principle states that every unobstructed point of a wavefront serves as a source of spherical secondary wavelets, and the amplitude of the optical field at any point beyond the obstruction is the superposition of all these wavelets [9]. This principle is illustrated in Figure 2-4. Each small arrow shown in Figure 2-4 represents a phasor, which indicates the amplitude and phase of a wavelet. The amplitude observed at any point in the optical field, such as P_0 , P_1 , and P_2 , is the algebraic sum of the individual phasors. Each of the unobstructed points (black dots within the single slit width \overline{AB} in Figure 2-4) on the incoming plane wave acts as a coherent secondary source. When the wavelength of the source is larger than the aperture, the coherent waves interfere constructively and result in the bright spots at P_0 , P_1 , P_2 , etc. The larger the wavelength, the wider the wave spread out. That means if a photon counter is placed at P_0 , it will see lots of light. When the aperture is decreased in size or larger wavelength light is used, the number of photons counted at P_1 and P_2 increases even as the counts at P_0 decreases.

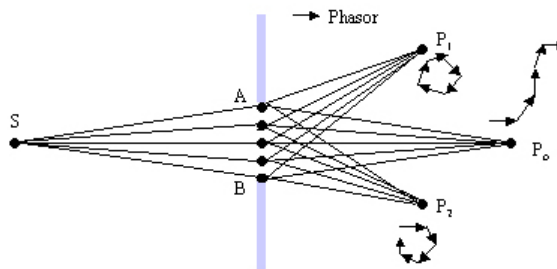


Figure 2-4. Diffraction at a small aperture. The amplitude observed at any point in the optical field is the algebraic sum of the individual phasors [9].

In 1883, Gustav Kirchhoff, a Russian theoretical physicist [12], developed a rigorous theory based on the solution of the Kirchhoff's scalar differential wave equation [9] and introduced the obliquity factor $\mathbf{K}(\theta)$ as shown below:

$$\mathbf{K}(\theta) = \frac{1}{2} (1 + \cos \theta) \quad (2-1)$$

where θ is the angle made with the normal to the primary wavefront vector \mathbf{k} . A schematic drawing of the secondary wavelets affected by the obliquity factor is shown in Figure 2-5. At point P, the wave amplitude A becomes [8]

$$A = \mathbf{K}(\theta)A_0 \quad (2-2)$$

where A_0 is the amplitude of the light source. $\mathbf{K}(\theta)$ introduces an angular dependence for the vector \mathbf{k} . At $\theta = 0$, the forward direction, the obliquity factor $\mathbf{K}(0) = 1$. At $\theta = 90^\circ$, the amplitude falls off to $\frac{1}{2}$ of the original value. At $\theta = 180^\circ$, the backward direction, $\mathbf{K}(\pi) = 0$. This factor expresses theoretically that no back wave is formed during the wave propagation.

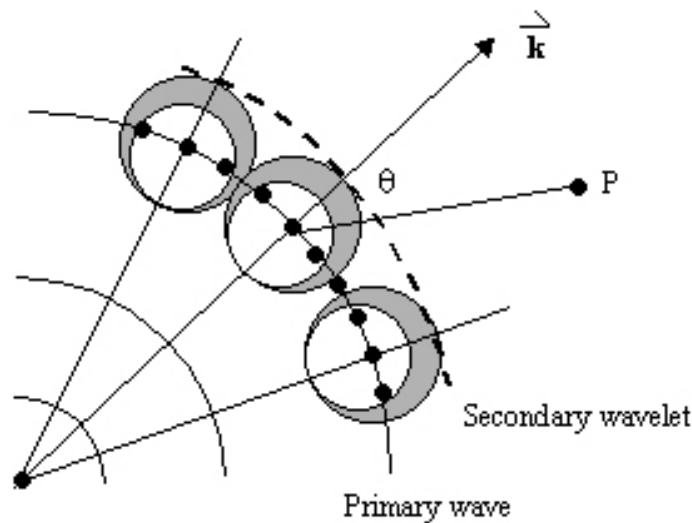


Figure 2-5. The obliquity factor $\mathbf{K}(\theta)$, the gray area, makes the amplitude of the vector \mathbf{k} vary as a function of the angle θ . $\mathbf{K}(\theta) = 0$ when $\theta = \pi$, thus no wave travels backward during the wave propagation [9].

2.2.2 Fraunhofer Diffraction

2.2.2.1 Single slit and double slit

Fraunhofer diffraction was first proposed by Joseph Fraunhofer in 1823 [9].

Consider a point source very far from a single slit aperture; thus the incident wavefront is planar. The slit width is d , and the observation screen is also far from the aperture with a distance D , shown in Figure 2-6(a) [13].

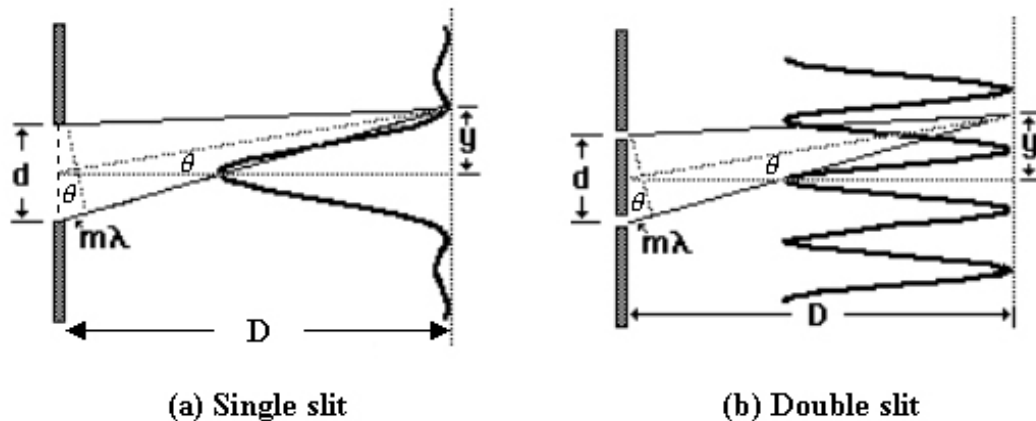


Figure 2-6. Fraunhofer diffraction through (a) single slit (b) double slit apertures [13].

Imagine that three light rays pass through the top, middle, and bottom of the slit in Figure 2-6 (a). If the paths of the top and middle rays differ by $\frac{1}{2} \lambda$ (wavelength), they will interfere destructively and cancel each other at point y . The middle and bottom rays will cancel each other because of the same condition. Consequently, if the path difference between the top and bottom rays is an integral multiple of λ , zero irradiance will be expected at point y of the observation plane. The equation for minima in Fraunhofer diffraction with a single slit can be written as [13]

$$d \sin \theta = m \lambda \quad m = \pm 1, \pm 2, \pm 3, \dots \quad (2-3)$$

When θ is zero, the light wave passes through the slit without being diffracted and forms the maximum of the intensity peak which is referred to as zeroth-order maximum (see

Figure 2-6(a)). This “undiffracted light” may cause the background noise and is discussed in Chapter 4.

However, for a double slit aperture, a λ path length difference between the path lengths of the two slits produces constructive interference; thus maximum intensities will be observed as predicted by equation (2-3) (Figure 2-6(b)). Combining the single slit diffraction and double slit interference, the final pattern for Fraunhofer diffraction on a double slit aperture is shown in Figure 2-7.

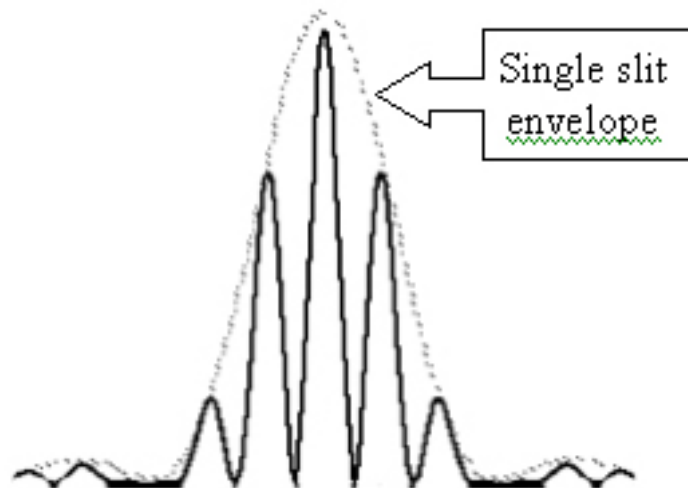


Figure 2-7. Intensity pattern for diffraction from the double slit as shown in Figure 2-6(b) [13].

2.2.2.2 Airy pattern – Fraunhofer diffraction from a circular aperture

When the slit aperture of Figure 2-6 is replaced by a circular aperture in Fraunhofer diffraction as mentioned in last section, an Airy pattern, named after George B. Airy [9], will form as a result of the diffraction phenomenon. An Airy pattern, shown in Figure 2-8, consists of a circular spot, the Airy disk, surrounded by much fainter concentric circular rings. The Airy disk or the bright center spot is called “primary maximum” and the rest of surrounded rings are called “secondary maxima” [9].

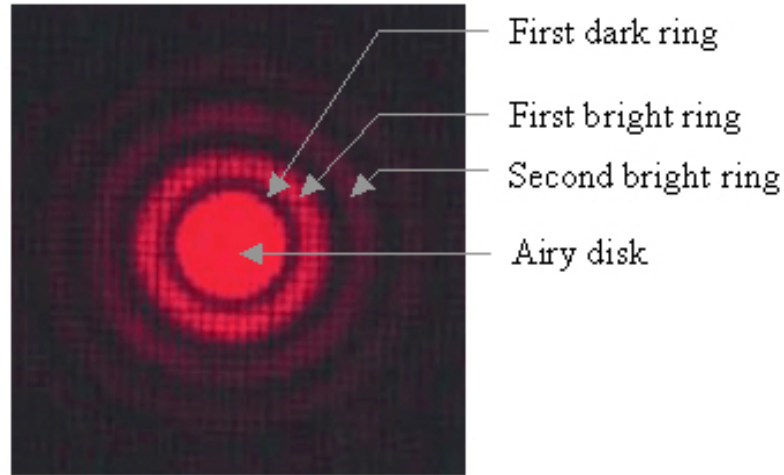


Figure 2-8. An Airy pattern recorded on a slide film and then digital-processed. The grid lines are the result of digitization [14].

The intensity distribution, $I(x)$, of the Airy pattern is written as below [9]:

$$I(x) = I(0) \left[\frac{2J_1(x)}{x} \right]^2 \quad (2-4)$$

where $I(0)$ is the intensity at the center of Airy disk, i.e., the intensity in the zeroth-order maximum, and $J_1(x)$ is the Bessel function of the first kind, shown in Figure 2-9. The x variable in $J_1(x)$ is written as [9]

$$x = \mathbf{k}dq/R \quad (2-5)$$

where \mathbf{k} is the wave vector, d is the radius of the circular aperture, q is the radius of the Airy disk and R is the distance between the aperture and observation screen. The Bessel function attenuates slowly with oscillations as x increases. $J_1(0) = 0$ and $J_1(x)/x$ approaches $\frac{1}{2}$ when x approaches 0 [9]. Since $\sin \theta = q/R$, the larger the diffraction angle (θ), i.e., the higher diffraction order (m), the higher the q/R , thus the larger the x value. From equation (2-4), the larger x value results in a smaller $I(x)$, i.e., the lower intensity. From equations (2-3) to (2-5), the diffraction intensity diminishes when the diffraction order is high.

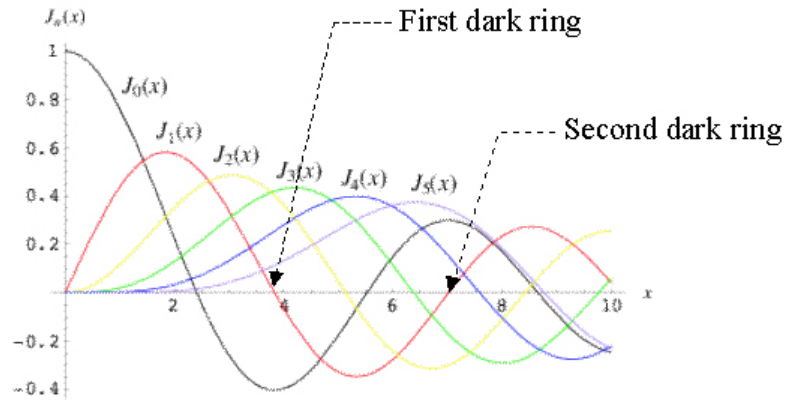


Figure 2-9. Bessel function of the zeroth, first, second, etc. kind [15]. Only the Bessel function of the first kind ($J_1(x)$, red solid curve) is used to calculate the intensity of the Airy pattern.

From Figures 2-8 and 2-9, the first dark ring corresponds to the first zero of the Bessel function, i.e., $J_1(x) = 0$ when $x = 3.83$. The radius q of the first dark ring can be equated to the boundary of the Airy disk [9]:

$$q = 1.22 R\lambda/2d \quad (2-6)$$

where R is the distance between aperture and observation screen, λ is wavelength, and d is the radius of the circular aperture. For a lens focused on the observation screen, R can be replaced with the focal length, f , of the lens.

The Airy pattern causes blurring of images from a point source. For a refractive optical system with an aperture, if the blurring is larger than that produced by aberrations (spherical, chromatic, astigmatism, etc.) of the system, the imaging process is said to be diffraction-limited and the image is the best that can be obtained with that aperture.

2.2.3 Fresnel Diffraction

Though the diffraction for the research of dual-wavelength photon sieves is categorized as Fraunhofer (far-field) diffraction, it is helpful to understand the difference between Fraunhofer and Fresnel diffractions and to distinguish the two diffractions.

Fresnel diffraction is also called near-field diffraction. It occurs when either the source or the observation screen is close to the aperture (the distance is in the range of few wavelengths) and the wavefront is essentially spherical. A schematic drawing in Figure 2-10 indicates the Fresnel diffraction geometry for a single slit aperture. The appearance of the diffraction pattern is similar to that from a Fraunhofer single slit except that the intensities at the minima are not zero. A comparison between Fresnel and Fraunhofer diffraction patterns is shown in Figure 2-11.

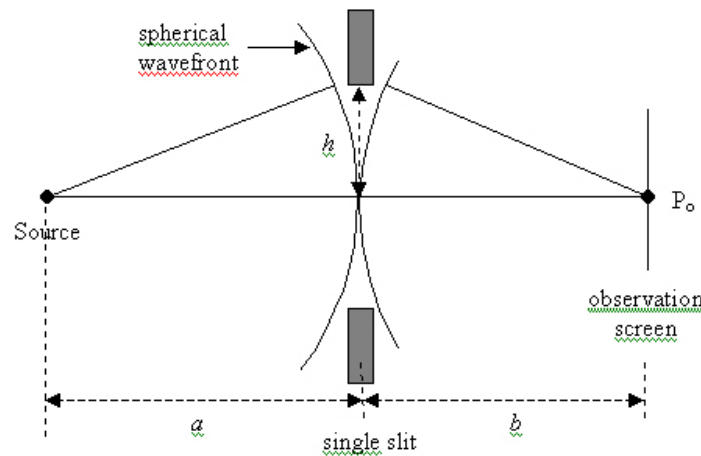


Figure 2-10. Fresnel diffraction by a single slit [8].

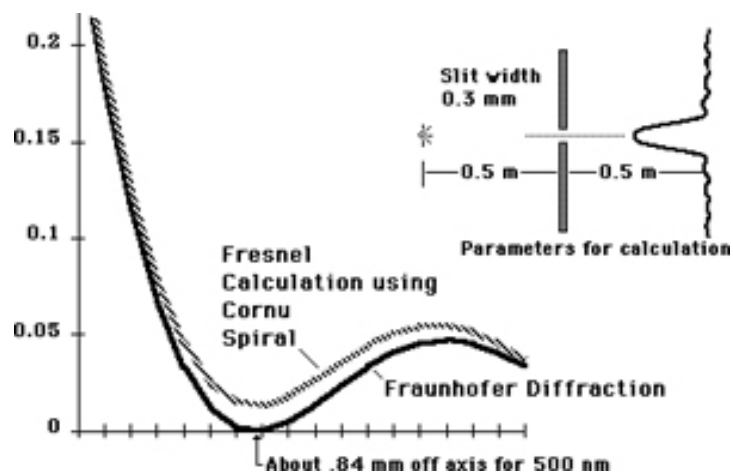


Figure 2-11. Comparison between Fresnel and Fraunhofer diffraction through a single slit. The minima in Fresnel diffraction pattern is not zero in contrast to minima in Fraunhofer diffraction [16].

The intensity, I , of Fresnel diffraction at a single slit can be written as [8]

$$I = \frac{1}{2} [ab\lambda / (a + b)] [(\int \cos \frac{1}{2} \pi v^2 dv)^2 + (\int \sin \frac{1}{2} \pi v^2 dv)^2] \quad (2-7)$$

where v is the variable of a function related to the phase difference between rays, which can be written as [8]

$$v = h \sqrt{2(a + b)/ab\lambda} \quad (2-8)$$

where λ is the wavelength, a and b (Figure 2-10) are the distances of the source to aperture and aperture to observation screen, respectively. If we assume [8]

$$x = \int \cos \frac{1}{2} \pi v^2 dv \quad (2-9)$$

$$y = \int \sin \frac{1}{2} \pi v^2 dv \quad (2-10)$$

equation (2-7) can be rewritten as

$$I = \frac{1}{2} [ab\lambda / (a + b)] (x^2 + y^2) \quad (2-11)$$

where x and y are known as Fresnel's integrals. When plotting x versus y , a spiral curve known as the Cornu spiral shown in Figure 2-12 can be obtained. The two ends of the spirals located at $(0.5, 0.5)$ and $(-0.5, -0.5)$ represent image plane points at infinity.

Depending on the Fresnel diffraction geometry, values of a , b , h , and λ will decide the value of v . At specific v , the corresponding x , y values can be found from the Cornu spiral and then the relative intensity of the Fresnel diffraction pattern can be calculated.

A dimensionless parameter, the Fresnel number (F), can be used to categorize the diffraction types. As mentioned in Figure 2-10, $F = 4h^2/b\lambda$, where h is half of the aperture width, λ is the wavelength, and b is the distance between observation plane and aperture. When $F \ll 1$, diffraction is of the Fraunhofer type; when $F \geq 1$, the diffraction regime becomes Fresnel [17].

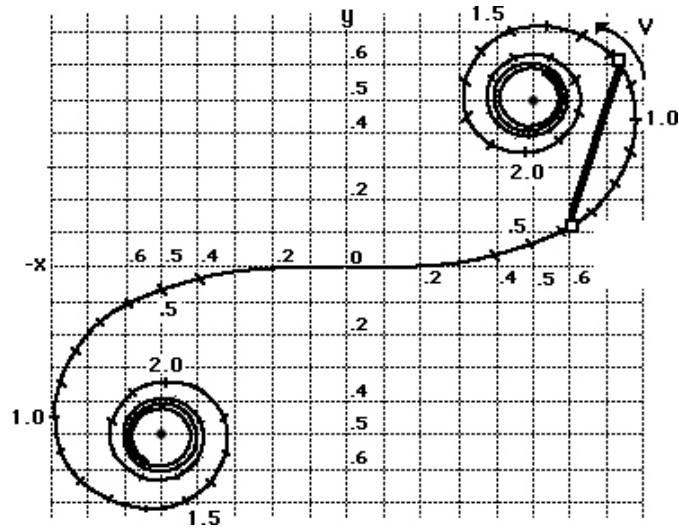


Figure 2-12. Cornu spiral. The coordinates x and y are the Fresnel's integrals [8].

2.3 Fresnel Zone Plate (FZP)

Consider a light source incident upon a circular aperture from infinity; i.e., the incident waves are planar and not spherical. After passing through the aperture (Figure 2.13), the light will reach point P_0 at a distance b , from the aperture. This circular aperture can be divided into half-period zones, where each zone is a multiple of a half wavelength away from P_0 , as shown in Figure 2-13.

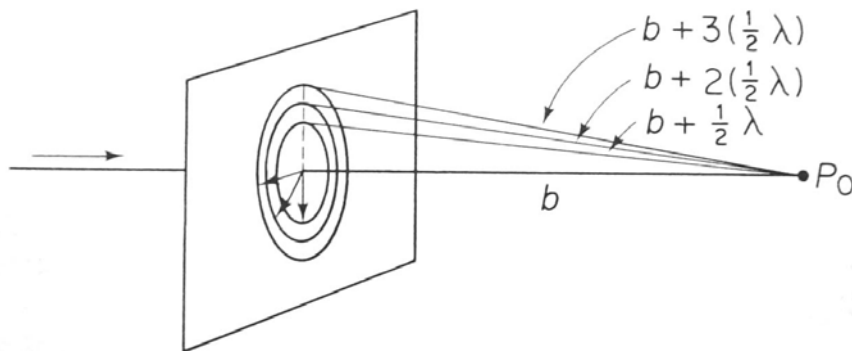


Figure 2-13. Fresnel half period zone for plane wavefront. Each zone is a half wavelength away from P_0 [8].

Thus $b + \frac{1}{2} \lambda$, $b + 2(\frac{1}{2} \lambda)$, and $b + 3(\frac{1}{2} \lambda)$ represent the boundaries of the first, second, and third zone, respectively. The radius of the m_{th} boundary (R_m) can be written as [9]

$$R_m^2 = (b + \frac{1}{2} m\lambda)^2 - b^2 \quad (2-12)$$

The area of each zone is approximately $\pi b\lambda$. However, the width of each zone (w) varies according to the radius of the zone. The intensity observed at P_o is the sum of the contribution of the wavelets originating from each zone. Because each zone is $\frac{1}{2} \lambda$ away, the contribution from the adjacent zone is opposite in phase (i.e., a phase shift of π). The light diffraction from adjacent zones will therefore cancel each other and the overall contribution at P_o is null. By eliminating the contribution from all odd or even zones, a dark or bright center Fresnel zone plate (FZP) will be obtained, respectively (see Figure 2-14). The overall intensity at P_o will be brighter as the number of zones is increased.

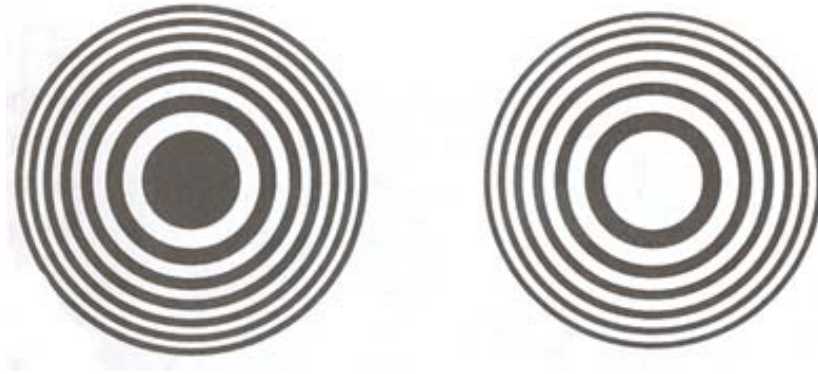


Figure 2-14. Dark center and bright center Fresnel zone plates. The dark areas are opaque to the wavelength of the light [9].

Because the incident light is from infinity, b is actually the focal length (f) and P_o is the focal point of this Fresnel lens. The primary focal length, f , is therefore [9]:

$$f = b = R_m^2 / m\lambda \quad (2-13)$$

It is apparent that the focal length depends strongly on the wavelength. For example, for a 500 nm designed FZP with a nominal focal length of 50 mm under 500 nm light, the focal length is shifted to 41.7 mm when the incident wavelength is changed to 600 nm.

This focal length shifting is verified with the testing results presented in Chapter 4.

2.3.1 Resolution of Image System and Zone Plates

The resolution of a lens is the minimum distance between two objects that can be distinguished. Considering two equal-irradiant and distant point sources passing through an aperture of an optical system, the Airy patterns formed from these two point sources are either overlapped or clearly resolved. Depending on the degree of pattern overlap, two resolution limits, Rayleigh and Sparrow criteria, can be applied, as shown in Figure 2-15. The Rayleigh criterion is applied when the center of one Airy disk falls on the first minimum of the Airy disk of another point image. When the distance between the two point sources further decreases, the central dip that appears in the Rayleigh criterion will finally disappear which is defined as the Sparrow criterion. The spatial resolution, δm , based on the Rayleigh criterion is then written as [9]

$$\delta m = 1.22 f\lambda/D \quad (2-14)$$

where f is the focal length, λ is the wavelength of light, and D is the diameter of the aperture.

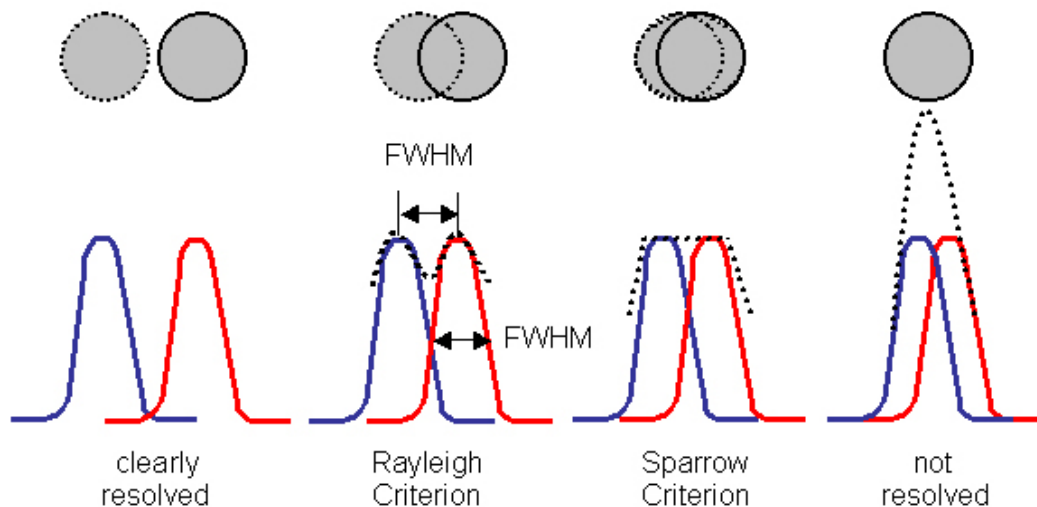


Figure 2-15. The Rayleigh and Sparrow criteria for resolving the overlapping point images from two distant point sources. The gray circles represent the Airy disks of the two point sources [9].

However, for a FZP, the resolution is controlled by the outermost zone width [3, 18, 29]. The optical resolution of a zone plate is given by [18]

$$\delta m = 1.22 \Delta r_N / m \quad (2-15)$$

where N is the outermost zone index, Δr_N is the outermost zone width and m is the diffraction order [18].

Due to the testing set-up in this research (described in section 4-4), the resolution of the photon sieves was not determined and is discussed in Chapter 4. In this research, FWHM and intensity were used to characterize the measured point spread function (PSF) and the image quality instead of determining the resolution of the photon sieves.

2.3.2 Secondary Maxima for Fresnel Zone Plates

As described above, an Airy disk is observed from Fraunhofer diffraction from a circular aperture. The intensity attenuates as predicted by the Bessel function of the first kind when light passes through a circular aperture, where the transmission abruptly becomes zero at the edge of the aperture. For a Fresnel zone plate, the amplitude contribution of each ring is equal at the focus. When this contribution drops abruptly to zero beyond the outermost ring, an oscillation of light intensity occurs just as shown in the Airy pattern (Figure 2-8). Secondary maxima is the collection of first, second, and higher order bright rings in the Airy pattern resulting from diffractions from the many concentric circular zones of a FZP. The secondary maxima will cause blurring of the image. It also increases the level of background noise and reduce the contrast of the image. The suppression of secondary maxima can be achieved by applying apodization technique which is discussed in sections 2-4-1-1 and 2-4-3. A schematic drawing of secondary maxima is shown in Figure 2-16.

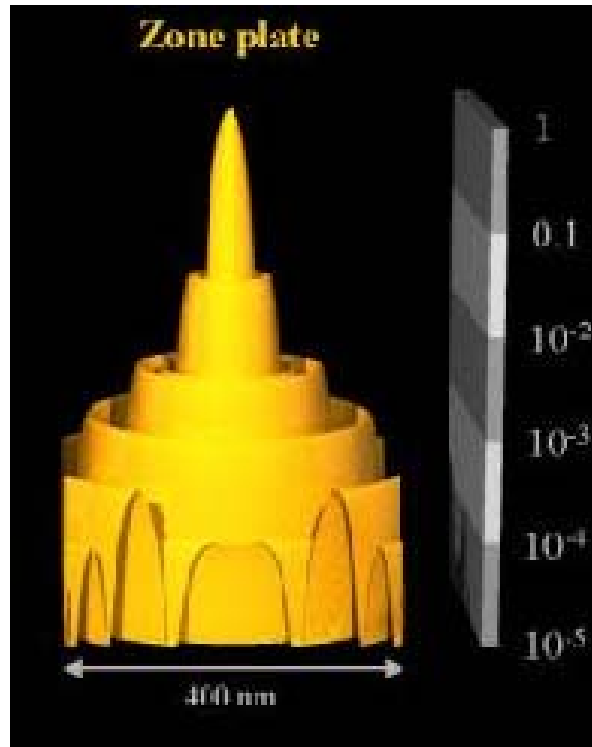


Figure 2-16. Secondary maxima from a zone plate. The vertical scale is a logarithm of intensity and the horizontal axis is the displacement from the focal point [20].

2.3.3 Amplitude versus Phase Zone Plate

The zone plate described above is called an amplitude zone plate. The light passing through all odd or even zones are blocked, which means half of the light is not transmitted. To increase transmission, Kirz et al [21] proposed a method to shift the phase of the light transmitted through the opaque regions of the FZP by using the proper thickness of a transparent material. This particular design is called a phase zone plate (PZP). Researches [22-24] combined the concepts of a phase-shift zone plate and a kinoform grating [25, 26] to create a kinoform zone plate where the original light with destructive phases were shifted by $\pm \frac{1}{2} \lambda$ (π) and resulted in a totally constructive Fresnel zone plate, as shown in Figure 2-17. The convex kinoform zone plate is equivalent to the concave type, which is the most common type.

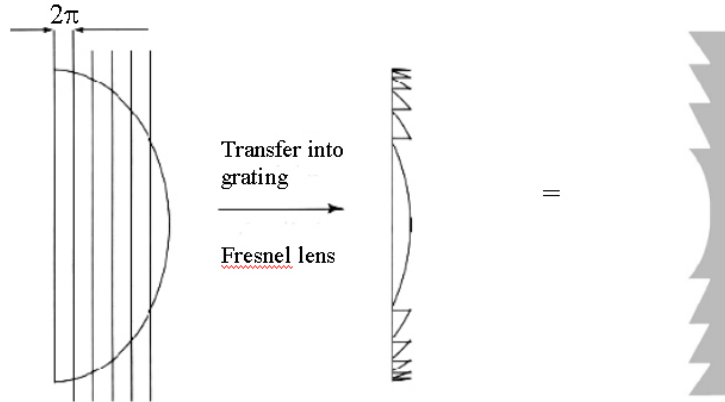


Figure 2-17. Kinoform Fresnel zone plates. The convex Fresnel lens is equivalent to the concave lens in properties. They all shift the light phase by π between the regions [22, 27].

Also in 1999, Fabrizio et al [20] utilized the same approximation of Schelokov's ideal continuous phase-shifting profile (ideal kinoform) but modified the materials of the zone plate to make it totally transmitting rather than reflecting. In order to approach the ideal kinoform profile, a stepwise function was created in the profile for each zone (see Figure 2-18, 19). The efficiency (η_m of the m^{th} diffraction order) of the Fresnel zone plate was shown to be equal to [18]

$$\eta_m = A^2/C^2 \quad (2-16)$$

where A is the observed amplitude and C is the intensity of the incoming field. This equation can be further expressed as [18]

$$\eta_m = 2 [1 - \cos(2\pi m/L)](L/m)^2 \quad (2-17)$$

where L is the number of profile steps. Table 2-1 shows the calculated diffraction efficiency with the various step-profiles of the lens. Diffraction efficiency is determined by the ratio of the power of the diffracted light beam to the incident power of the beam while the transmittance is the fraction of light at a specific wavelength that passes through a Fresnel zone plate.

Table 2-1. Step profiles and their calculated diffraction efficiency [27].

Step profile	Efficiency (%)
Theoretical (kinoform)	100
Linear	99
16-level	98.7
8-level	95
4-level	81.1
2-level	41
Amplitude	10

The diffraction efficiency of an amplitude zone plate is only 10%. If we make the originally opaque zone transparent but with a π phase shifting, the diffraction efficiency can be increased to 41% (a binary phase zone plate). The profile steps are proportional to the number of fabrication steps with the following relationship [27]:

$$\# \text{ of profile steps} = 2^n \quad (2-18)$$

where n is the number of masks or fabrication steps. Figure 2-18 shows that three masks (or fabrication steps) could result an eight-phase-level PZP. The profile of a PZP is closer to the ideal kinoform when the number of steps is increased.

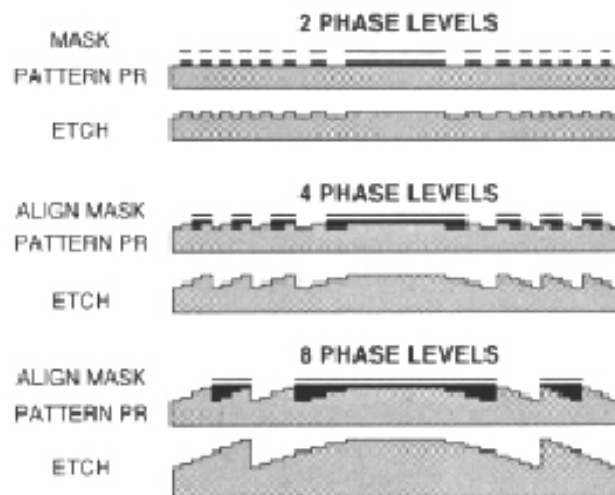


Figure 2-18. Three fabrication steps result an eight-phase-level Fresnel lens [27].

A schematic drawing of working principle and a scanning electron microscope image for a quaternary Fresnel zone plate are shown in Figure 2-19. In a quaternary phase zone plate, each level in a single zone makes incident light phase shift by $\frac{1}{4} \lambda$ and results in total constructive interference and a higher efficiency (81% from Table 2-1).

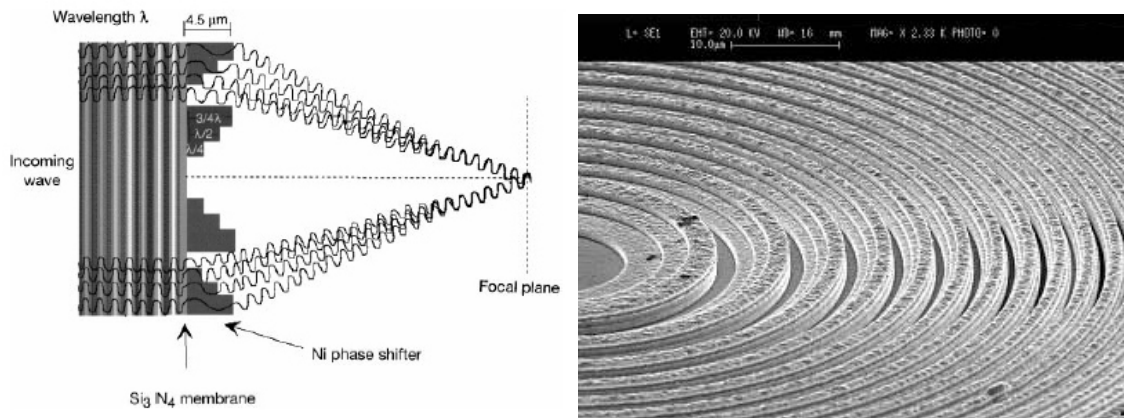


Figure 2-19. Quaternary Fresnel zone plate design and SEM image of a fabricated PZP [18].

2.4 Photon Sieve

As described above, a photon sieve is a diffractive lens composed of pinholes distributed in the Fresnel zones, as shown in Figure 2-20. Kipp et al proposed this concept in 2001 [3]. However, the photon sieve pattern shown by Kipp et al was consisted of 5646 randomly distributed holes and was very complicated. The detail design rules of the complicated photon sieve were not described in their paper.

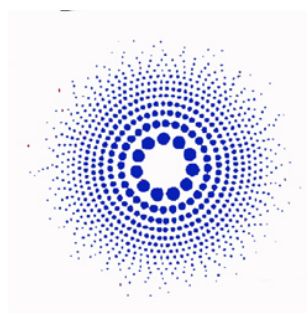


Figure 2-20. Schematic drawing of a photon sieve. Each blue spot is a hole through an opaque film.

Analogous to the concept of a Fresnel zone plate, the pinholes have to be positioned properly to fulfill the criterion for constructive interference. That requires that the optical path length (OPL) from the source via the center of the holes to the focal point be an integral number of wavelength, λ . This criterion can be expressed as the equation shown below [3]:

$$\sqrt{r_n^2 + p^2} + \sqrt{r_n^2 + q^2} = p + q + n\lambda \quad (2-19)$$

where p is the distance between the source and the photon sieve, q is the distance between the photon sieve and the focal point, and r_n is the distance between the center of the holes and the optical axis. A schematic drawing of the relationship between source, photon sieve, and focal plane is shown in Figure 2-21.

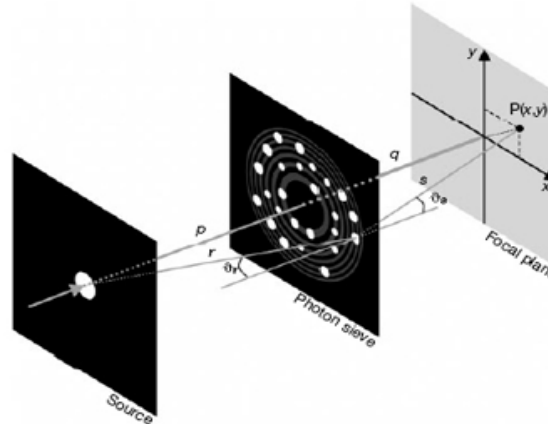


Figure 2-21. Diagram showing point-to-point imaging with a photon sieve [3].

The theoretical analysis of focusing for photon sieves in the far-field [28] and nonparaxial modes [29] were published by Qing Cao et al in 2002 and 2003, respectively. Nonparaxial mode refers to the angle between light rays and the optical axis, θ , being large. The paraxial approximation ($\sin(\theta) \approx \tan(\theta) \approx \theta$ when θ is small) [30] is no longer valid for the calculation of the OPL.

2.4.1 Advantages of Photon Sieves over Fresnel Zone Plates

Fresnel zone plates have been used to focus X-ray radiation for many years [1, 2, 31, 32]. However, ring-shaped secondary maxima are usually observed at the focal plane and cause blurring of the images from the zone plates. In addition, the resolution of Fresnel zone plates is controlled by the width of the outermost zone. Processing limitation may exist when approaching high-resolution zone plates. Photon sieves provide an opportunity to suppress the secondary maxima for sharper focusing of images and also overcome the process limitation of the resolution of Fresnel zone plates [3]. These two advantages are reviewed in the following sections.

2.4.1.1 Suppress higher diffraction order and improve focus

It is well known that side bands or secondary maxima are produced if the light passes through a rectangular type transmission window [3, 14, 20]. In a binary amplitude zone plate, the transmitted zones stopping abruptly at the outermost zone represents a rectangular transmission window. Ring shaped secondary maxima are formed and cause blurring of images. Blurring is defined by the standard deviation of the intensity distribution. For example, if the type of distribution is Gaussian, the degree of blur is then determined by the standard deviation (σ) of the Gaussian distribution (normal distribution) known as Gaussian blur [33, 34]. The greater the standard deviation, the higher the degree of blur and the greater the loss of resolution. In this research, the degree of blur was not characterized. Photon sieves, proposed by Kipp et al [3], suppress the secondary maxima and higher diffraction orders by modulating the pinhole density on each ring of the photon sieve to implement a smooth transmission window. This technique is called “apodization” and is reviewed in section 2-4-3. Figure 2-22 shows a photon sieve and a zone plate together with the experimental and calculated intensities at

the focal plane [3]. Comparing the intensities measured at focal plane, the secondary maxima (concentric ring patterns shown in Figure 2-22 **f**) observed in the zone plates were suppressed by two orders of magnitude (calculated result) when using photon sieves as the focusing element. This property was not examined in the research of dual-wavelength photon sieves; however, it was verified by the simulation result demonstrated in section 4-2-3.

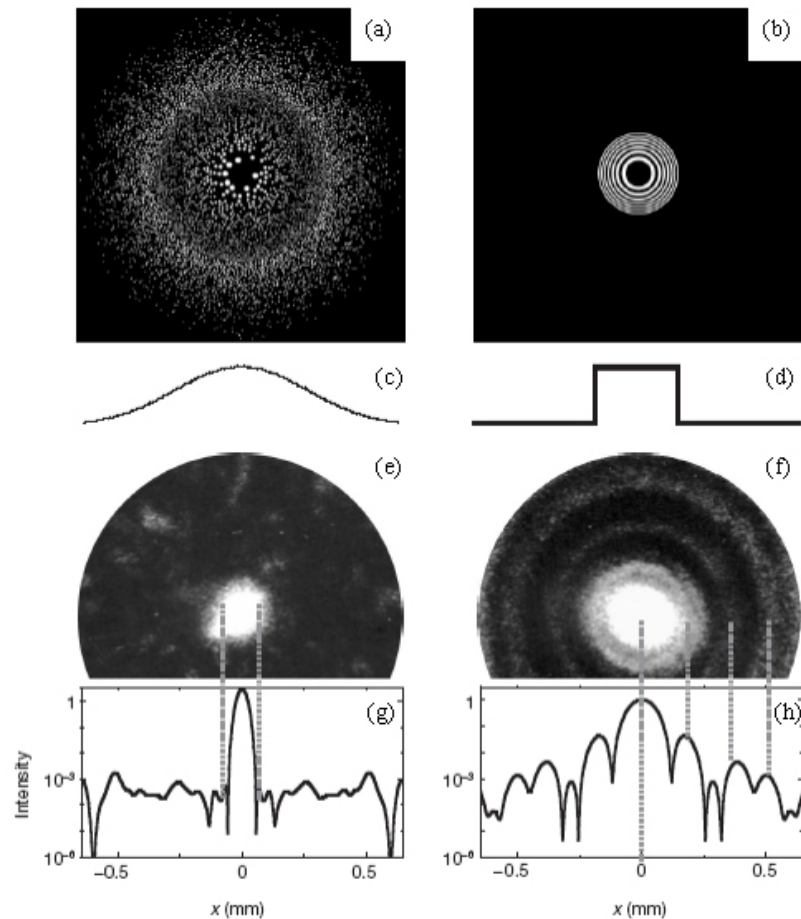


Figure 2-22. A photon sieve and a FZP together with experimental and calculated results. (a) photon sieve (b) FZP (c) smooth transmission window (d) rectangular transmission window (e) intensity at focal plane for photon sieve (f) intensity at focal plane for FZP (g) calculated intensity for photon sieve (h) calculated intensity for FZP. The secondary maxima shown in FZP was suppressed when changing the focus element from FZP to photon sieve [3]. The same phenomenon is observed from the simulation result demonstrated in section 4-2-3.

2.4.1.2 Overcoming the limitation of the resolution of FZP

In addition to suppressing the secondary maxima, photon sieves also provide an opportunity to overcome the limited zone plate resolution. The intensity at the observation plane is determined by the net contribution of interference. Kipp et al [3] produced the first photon sieve in 2001 and proposed the theory of the relation between the diffraction amplitude and the d/w ratio (i.e., the K factor in Chapter 4), where d is the pinhole diameter and w is the zone width of an underlying zone plate. This relation is shown in Figure 2-23. In the inset of Figure 2-23, the black and white strips represent the zones with destructive and constructive interferences, respectively. Four pinholes, A, B, C and D, with various diameters are drawn and the d/w ratios for the 4 pinholes are 1, 1.5, 4 and 4, respectively. The calculated curves of constructive (solid gray line) and destructive (dashed gray line) interferences and the total contribution of the two interferences (solid black curve) are shown in Figure 2-23. Both pinholes C and D have the same pinhole diameter and d/w ratio, however, the pinhole C is centered on a white zone thus the black area within the pinhole is greater than the white area which results in a net destructive interference therefore a negative intensity. Once the center of the pinhole shifts to a black zone (pinhole D), the white area within the pinhole dominates the interference and a net positive intensity will be observed at the focal plane.

The spatial resolution (δ_m) of a traditional zone plate is decided by the outermost zone width (w). However, for a photon sieve, the spatial resolution is limited by the smallest effective width (w_{\min}^{eff}), which is determined by the maximum d/w ratio [3]:

$$\delta_m = w_{\min}^{\text{eff}} = d_{\min} / (d/w)_{\max} \quad (2-20)$$

This equation implies that at a d/w ratio designed to be 1.5, a photon sieve with a smallest pinhole diameter of 45 nm has the same spatial resolution as a FZP with the outermost zone width of 30 nm. As the d/w ratio increases, the diameter of the smallest pinholes of a photon sieve can also be increased while still maintaining the same spatial resolution.

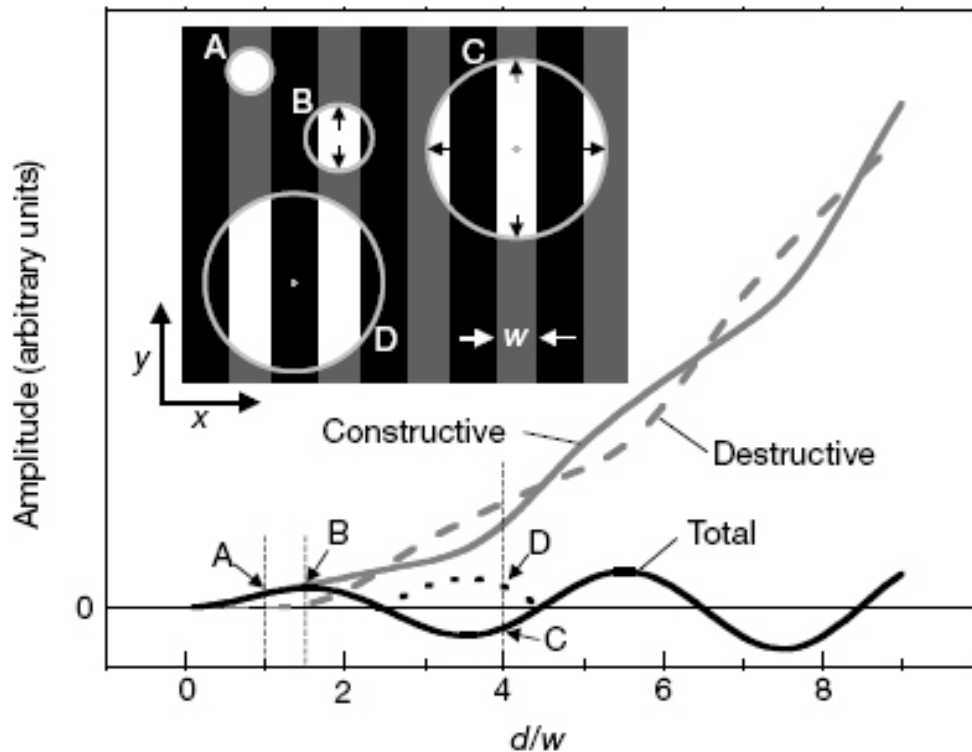


Figure 2-23. The relation between the contribution of focal amplitude and the ratio of the pinhole diameter over underlying zone width (d/w ratio). As long as the white area within a pinhole is larger than the black area, the net intensity at focal plane will be positive [3].

Menon et al [35] reported that when using a photon sieve in a maskless photon-sieve-array lithographic system, the size of the single-exposure focal spot was controlled by the K factor (d/w ratio) when the smallest pinhole diameter was fixed. The larger the K factor, the smaller the focal spot, which is consistent with the theory proposed by Kipp et al [3]. Neither Kipp et al [3] nor Menon et al [35] mentioned the limit of K factor. From the simulation result shown in section 4-2-3, the focal spot (FWHM) becomes

smaller when the K factor becomes larger; however, the intensity of the focal spot diminishes dramatically when K factor increases from 1.5 to 2. This implies that when K factor is large enough that the focal spot will not be formed since the intensity of the focal spot is too low to be observed.

2.4.2 Disadvantage of Photon Sieves over Fresnel Zone Plates

As outlined above, photon sieves have several advantages over zone plates. However, lower transmission is a very critical limitation of photon sieves. An amplitude zone plate typically has a transmission of 50% while a photon sieve only has a transmission of 15 to 20% [3]. The transmission difference between zone plates and photon sieves is proportional to the opening area of the zones and the pinholes. The low transmission does not prevent photon sieves from applications using high intensity sources, such as in synchrotrons used for X-ray microscopy [3]. For common applications where the light source is less intense, low transmittance may limit the applications of photon sieves. Low transmission reduces the signal intensities and contrast between signals and background, causing poor image quality. The contrast of a image is defined as [9]

$$\text{contrast} = (I_{\max} - I_{\min}) / (I_{\max} + I_{\min}) \quad (2-21)$$

where I_{\max} and I_{\min} are the maximum and minimum intensities of the image, respectively.

The photon sieves produced in this research consisted of a glass substrate coated with opaque metals having pinholes where light can pass through and diffract to form images. Antireflection coatings on both sides of the glass substrate can only enhance the transmission of the photon sieves by ~8% at most (4% from each side) [8]. Menon et al in 2005 [35] suggested a phase-shift photon sieve, which works in the same fashion as the

phase zone plate described in section 2-3-3. In a phase-shift photon sieve, the entire photon sieve is transparent to the light source and the pinholes have a phase shift of π with respect to the rest of the photon sieve therefore the transmission can be enhanced significantly. However, neither the detailed design nor the actual device was reported in their paper.

2.4.3 Apodization

The term “apodization” is derived from Greek which means “take away-foot” [9]. Apodization is the process of modulating the pinhole density on each ring of the photon sieve to implement a smooth transmission window and thus further suppress the secondary maxima of a diffraction pattern. It is possible to smooth the sharp discontinuity of the transmission window by adding another function onto the existing window function. The added function is called an apodization function. Apodization technique also can be applied to FZP; however, it requires very complicated equations and computer calculations to apodize the zone plate [36].

Apodization techniques are utilized in many areas, such as searching for earth-like planets in astronomy [37], microscopy, medical imaging and optical storage [38]. Apodization can be achieved by changing the aperture shapes [39] or alternating the transmission characteristics [37, 38, 40, 41]. Some of the most common apodization functions are plotted in Figure 2-24 [42]. The corresponding functions are listed in Table 2-2. For the designs of photon sieves used in this research, Gaussian apodization functions were chosen and modified to fit the various photon sieve designs through a series of simulations, which were completed by Shenderova [43-45]. The details of the simulations are described below in section 4-2.

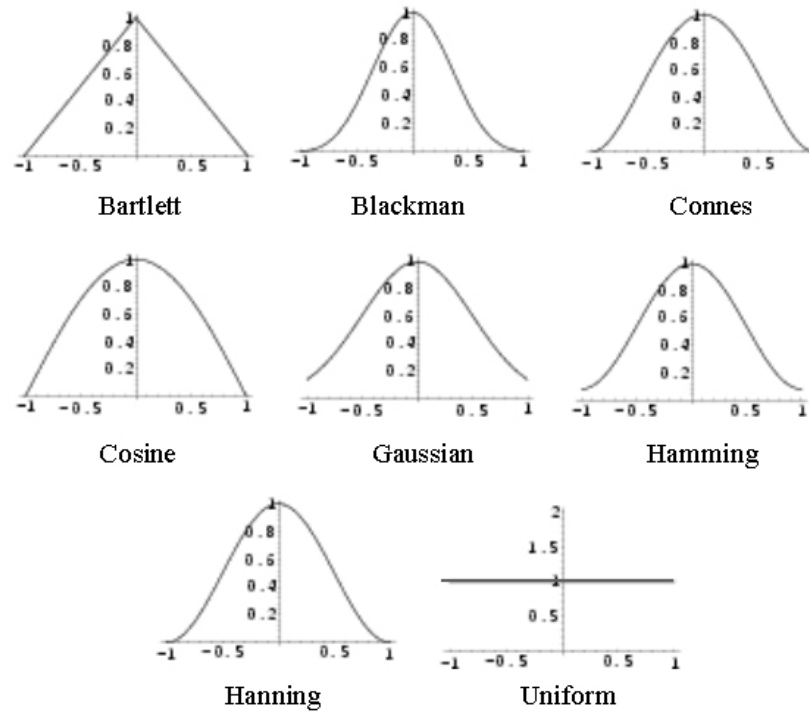


Figure 2-24. Some commonly used apodization functions in linear scale [42]. X-axis is value of x/L where x is optical path difference out to a maximum value of L (also shown in Table 2-2). Y-axis is the amplitude of the function.

Table 2-2. Equations of the apodization functions shown in Figure 2-25 [42]. x is the optical path difference and L is the maximum value of x variable.

Type	Apodization Function
Bartlett	$1 - \frac{ x }{L}$
Blackman	$0.42 + 0.5 \cos\left(\frac{\pi x}{L}\right) + 0.08 \cos\left(\frac{2\pi x}{L}\right)$
Connes	$\left(1 - \frac{x^2}{L^2}\right)^2$
Cosine	$\cos\left(\frac{\pi x}{2L}\right)$
Gaussian*	$e^{-x^2/(2\sigma^2)}$
Hamming	$0.54 + 0.46 \cos\left(\frac{\pi x}{L}\right)$
Hanning†	$\cos^2\left(\frac{\pi x}{2L}\right)$
Uniform	1

2.4.4 Applications of Photon Sieves

Photon sieves are made from a metal thin film on a thin substrate or from a free standing opaque film. In addition to their traditional use for focusing x-rays, they can be used in any application that requires small and light weight lenses. Since photon sieves are a relatively new type of diffractive lens [3], reported applications of this device are limited. Gil and Menon in 2003 and 2005 [2, 35] reported using photon sieves to replace the zone plates in their “scanning-optical-beam-lithography” system, which was based on the technique of maskless, zone-plate-array lithography (ZPAL) invented by Smith in 1996 [46]. Schematic drawings of a ZPAL system are shown in Figure 2-25.

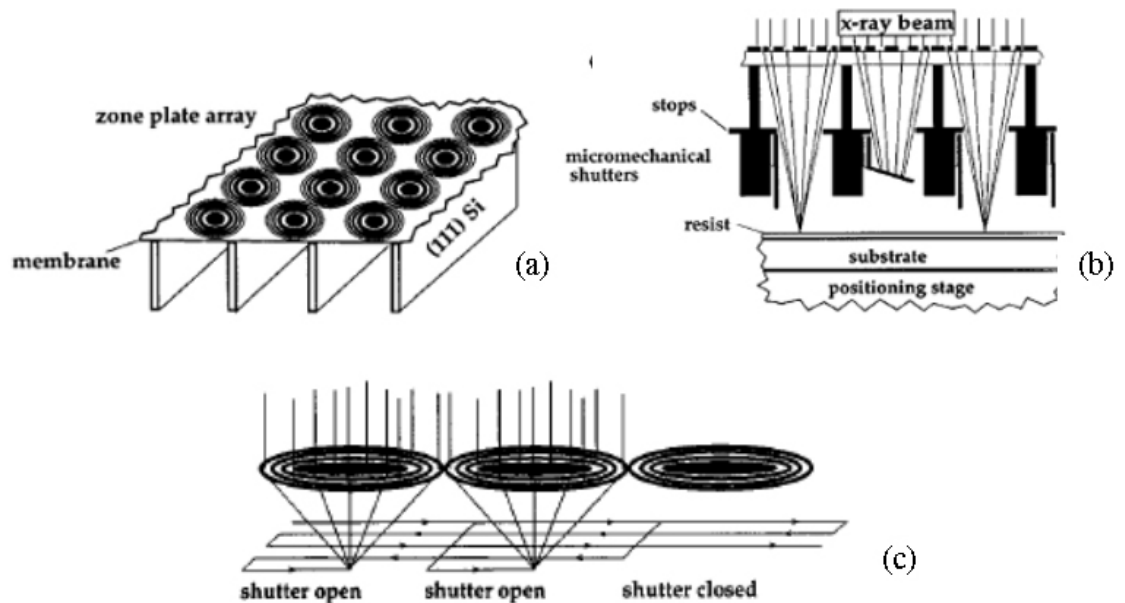


Figure 2-25. Maskless, zone-plate-array lithography (a) array membrane on the supporting joists (b) individual micromechanical shutter within each unit cell (c) pattern writing by scanning the sample in X and Y directions [46].

In the ZPAL system, thousands of $10\mu\text{m}$ -size zone plates were set in an array, where each zone plate was isolated in its unit cell that was supported on a thin carbonaceous membrane with vertical, anisotropically etched Si (111) joists for

mechanical support, as shown in Figure 2-25 (a). Each zone plate was responsible for exposure in its own unit cell. The exposure was controlled by a micromechanical shutter located within the individual unit cells, as shown in Figure 2-25 (b). The stage that held the sample was scanned in the X and Y directions to get a full pattern, as shown in Figure 2-25 (c).

2.5 Chromatic Aberration

Chromatic aberration of a refractive lens results from the dispersion of the refractive index of the lens material with wavelength. For different wavelengths, the same materials will have different refractive indices, thus cause different degrees of light bending. For example, in the range of visible wavelengths, blue rays bend more than red ones. For a polychromatic light source, the multi-wavelength rays will not focus at one single spot on the optical axial as shown in Figure 2-26, resulting in chromatic aberration.

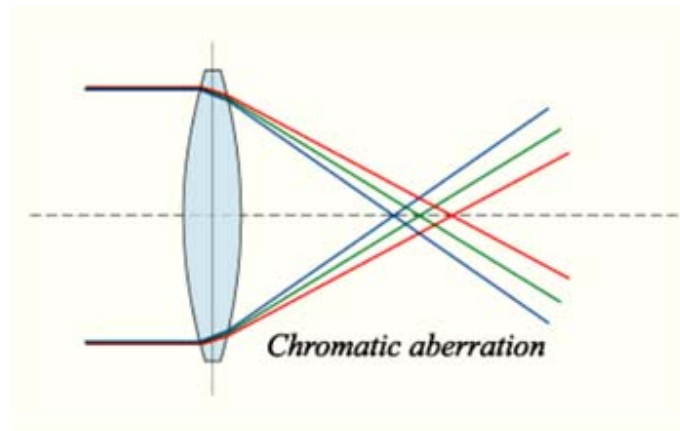


Figure 2-26 Chromatic aberration of a refractive lens [47].

For a diffractive lens, incident light rays bend when skimming the edge of an obstacle and then interfering with each other and finally focus on the observation screen. As reviewed in section 2-3, the focal length of diffractive lens is wavelength dependent. A very large longitudinal chromatic aberration is estimated by using equation (2-13). In

the visible range, red rays bend more than blue one. The light bending mechanisms for refractive and diffractive lenses are different, but both exhibit chromatic aberration.

2.6 Justification of Research

There is no true single achromatic diffractive lens to date. In reported research of diffractive lenses, no single lens was designed to have two diffraction elements. The purpose of this research is to study how lens properties changed when multiple diffraction elements with different distributions were incorporated in a single lens. A dual-wavelength photon sieve consisting of two groups of pinholes, designed to focus two wavelengths of light, is the simplest system to investigate. As reported below, such a dual-wavelength diffractive lens exhibits significant chromatic aberration. This is consistent with the diffraction theories (section 2-3) reviewed above. A number of different designs for the distribution of the two groups of pinholes were tested. The focal spot size obtained from a dual-wavelength photon sieve was same to the one obtained from a single-wavelength photon sieve but with equal or lower intensity under both monochromatic and polychromatic illuminations. The significant chromatic aberration observed in a single-wavelength photon sieve makes it a good candidate for a focusing filter lens for polychromatic light. Dual-wavelength photon sieves could be used for an imaging device that does not require complete filtering of polychromatic light at the cost of intensity. The details of testing set-up and results are shown and discussed in Chapter 4.

CHAPTER 3 PHOTON SIEVE FABRICATION

3.1 Introduction

As discussed in chapter 2, a photon sieve (PS) is a diffractive lens composed of pinholes distributed similar to the Fresnel zones. The PS, shown in Figure 3.1, consist of a glass substrate (transparent to the wavelength of interest) coated with opaque metals having a pattern of holes where light can pass through and diffract to form an image.

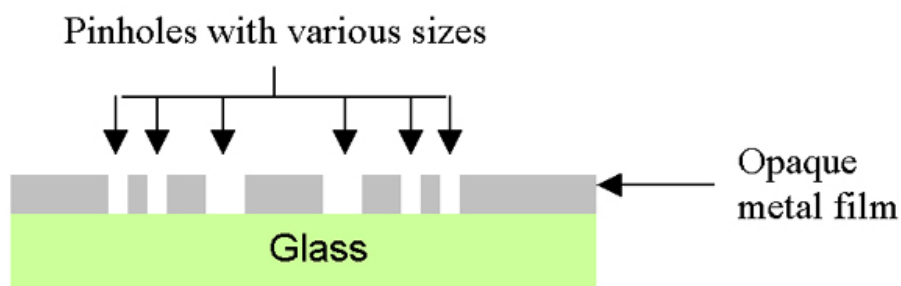


Figure 3-1. Schematic drawing of a cross-sectioned photon sieve. The size of pinhole varies from 80 to 10 μm depending on the location of pinhole for a PS designed for 500 nm light.

To make this device, lithographic techniques were used to transfer geometric patterns from software or masks to the metal film on the substrate. Depending on the type of radiation, lithography can be divided into three categories: optical, x-ray, and electrons/ion beams. Though optical lithography is widely used in the semiconductor industry, it reaches its limitations when the resolution requirements shift to submicron levels. Electron and ion beams possess high energies and therefore offer extremely small wavelengths which gives better resolution as compared to even deep or near ultra-violet

(UV) light. In addition to the better resolution, electron and ion beams can be focused to produce patterns on the resist directly without any mask.

The minimum feature size of the photon sieve designs used in this study was in the micrometer range. Either traditional photolithography or electron beam (e-beam) lithography can therefore be used for this patterning process [48]. Due to the instrument accessibility and ease of use without a mask, e-beam lithography was chosen for process development. In the following sections, details and problems that encountered in each process step are illustrated. Background knowledge of some techniques including processing and analytical instruments are introduced as well.

3.2 Process Development

Photon sieves were fabricated by first depositing by electron beam evaporation [48] a thin adhesion layer of nickel (3 nm), followed by deposition of a 150 nm silver layer on a glass substrate. The metallized substrate was then coated with electron beam (e-beam) resist, patterned using e-beam lithography and then developed. The patterned e-beam resist was used as a mask to protect the underlying metal films during etching, either dry or wet etching depending on different process method. The e-beam resist was then stripped, resulting in a photon sieve. A flow-chart of general processing steps is shown in Figure 3-2. Four different process methods, which will be named (1) reversed image etching, (2) direct wet etching, (3) direct dry etching, and (4) lift-off, are described in Figure 3-2. The acronyms and abbreviations used in Figure 3-2 are listed in Table 3-1. The procedures of substrate cleaning, metal deposition, and e-beam pattern writing were identical for these four procedures. The e-beam resists, developers, etching methods, and resist strippers were different depending on the process method. Complete descriptions of each method are given below in sections 3.2.6.1 to 3.2.6.4.

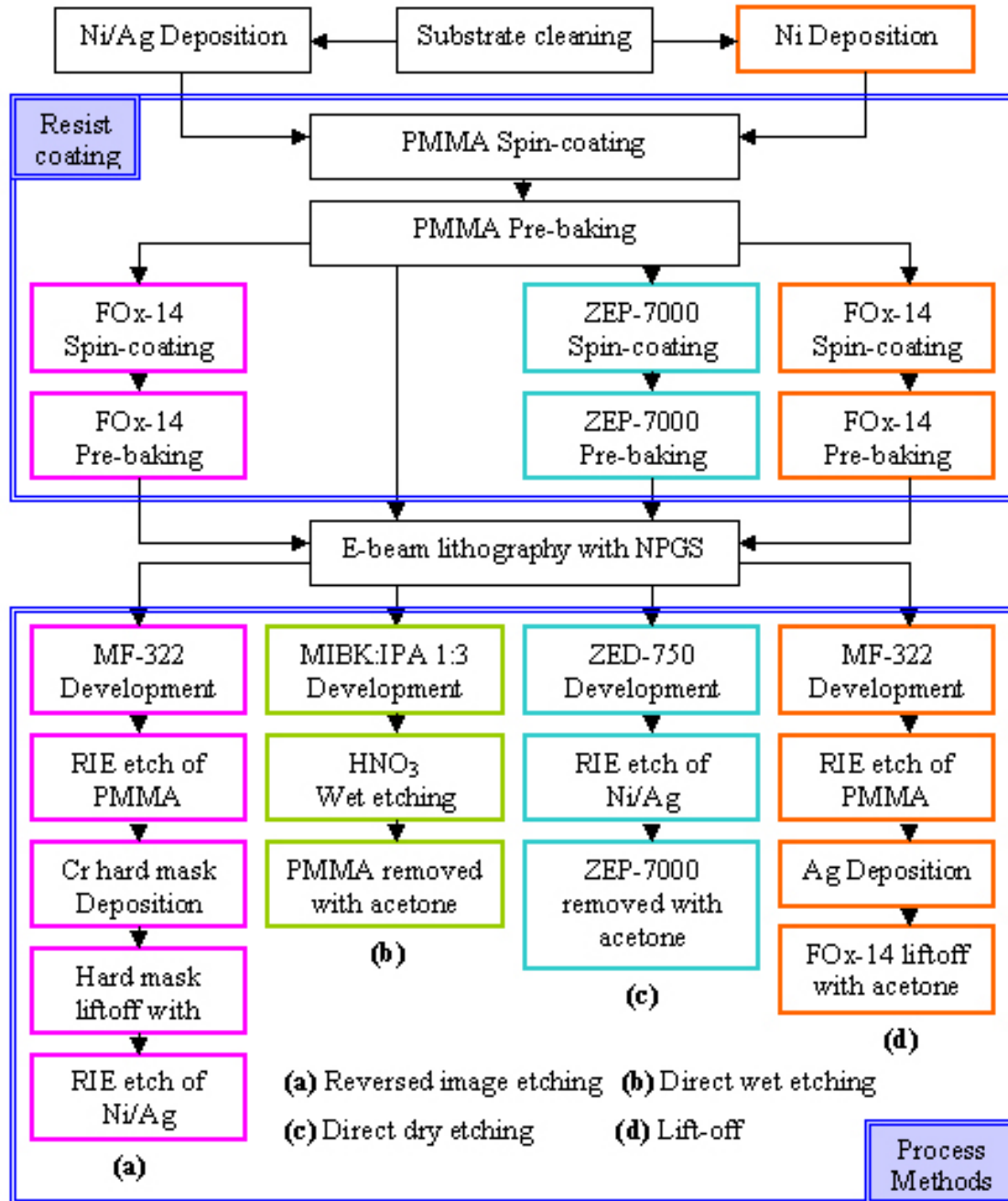


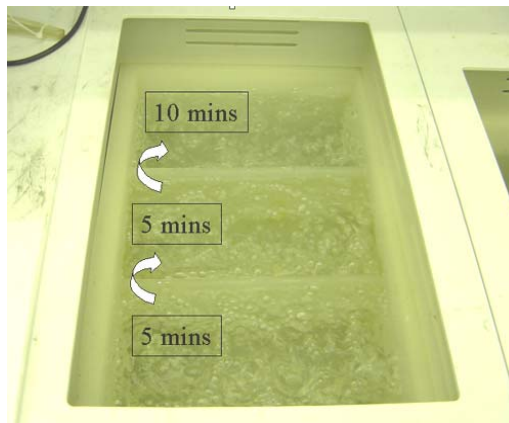
Figure 3-2. Flowchart of various processing methods (a) to (d). The whole development is divided into five big steps, substrate preparation, film deposition, resist coating (flow charts within the top blue-double-line box), e-beam lithograph, and four process methods (flow charts within the bottom blue-double-line box). Equipments, operation details, and problems of each step is discussed in the following corresponded section.

Table 3-1. Acronyms and abbreviations shown in Figure 3-2.

Acronym and Abbreviation	Full Name
PMMA	Polymethylmethacrylate
FOx-14	Liquid solution of hydrogen silsesquioxane (HSQ)
ZEP-7000	Proprietary positive e-beam resist
MF-322	Proprietary developer for FOx-14
RIE	Reactive Ion Etching
MIBK	Methyl isobutyl ketone
IPA	Isopropyl alcohol
ZED-750	Proprietary developer for ZEP-7000
NPGS	Nanometer Pattern Generation System

3.2.1 Substrate Preparation

All PSs were fabricated on pre-cleaned glass microscope slides purchased from Fisher Scientific (Cat. No. 12544). The glass slides were 3 x 1 x 1/16 inch but were cut into 1 x 1 x 1/16 inch substrates followed by scrubbing for 5 min. in an Alconox (powder detergent from Fisher) DI water solution. After rinsing-off the detergent, the substrates were submerged into a three-stage cascade DI water rinse bath with N₂ bubblers, as shown in Figure 3-3 (Bold Technologies Inc. Model 625T wet bench), for over 20 minutes. Substrates were always placed in the lowest (dirtiest) tank for 5 minutes, then the middle tank for another 5 minutes, and finally the highest (cleanest) tank for 10 minutes. The substrates were then blow dried with dry N₂.

Figure 3-3. Three-stage cascade DI water rinse bath with N₂ bubblers on the wet bench.

3.2.2 Film Deposition

Metal films were deposited by electron beam evaporation. The details of film deposition and the illustration of e-beam evaporator are given in the following sections.

3.2.2.1 Electron-beam evaporator: system and operation

Figures 3-4 and 3-5 show a schematic drawing and a photograph of the e-beam evaporator, respectively. The detailed structure inside the processing chamber is shown in Figure 3-6. The diffusion pump is used as an example when describing the process steps.

Before starting to pump the chamber to lower pressure, the mechanical pump (Leybold Dryvac 100P) and diffusion pump need to be turned on for at least 30 minutes to allow the pumps to stabilize or reach the operation temperature (about 250°C for diffusion pump oil). Stable operation and attainment of the proper vacuum should be verified by pressure gauge readouts. Liquid nitrogen was added into the cold trap before pumpdown. The cold trap is used to condense the oil vapor into its solid phase to prevent the pump oil from backstreaming and contaminating the work chamber.

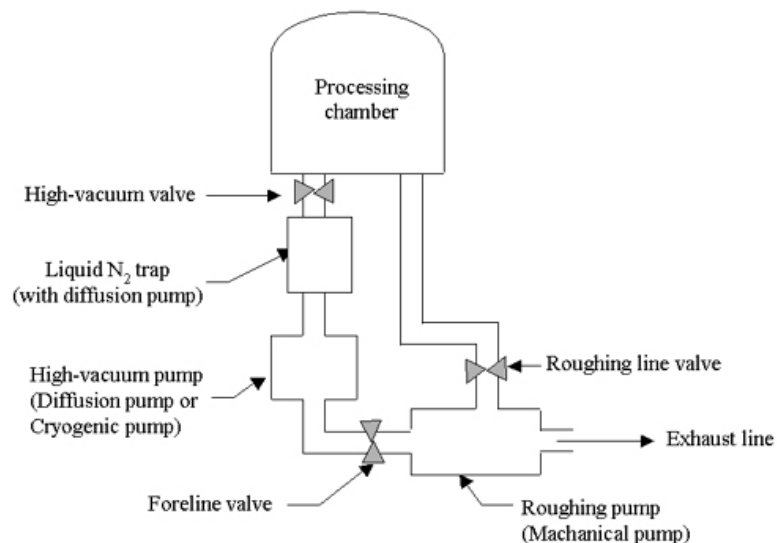


Figure 3-4. Schematic drawing of e-beam evaporator system.

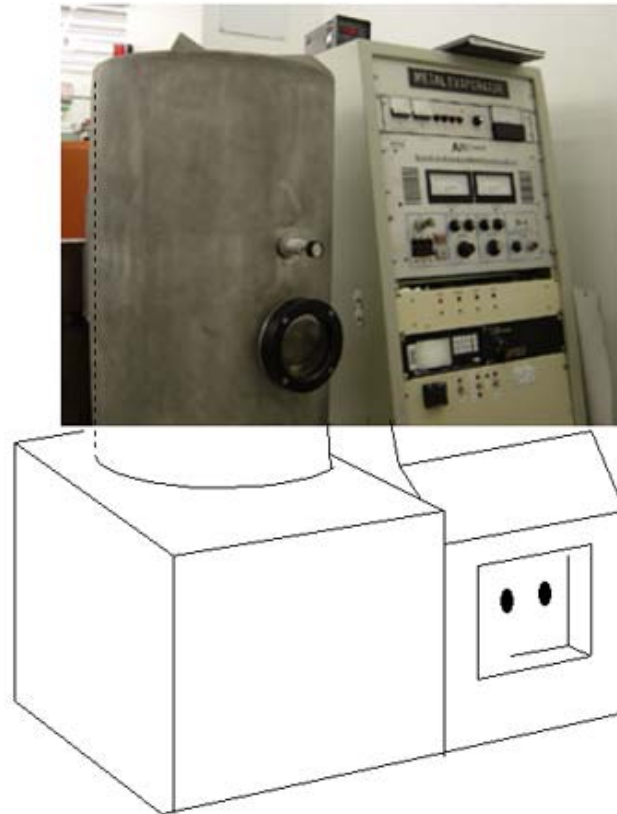


Figure 3-5. Photograph of electron-beam deposition chamber and control rack.

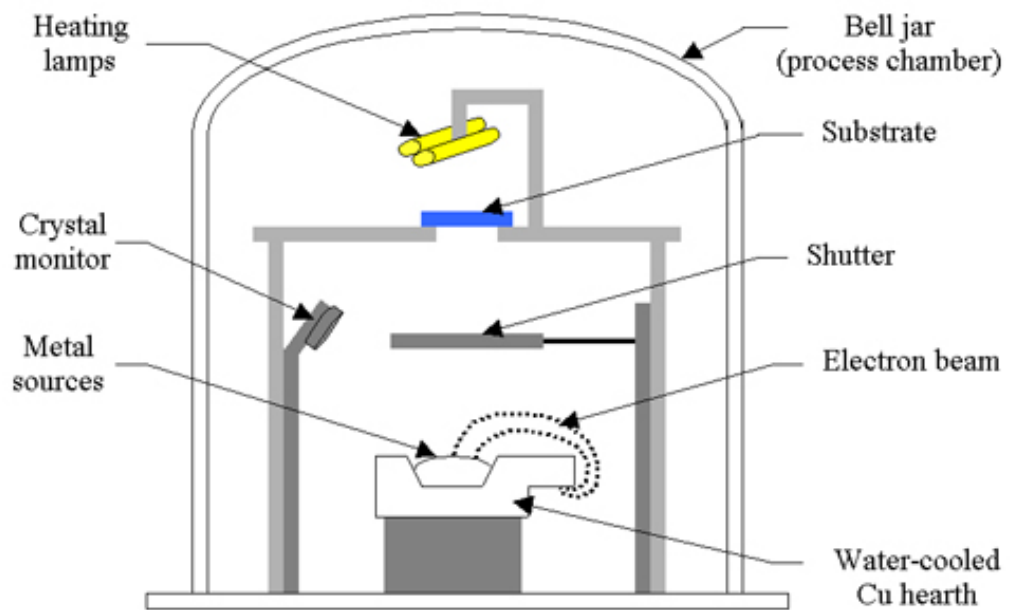


Figure 3-6. Detailed structures inside bell jar of an e-beam evaporator.

After placing two substrates in the process chamber, the bell jar was closed and the roughing line valve was opened to rough the chamber down to a crossover pressure of 150 milliTorr. The roughing line valve was then closed and the foreline and high vacuum valves then opened. If the pressure in the foreline is pumped too low ($<150\text{mTorr}$), the mechanical pump oil will backstream and contaminate the chamber [49]. Conversely, if the crossover pressure is too high, backstreaming of the diffusion pump oil to the process chamber will occur due to the collapse of vapor jets in the diffusion pump. Once the foreline and high vacuum valves were opened, the diffusion pump could pump down the chamber to very high vacuum (10^{-6} Torr). The mechanical pump was left on to serve as a backing pump for the diffusion pump. An ion gauge was used to monitor the chamber pressure.

Metal deposition was carried out at an operating pressure of $3 \sim 5 \times 10^{-6}$ Torr. The water-cooled copper hearth can hold up to 5 different sources and the source in use was controlled by a small rotary motor. The ability to rotate a different hearth into the source position allows deposition of multi-layer thin films of various materials without breaking the vacuum. Each source material (e.g., Ni or Ag) was placed in a graphite crucible (1 inch in diameter, 0.75 inch in depth, Kurt J. Lesker EVCEB-11) in sufficient quantities to cover the whole base but no more than $2/3$ of the depth of the crucible to avoid overflowing of the source material. Electrons are thermionically emitted from a hot filament then accelerated by a high voltage (30 kV). The electron beam is deflected by a magnetic field, focused by an electrostatic lens, and heats the source materials to a temperature where the sublimation or evaporation rates are sufficiently high to deposit a

thin film at an acceptable rate. The electron beam is controlled by an electron beam power supply (Airco Temescal model ES-6).

The cleaned, bare 1 x 1 inch substrates were placed on a sample holder which allowed a nearly normal-incidence of the evaporative flux in order to minimize shadowing effects [48, 50]. The substrates were heated to above 200°C by heating lamps (Globe D, 50V, 200W) to eliminate adsorbed water moisture. The heating lamps were then turned off and the substrates allowed to cool for about 15 minutes. Metal deposition was then initiated by heating the source metal with the electron beam. An adhesion layer of nickel with a thickness of 30 Å was deposited at a rate of about 5 Å/s and a substrate temperature between 50-70°C controlled by the heat lamps. The elevated temperature provides a good film quality. The deposition rate and thickness were controlled by an INFICON deposition controller XTC/2 which is described in section 3.2.2.2. After the deposition of nickel, the copper hearth was rotated to the silver source and a 1500Å silver film was deposited at a rate of 20 Å/s, with the substrate temperature again controlled between 50-70°C. The metal-film-coated substrate was left in the vacuum chamber for over 15 minutes to cool down close to room temperature before venting the chamber and removing the substrates.

For silver deposition, when the bottom of the crucible was not completely covered by the source metal, tiny silver balls (< 10 µm) were observed on the silver film, as shown in Figure 3-7. Cotronakis et al [51] reported that carbon contamination was the cause of gold spitting. The gold spitting was reduced by removing the carbon residual from the gold source. It is speculated that when the electron beam hits the bottom of the graphite crucible, carbon contamination increased and caused the silver spitting. This

problem was avoided when the silver metal source was in sufficient quantity to cover the whole base.

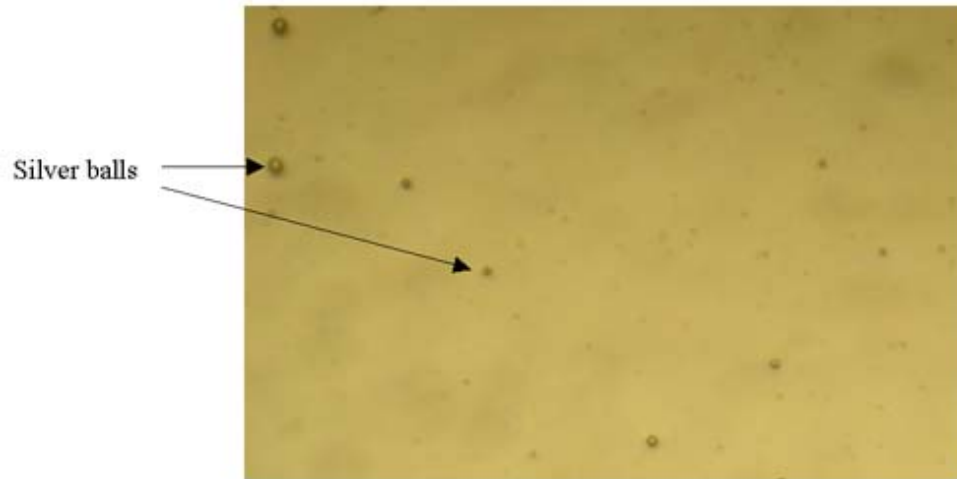


Figure 3-7. Silver spitting. Small spherical silver balls spitted from the molten silver source. The size of the largest silver balls is about 10 μm .

At the beginning of process development, a diffusion pump was used as the high vacuum pump in the e-beam deposition system, but was replaced by a cryogenic pump for the last half of the research. This change did not disrupt the research results reported below for photon sieves. The most significant difference between a diffusion pump and a cryogenic pump is that no pump fluid or lubricant is used in cryopumps; thus backstreaming of oil from the pump to the processing chamber does not occur. The cryopump is continually running until regeneration is needed to remove the captured gases and restore its pumping capacity. The mechanical pump can be turned off after opening the high vacuum valve since there is no need of a backing pump for the cryopump. The rest of the details of a cryogenic pump can be found in the following references [49, 52, 53]. The change from diffusion pump to cryopump for the-beam evaporator reduced the processing time and also resulted in a better film quality.

3.2.2.2 Deposition controller

By setting multiple parameters of the source materials in the deposition controller (INFICON XTC/2), the controller can control the shutter to open and close automatically according to the preset film thickness. The deposition monitor is a quartz crystal with special piezoelectric sensitivity. The piezoelectric crystal changes its shape when a RF voltage is applied and mechanical oscillations result. The frequency of the oscillation is a function of the thickness of the crystal. During the deposition, the added mass reduces the frequency of this oscillation. Before deposition, the density and the Z-ratio of the depositing film are entered into the microprocessor within the deposition controller to correctly convert frequency change to film thickness. The Z-ratio is equal to [54]

$$(\rho_q u_q / \rho_f u_f)^{1/2} \quad (3-1)$$

where ρ_q, ρ_f are the densities of quartz and the deposited film, respectively, and u_q and u_f are the shear moduli of the quartz and the film, respectively. The derivation of equation (3-1) can be found in references [54-57].

Table 3-2 shows densities and Z-ratios of materials used in the project. If multiple layers were deposited, the Z-ratio used for the second layer is decided by the relative thickness of the two layers. When one layer is thick compare to another, the Z-ratio of the thick film is used for both layers regardless of the sequence of deposition. When the thickness of both layers is similar, a weighted average of the two Z-ratios is used [54]. A picture of a deposition monitor and a schematic drawing of a quartz crystal oscillator are shown in Figure 3-8 (a) and (b), respectively [57, 58].

Table 3-2. Densities and Z-ratios of materials used in the experiment.

Formula	Density	Z-ratio	Material Name
Ag	10.500	0.529	Silver
Cr	7.200	0.305	Chromium
Ni	8.910	0.331	Nickel
MgF ₂	3.180	0.637	Magnesium Fluoride

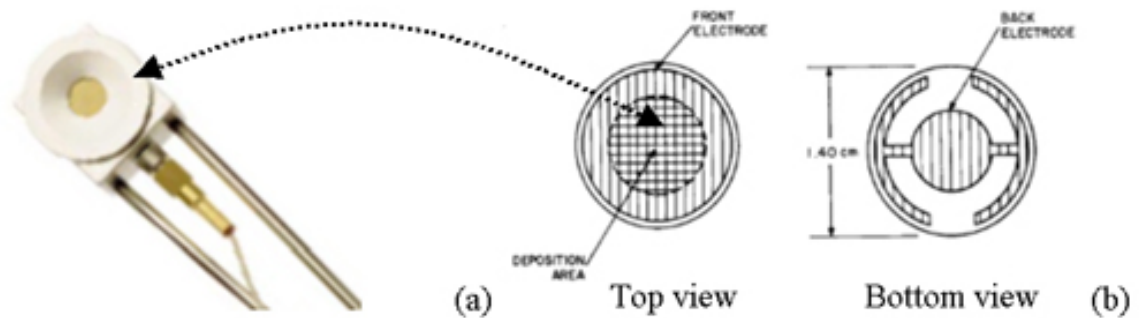


Figure 3-8. Standard deposition monitor (a) and quartz crystal oscillator (b) [57, 58].

3.2.3 Resist Coating

3.2.3.1 Electron-beam resists

Depending on the processing methods, three different e-beam resists were used: PMMA, FOx-14, and ZEP-7000. PMMA is an ultra-high resolution positive e-beam resist [59]. Positive resist means that the exposed areas are removed during development, leaving a positive image in the resist. On the other hand, the negative resist is the resist where the exposed areas are retained while the unexposed areas are removed, resulting in a negative image in the resist [48]. The PMMA used in the experiment was 950 PMMA C4 obtained from Microchem, Inc. Microchem offers a variety of molecular weights and solvent systems for PMMA. The “950” resist has a molecular weight of 950,000 and “C4” represents a 4% PMMA concentration in chlorobenzene.

FOX-14 is a liquid solution of hydrogen silsesquioxane (HSQ) in a solvent obtained from Dow Corning. First generation FOX (referred as FOX-1x) uses MIBK as the solvent while second generation resist (referred as FOX-2x) uses a volatile methyl siloxane (VMS) as the solvent [60]. FOX-14 is a flowable, inorganic polymer which forms a micro-porous amorphous (SiO₂-like) film after the e-beam exposure. It is a high resolution negative e-beam resist.

ZEP7000 is a high resolution positive e-beam resist with excellent dry-etching resistance obtained from Zeon Chemicals L. P., a Japanese company. It is a polymer of an unspecified type with a molecular weight of 340, 000 and was dissolved in diethylene glycol dimethyl ether [61].

For positive resist, such as PMMA and ZEP7000, the energy provided by the electrons breaks bonds in the polymer chains and results in a local reduction of molecular weight. As a result, the exposed area is more chemically active and can be dissolved by the developer. For negative resist, the electrons provide energy for molecular chain to cross-link so that the exposure areas are retained while the unexposed areas are dissolved by the developer. The doses, energies and developers required for PMMA, FOX-14, and ZEP700 are described in section 3.2.4 on pattern formation.

3.2.3.2 Spin-coating and prebake

The spin coater used in the experiment was a P6700 by Specialty Coating System, Inc. It has an 8-inch polytetrafluoroethylene (PTFE) coated bowl with a programmable three-stage spin controller. The speed range of the spin coater is from 100 to 8000 rpm with hold times of 0 to 999 seconds. Figure 3-9 shows a picture of the P6700 spin coater.



Figure 3-9. P6700 series spin coater by Specialty Coating System, Inc.

The spin coating process can be separated into four stages [62-64]. The first stage is dispensing the e-beam resist onto the substrate by using a disposable pipet. The second stage is the acceleration of the turntable to the desired speed. In the third stage, the substrate is spinning in a constant speed and the viscosity force of the resist dominates the film thinning process. The fourth stage is similar to the third stage that the substrate spins at constant speed. However, the coating thinning process is dominated by the solvent evaporation instead of fluid viscosity. The coating thickness is essentially determined by the balance between forces that shear the resist toward the edge, and the drying rate that affects the viscosity of the resist.

Generally, for a known resist, higher spin speed and longer spin time result in thinner coatings. When the spin speed increases, the centrifugal force increases and less fluid can be held on the substrate; thus, the thickness of the fluid decreases. Data from the manufacturer on the relationship between the spin speed and thickness is shown in Figure 3-10 for ZEP resists [61]. For ZEP7000, the film thickness was about 1800Å for the spin speed of 3000 rpm used in this study.

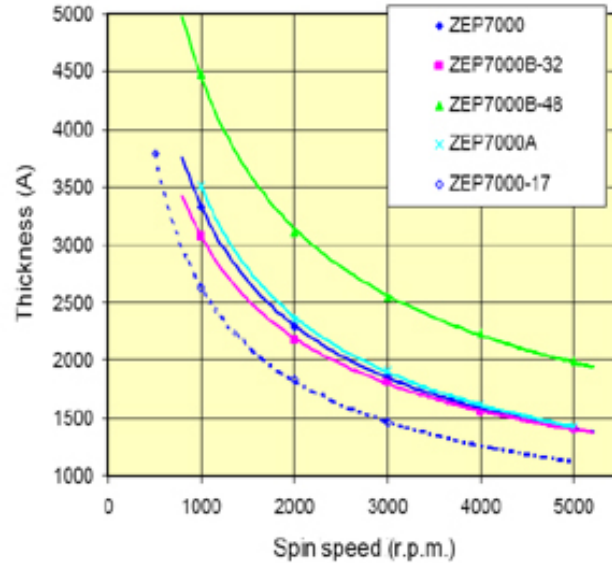


Figure 3-10. Relationship between the spin speed and thickness [61].

The substrate with deposited films was first loaded onto the vacuum chuck and cleaned by spin-rinsing first with isopropyl alcohol (IPA) then methanol. The substrate was spun at 200 rpm for 10 seconds. E-beam resist was then dispensed onto the rotating substrate and allowed to spread over the substrate. This method conserved resist material since it was only necessary to cover the center of the substrate. After this dispensing step, the spin speed was increased to 3000 rpm and held at that speed for 35 seconds. PMMA, FOx-14, or ZEP7000 were spun coated onto the substrates with the same recipe and the thicknesses of the coatings were 5000Å, 3000Å, and 1800Å, respectively.

Spin coating defects, reported in the literature and shown in Figure 3-14 [64], were observed on the present samples. Comets, Figure 3-11 (a), are caused by large contaminated particles on the substrate, and can be reduced by working in a particle-free environment. Uncoated areas, Figure 3-11 (b), are caused by dispensing insufficient amounts of resist, and can be corrected by simply increasing the amount of dispensed resist.

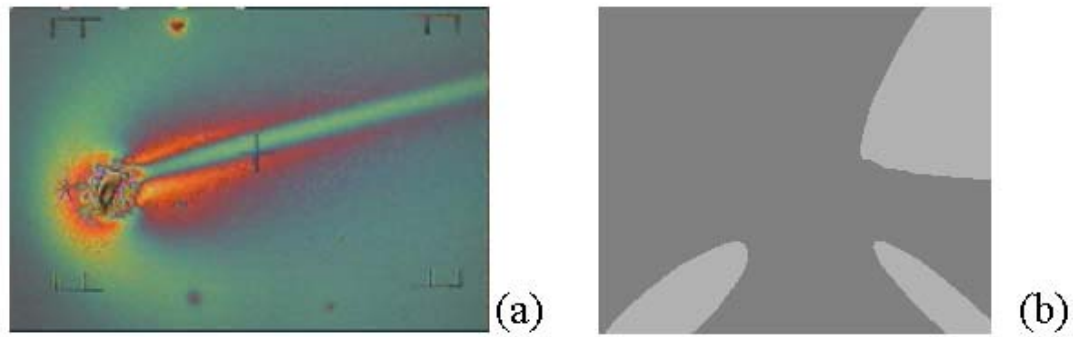


Figure 3-11. Optical photographs of spin coating defects: (a) comet, and (b) uncoated area [64].

After spin coating, the substrates were prebaked (soft baked) to remove solvents from the resist. The hot plate used in the experiment was a Cole Parmer DATAPLATE 720 Series Digital Hot Plate. It had a ceramic plate surface and is capable of temperatures in excess of 370°C.

The film thickness of the resists shrank to about 85% of its initial value during prebaking [61, 65]. The prebake temperature and time are different depending on type of resist. Depending on the heat transfer mode, either conduction (hot plate) or convection (oven), the time required for prebake is different. It requires a longer time, generally 20 to 30 minutes, to bake the substrate in a convection oven and it only needs 1 or 2 minutes to bake the substrate on a hot plate. In addition to the slower heat transfer mode (convection), a skin forms on the top of the resist during the solvent drying and further hinders the rapid evaporation of the volatile component within the resist [66] when baking the substrate in a convection oven. In this research, the temperature of the hot plate was set to be 180°C. The time of prebake for PMMA, FOx-14, and ZEP7000 were 15 minutes, 2 minutes, and 2 minutes, respectively. After spin coating and prebaking, the substrates were ready for writing of the patterns.

3.2.4 Pattern Formation

The photon sieve patterns were written with a Phillips XL 40 scanning electron microscope (SEM) controlled by the nanometer pattern generation system (NPGS). NPGS is software and hardware that generated steering voltages to control the beam location and dwell time from an input data file (DesignCAD files in this research) describing the pattern to be written.

The resist-coated substrate was loaded onto a multi-sample translatable stage along with a gold standard and a Faraday cup. The acceleration voltage was set to be 30kV and spot size of the electron beam is size 4, i.e., a diameter of a few nanometers. The gold standard was used to focus the electron beam with a working distance of 12.8 to 13.2 mm depending on the minimum magnification required by the pattern design. Astigmatism and beam alignment (controlled by lens modulator) were adjusted to resolve surface features at high magnification of 60,000 ~ 125,000X. After these initial adjustments, no further changes in focus and astigmatism were made. By moving the stage to the Faraday cup and increasing the magnification, the electron beam current was measured and recorded. Due to the absence of a beam blanker, the stage was then moved to place the beam on the edge of the substrate at a magnification of 400X or greater to minimize the e-beam exposure in the area to be patterned. The stage rotation was then adjusted by the Stage/x-align command for sample alignment. The height of the substrate was adjusted till the resist surface was in focus. Writing of the desired photon sieve pattern was controlled by the run file and the NPGS software. The number and type of patterns, the locations of the patterns on the substrates, the e-beam dose, the center-to-center distance and the line spacing of electron beam writing were all specified in the run file. The center-to-center distance is the distance between two e-beam exposed areas (area mode)

and line spacing is the distance between two e-beam exposed lines (line mode). The beam current was between 1680 and 1720 pA for a beam spot size of 4. The e-beam dosage of PMMA, FOx-14, and ZEP7000 were set to an “area dose” of $130 \mu\text{C}/\text{cm}^2$, $45 \mu\text{C}/\text{cm}^2$, and $45 \mu\text{C}/\text{cm}^2$, respectively. The line spacing and the center-to-center distance were both set to 100 nm. If the line spacing or the center-to-center distance is too small, over-exposure problems may occur. The “non-stop writing” mode was selected for all pattern writing processes. After entering all the parameters, the NPGS calculated the exposure time automatically and controlled the beam movement according to the pattern design. The e-beam was turned off immediately after the pattern writing was finished to prevent unnecessary exposure to the resist. Depending on the pattern designs, the writing time of a single photon sieve was about 20 to 40 minutes. The chamber was then vented and the sample was unloaded for development of the resist pattern (see Figure 3-2 for process flow chart).

The developer used for PMMA resist consists of MIBK with IPA in a ratio of 1 to 3. The developing time was 70 seconds in a beaker at room temperature without stirring. After development, the substrate was rinsed with IPA then blow dried with pure N_2 . The developer for FOx-14 was Microposit MF-322 obtained from Shipley Company and consists of 2.44% tetramethylammonium hydroxide (TMAH), less than 1% of surfactant [67] and water. The substrate was developed in MF-322 for 90 seconds and rinsed by de-ionized (DI) water, then dried with pure N_2 . For ZEP7000, the proprietary developer is ZED-750 obtained from the Zeon Chemicals L. P. The substrate was developed in ZED-750 for 2.5 minutes, then rinsed in IPA and dried with N_2 .

3.2.5 Reactive Ion Etch (RIE)

The RIE system used for the experiment is a PlasmaTherm SLR770 series reactive ion etcher with a turbopump (Leybold Turbovac 1000) and two mechanical pumps (Leybold Trivac BCS) used for backing the turbopump and roughing the loadlock, respectively. The system includes a loadlock chamber with an automatic arm to move the sample into the etching chamber. The loading platform was able to handle different sample sizes from small to a 4-inch wafer. The PlasmaTherm SLR770 has an ECR plasma source produced by a 1000W microwave power supply and is combined with a 13.56MHz 500W RF power supply. The ECR source operated at 2.45GHz [65]. Reactive ion etching is discussed in detail in reference [48]. Figure 3-12 is a photograph of the PlasmaTherm SLR770.

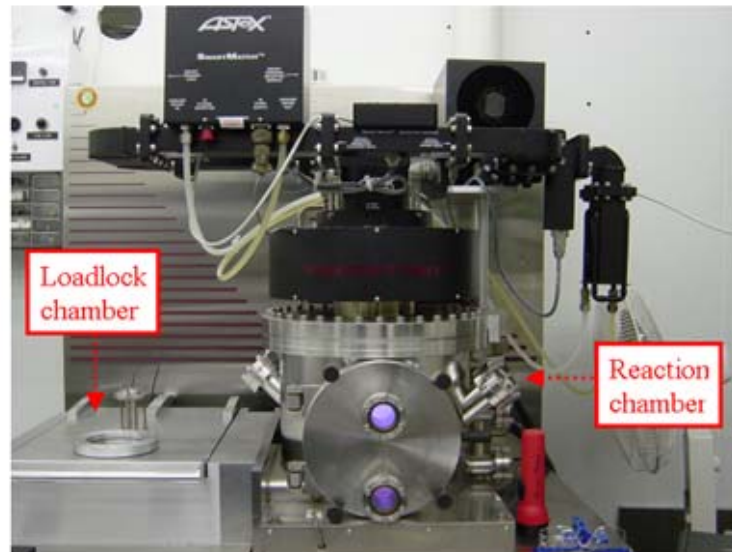


Figure 3-12. Photograph of the PlasmaTherm SLR770.

During the process development, etching recipes with oxygen, argon, or a proprietary $H_2/Ar/CH_4$ etching recipe [68], were used to etch PMMA and silver. Oxygen plasma was used to etch the PMMA layer and the argon plasma was used to sputter etch

the silver metal. The proprietary etching recipe (patent pending) was used to etch the silver metal with excellent selectivity between chromium and silver. Selectivity in plasma etching is defined as the ratio of the etching rates of two different materials when exposed to the same plasma environment [48]. When the etch rate of the mask is low and the etch rate of the underlying material is high, the selectivity is good. The actual reason for the excellent selectivity is not clear. The detailed compositions and operation parameters for the recipes are shown in Table 3-3.

Table 3-3. Experiment parameters of plasma-etching recipes for RIE process.

	Oxygen plasma	Proprietary recipe (Patent pending)	Argon plasma
Etched material	PMMA	Ag	Ag or Ni
Mask	FOx-14	Cr	ZEP-7000
Pressure	10 mtorr	proprietary recipe	1 mtorr
Temperature	Room temp.	Room temp	Room temp
RF power (W)	100	proprietary recipe	100
ECR power (W)	0	proprietary recipe	900
Gas / Flow rate	O ₂ / 20 sccm	H ₂ / proprietary recipe Ar / proprietary recipe CH ₄ / proprietary recipe	Ar / 10 sccm

3.2.6 Various Process Methods: Procedures and Results

Photon sieve patterns were created by four different processes (reversed image etching, lift-off, direct wet etching, and direct dry etching) as described in the flow chart in Figure 3-2. They are described in detail below.

3.2.6.1 Reversed image etching process

Photon sieves were fabricated by first depositing by electron beam evaporation a thin adhesion layer of nickel of 30 Å, followed by deposition of a layer of silver (1500 Å)

on a cleaned glass substrate. In the reversed image etching process, the metallized substrate was coated, first with PMMA with a prebake at 180°C for 15 minutes, and subsequently with FOx-14 with a prebake at 180°C for 2 minutes. The FOx-14 was patterned using electron beam lithography and then developed by MF-322 for 90 seconds. The unexposed FOx-14 was dissolved in the developer and then the exposed PMMA was removed by oxygen plasma etching. The oxygen plasma recipe and detailed operation procedures for RIE and etching recipes were described above. After etching the PMMA, a 250Å-thick chromium (Cr) layer, used as a hard mask for RIE, was deposited by e-beam evaporation. The sample was then rinsed by ultrasonication in an acetone bath (Fisher Scientific ultrasonic FS-28) to lift off the Cr/FOx-14/PMMA masked areas, exposing the silver layer. After lift off, the sample was dried and the silver and nickel was etched using RIE with the proprietary recipe [68] (see Table 3-3) to produce the transparent PS holes. Figure 3-13 shows an optical micrograph of a photon sieve manufactured by this method. The process steps in this method are shown schematically in Figure 3-14.

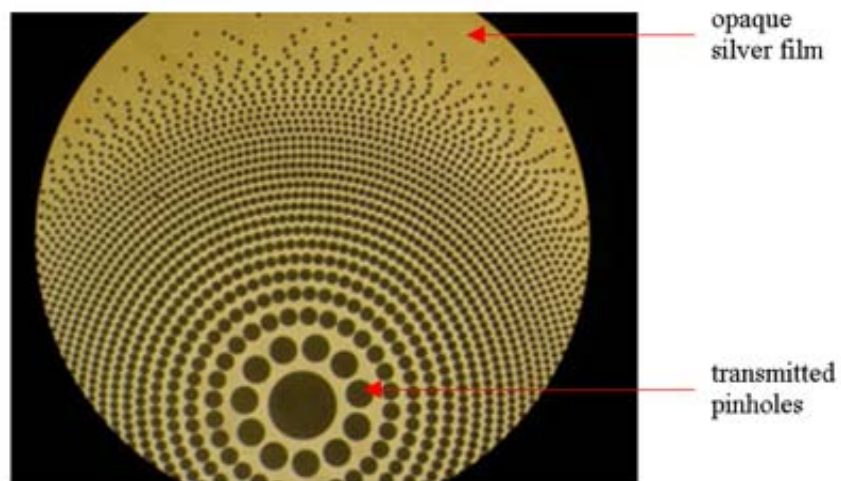


Figure 3-13. Optical micrograph of an apodized photon sieve manufactured by reversed image etching method.

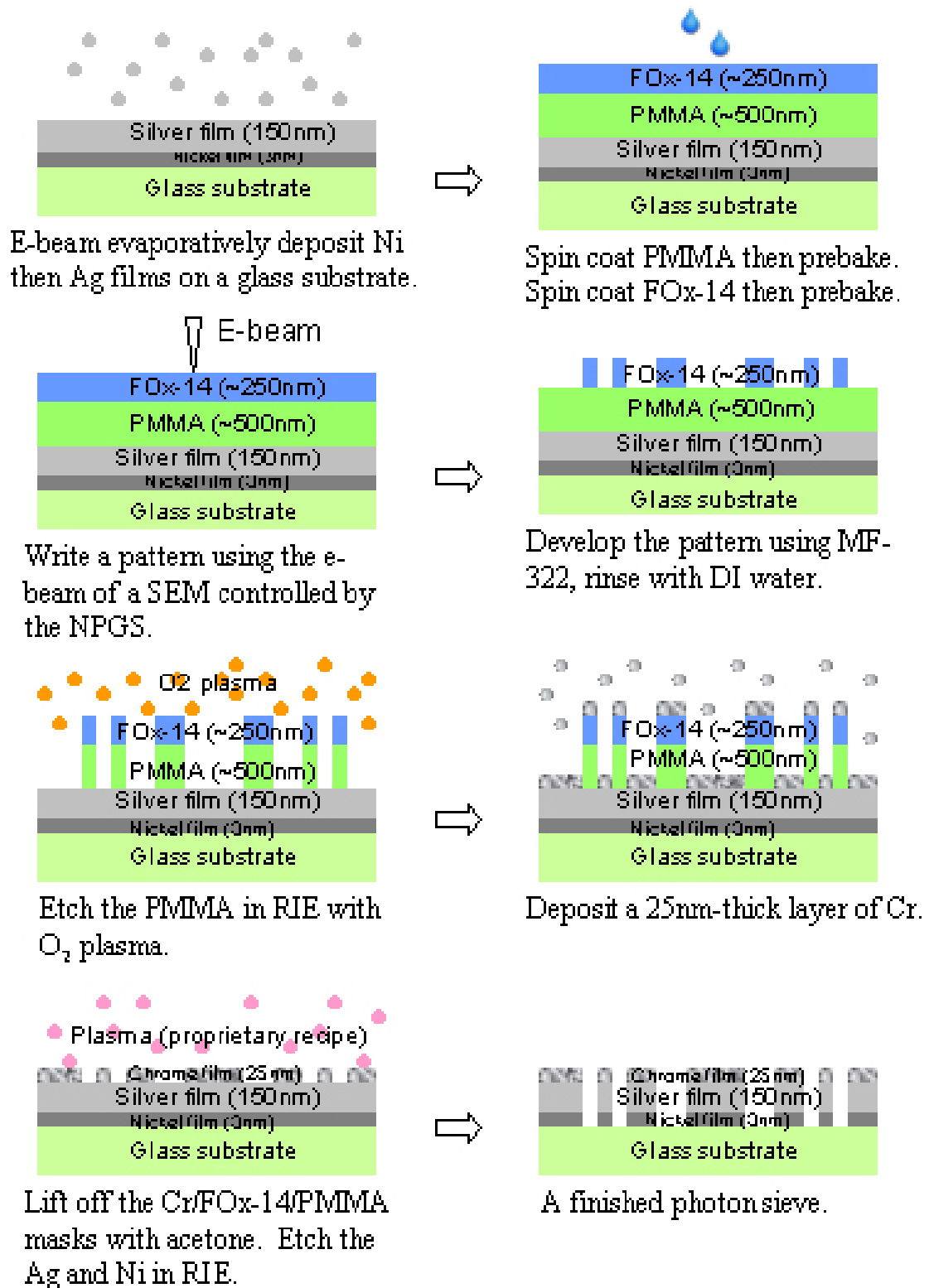


Figure 3-14. Process flow of the “reversed image etching” method. The direction of flow is from left to right, top to bottom.

This process method required a chromium film deposition and over 40 minutes of high-power reactive ion etching of silver. The whole process took about a half day longer than the other methods. In addition to the complicated process, residual dots of material, shown in Figure 3-15, observed after the etching of silver with the proprietary recipe [68] are described as below. The sizes of the residual dots were on the order of a micrometer and the dots were only distributed within the large pinholes near the center of a photon sieve. After 20 minutes of etching, the residual dots were already formed and they became bigger as etching continued. The SEM micrograph shown in Figure 3-15 was taken after 40 minutes of etching.

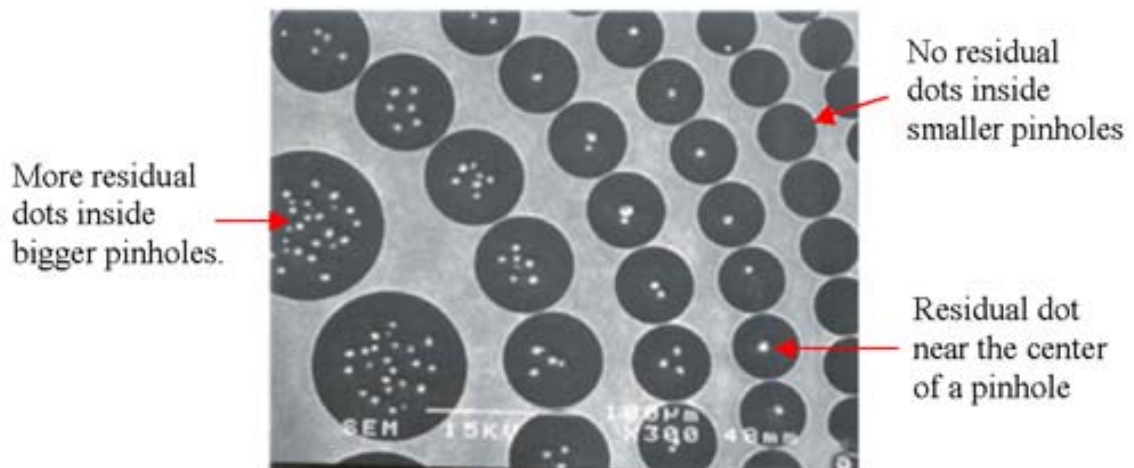


Figure 3-15. SEM micrograph of residual dots within the pinholes after plasma etching of Ag and Ni.

The composition of the residual dots was analyzed by Auger spectroscopy and evaluated by secondary and backscattered electron images in the SEM. Figure 3-16 [69] shows a schematic drawing of the interaction volume for various electron-specimen interactions. Auger emission is preferred for detection of low atomic number elements, while X-ray emission is preferred for high atomic number elements [70]. Only Auger electrons generated closed to the specimen surface can escape with their characteristic

energies and be used to identify the atoms in the specimen (10\AA from the surface in Figure 3-16).

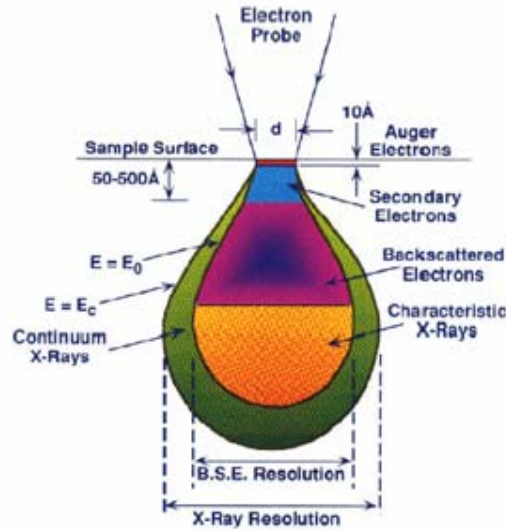


Figure 3-16. Schematic drawing of interaction volume for various electron-specimen interactions [69].

The micrographs of secondary and backscattered electron images of the residual dots are shown in Figure 3-17 (a) and (b) respectively. Both micrographs were taken at the same location with the same magnification for comparison. Secondary electron yield does not change systematically with the atomic number, Z , of the element being imaged, whereas the backscattered electron yield increases with increasing Z . Secondary electrons provide a better topographical contrast while backscattered electrons provide some information about the specimen elements [70]. From the backscattered electron micrograph, shown in Figure 3-17 (b), the residual dots appear to be hemispherical bodies with dark strips, and their appearance is very similar to those in the secondary electron micrograph, shown in Figure 3-17 (a). The information provided by the BSE micrograph confirmed that the dark strips on the residual dot consists of relatively low Z elements as compared to the rest (white part) of the hemispherical bodies.

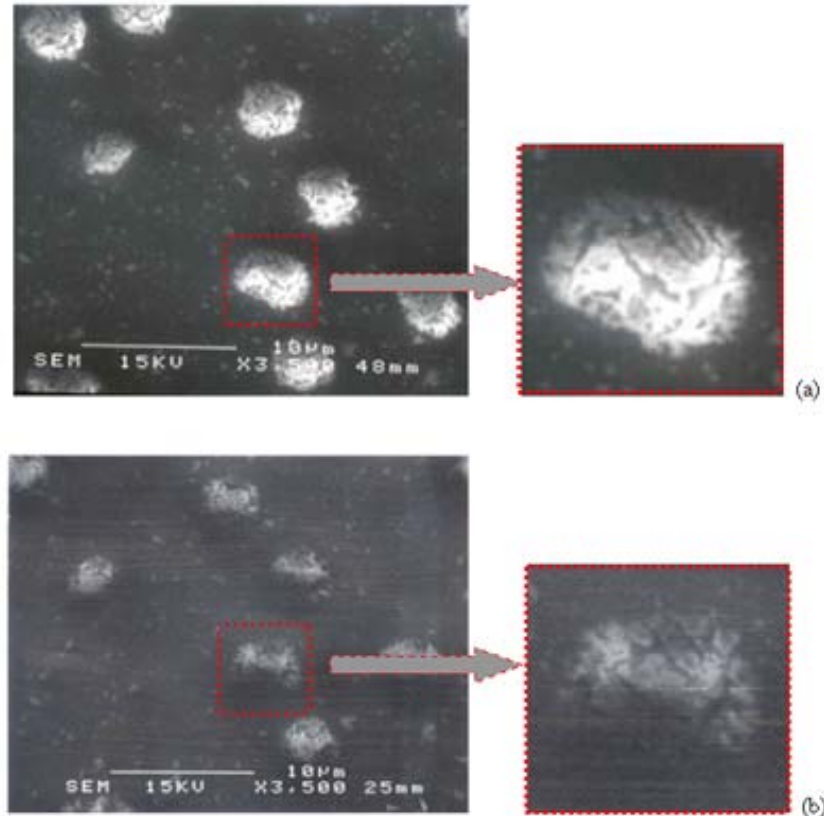


Figure 3-17. Residual dots (a) SE image (b) BSE image. SE yield does not change systematically with the atomic number, Z , of the element being imaged, whereas backscattered electron yield increases with increasing Z . BSE image confirmed the dark strips on residual dot consisted of relatively low Z element compared to the rest of hemispherical body.

The same specimen was analyzed by Auger electron spectroscopy. The Auger spectra were taken in an area with residual dots instead of from a single dot. Charging artifacts occurred when the primary beam was focused onto a single dot due to the non-conductive glass substrate underneath. Generally, the charging problem can be improved by lowering the energy of incident beam or tilting the sample. Both actions had been taken and charging still occurred, so the area of analysis was expanded to include an area of residual dots, as shown in Figure 3-18. Auger spectra before and after argon-sputtering are shown in Figure 3-19 (a) and (b), respectively. The depth profile from argon sputtering on the residual dots is shown in Figure 3-20.

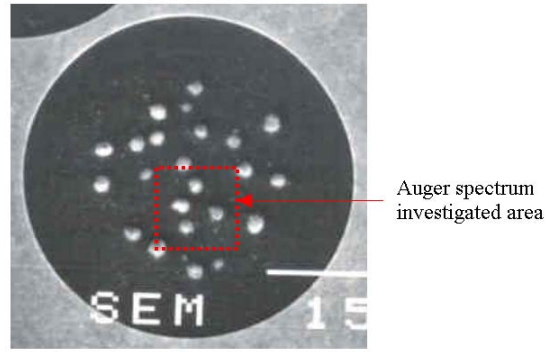


Figure 3-18. Indication of investigated area for Auger spectrum.

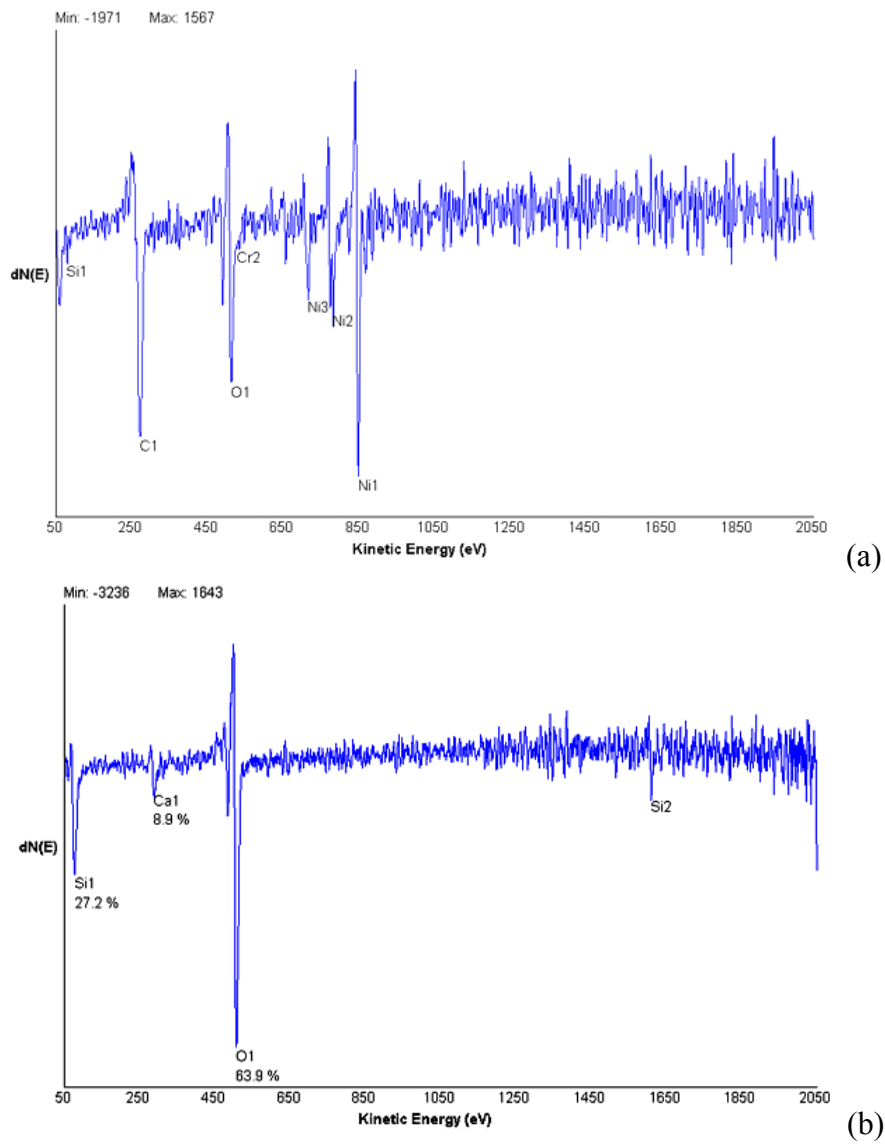


Figure 3-19. Auger spectra from a general area with residual dots (a) before argon sputter, and (b) after argon sputter.

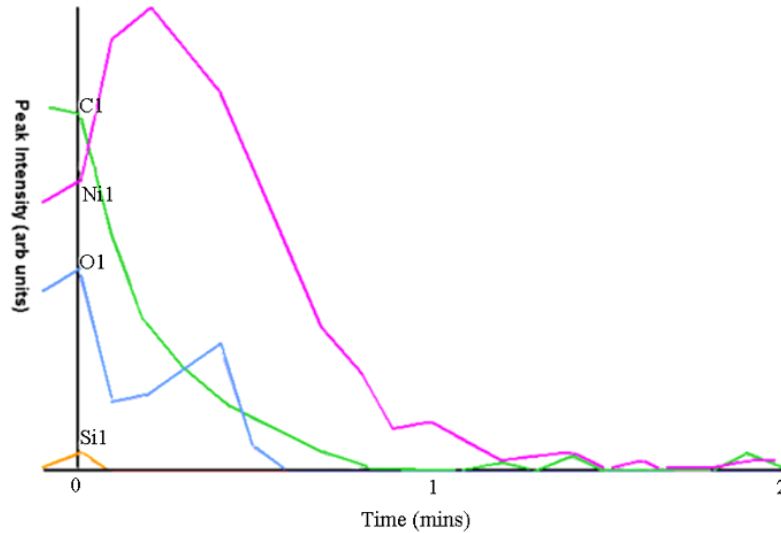


Figure 3-20. Argon sputtering depth profile from the area with residual dots.

Before argon sputtering, chromium (Cr), nickel (Ni), oxygen (O), carbon (C), and silicon (Si) peaks were found in the area with residual dots. After sputtering, Si, calcium (Ca), and O peaks were found in the same area whereas Cr, Ni, and C peaks disappeared and so did the residual dots. The strong Si and O (from SiO₂) and weak Ca peak after sputtering came from the glass substrate. The Cr, Ni, C and part of the O peaks found before sputtering are from either the residual dots or surface contaminations.

To avoid the long process time (chromium deposition and 40 minutes of RIE etching) and the possibility of residual dots formation, the lift-off process was developed.

3.2.6.2 Lift-off process

The lift-off method to fabricate PS was developed consisting of first evaporating a 30Å adhesion layer of nickel, which also served as a charge dissipation layer during e-beam lithography. The substrate was then coated, first with PMMA with a prebake at 180°C for 15 minutes, and subsequently with FOx-14 with a prebake at 180°C for 2 minutes. The FOx-14 was patterned using electron beam lithography and developed by MF-322 for 90 seconds. The unexposed FOx-14 was dissolved and the unmasked PMMA

was removed by RIE. After the etching of the PMMA, a 1000Å-thick silver (Ag) layer was deposited on the substrate by e-beam evaporation. The sample was rinsed by ultrasonication in an acetone bath (Fisher Scientific ultrasonic FS-28) to lift off the Ag/FOx-14/PMMA layers. The sample was subjected to RIE for 10 seconds to remove the thin nickel layer by argon sputtering. A schematic process flow of this method is shown in Figure 3-21.

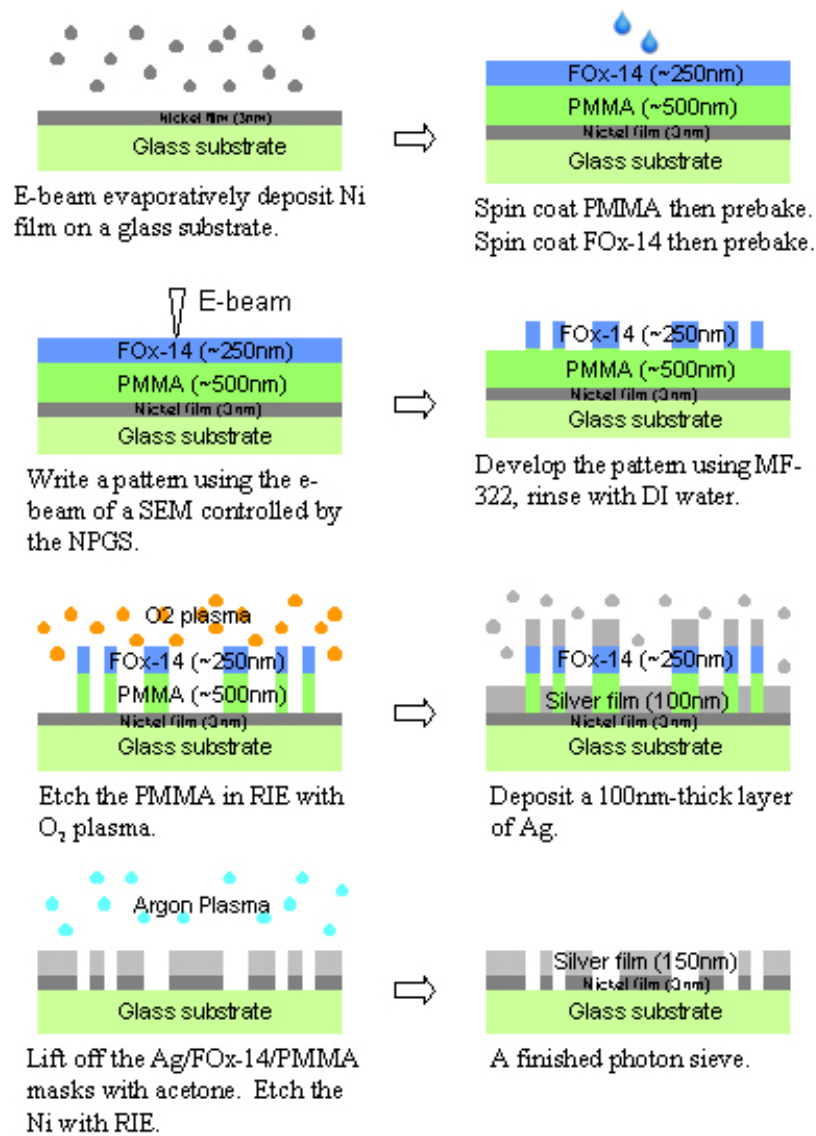


Figure 3-21. Process flow of the "lift-off" method. The direction of flow is from left to right, top to bottom.

This process method shortened the processing time by eliminating the steps of Cr deposition and 40 minutes of silver etching. However, it required a short etching of nickel by argon sputtering, which bombarded the silver surface simultaneously and caused roughening. No residual dots were observed in this process method. Figure 3-22 shows an optical micrograph of a photon sieve manufactured by the lift-off method. The sidewall residue, shown in Figure 3-23, limited the deposited thickness of silver. If the silver was too thick, it prevented the PMMA layer from being dissolved in acetone during the lift-off process. In addition, the oxygen plasma was not stable (with unknown contamination) over the time period of the process development. In order to avoid the problem of sidewall residues and the use of oxygen plasma, the process of direct wet etching was studied.

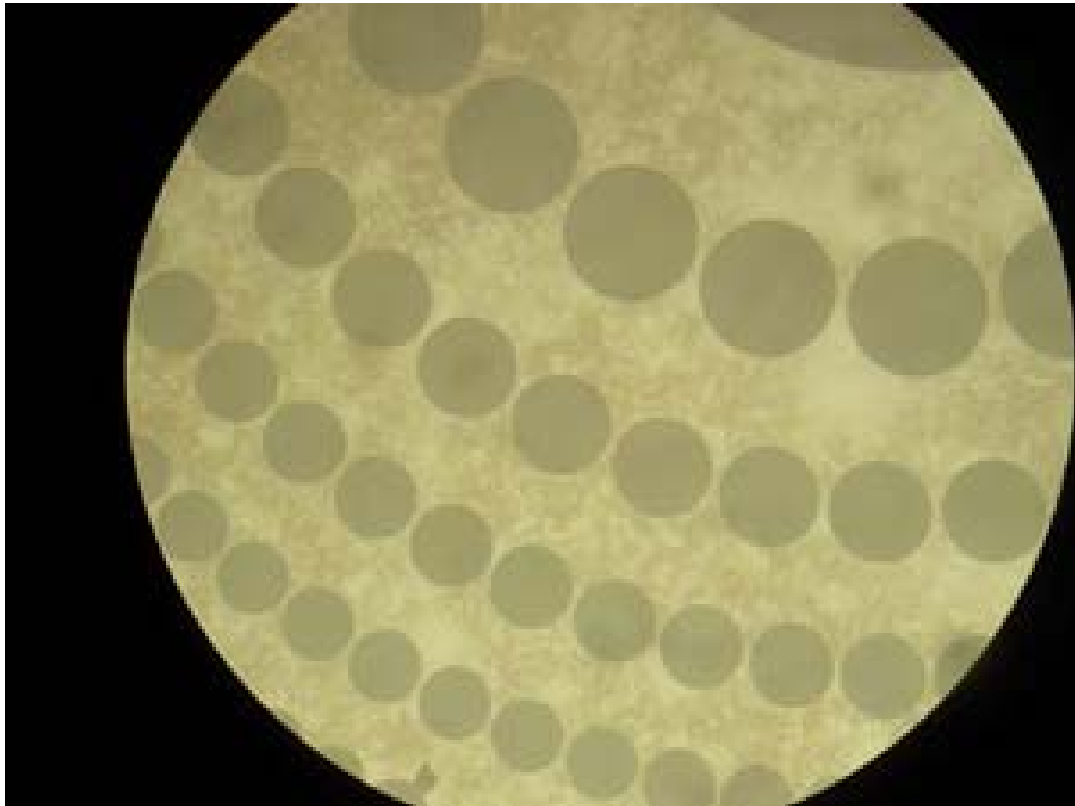


Figure 3-22. Optical micrograph of a photon sieve manufactured by the lift-off method.

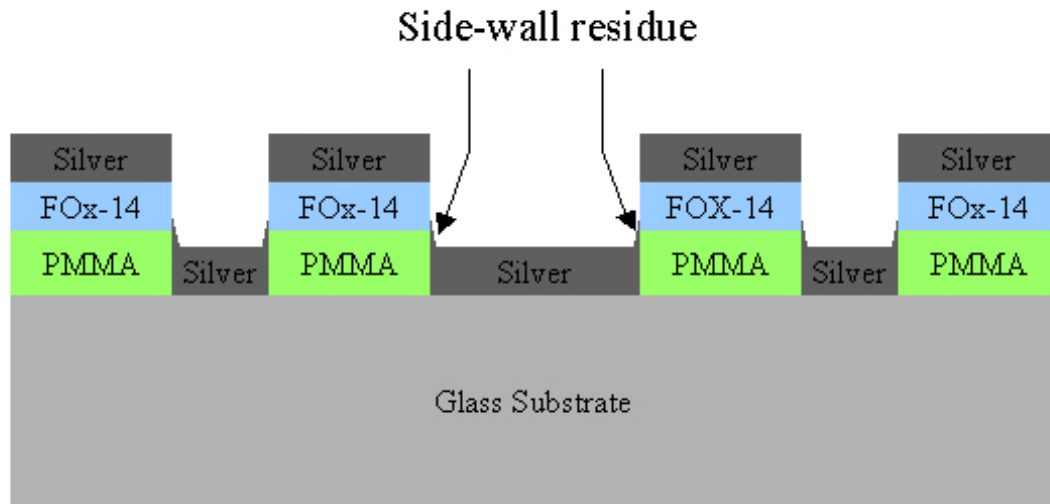


Figure 3-23. Schematic drawing of sidewall residue. Some of the deposited silver atoms stuck on the sidewall of the patterned resist and prevented the PMMA layer from being dissolved in acetone during the lift-off process.

3.2.6.3 Direct wet etching process

In the direct wet etching method, photon sieves were fabricated by first depositing by electron beam evaporation a 30Å adhesion layer of nickel, followed by deposition of a layer of silver (1500 Å) on a cleaned glass substrate. The metallized substrate was then coated with PMMA with a prebake at 180°C for 15 minutes. The PMMA was patterned using electron beam lithography and developed by MIBK:IPA (1:3) for 70 seconds. The exposed silver was etched using 12M nitric acid (HNO₃) in 1 second. The sample was rinsed with DI water twice. The PMMA was removed by rinsing with ultrasonication in an acetone bath. A schematic process flow of this method is shown in Figure 3-24.

This method was the simplest compared to other three process methods because it required neither Cr deposition nor long time RIE, and only required one spin coating of PMMA, which was used as a mask for direct wet etching. However, the quality of etching was poor. The uniformity of wet etching over different feature sizes was a

problem. Figure 3-25 shows that the large pinholes (80 μm in diameter) located in the center of the photon sieve were etched clearly while the small pinholes (10 μm in diameter) located at the outer area of photon sieve were not etched completely. In order to avoid this problem, the process of direct dry etching was studied.

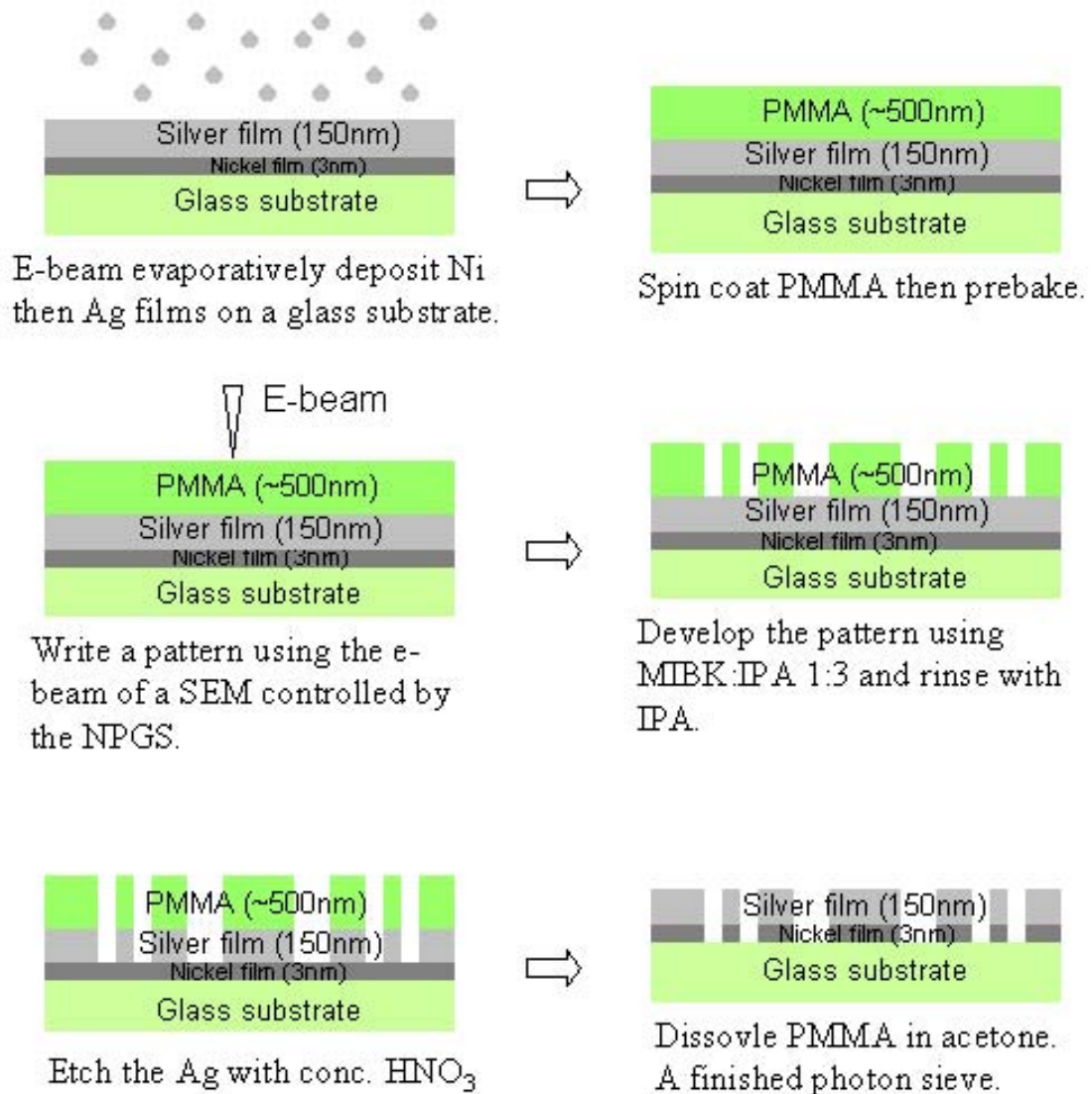


Figure 3-24. Process flow of the "direct wet etching" method. The direction of flow is from left to right, top to bottom.

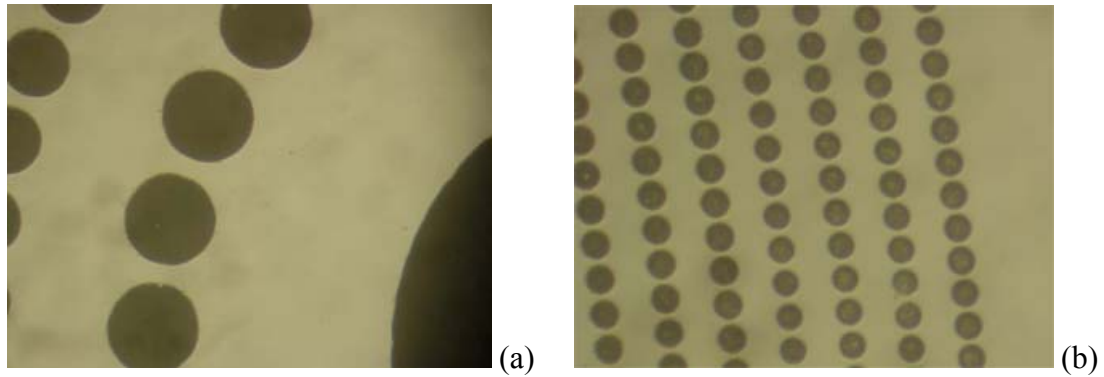


Figure 3-25. Optical micrographs of the photon sieve manufactured by direct wet etching (a) completely etched large center pinholes (80 μm in diameter), and (b) incompletely etched small outer pinholes (10 μm in diameter.)

3.2.6.4 Direct dry etching process

In the direct dry etching process, the metallized substrate (3 nm of Ni and 150 nm of Ag) was coated with PMMA and prebaked at 180°C for 15 minutes. The PMMA was patterned using electron beam lithography and developed by MIBK:IPA (1:3) for 70 seconds. PMMA was used as a mask for the RIE argon etching. The PMMA demonstrated a poor resistance to dry etching and veil-like material accumulated at the edge of each pinhole which caused the edge roughening, as shown in Figure 3-26.

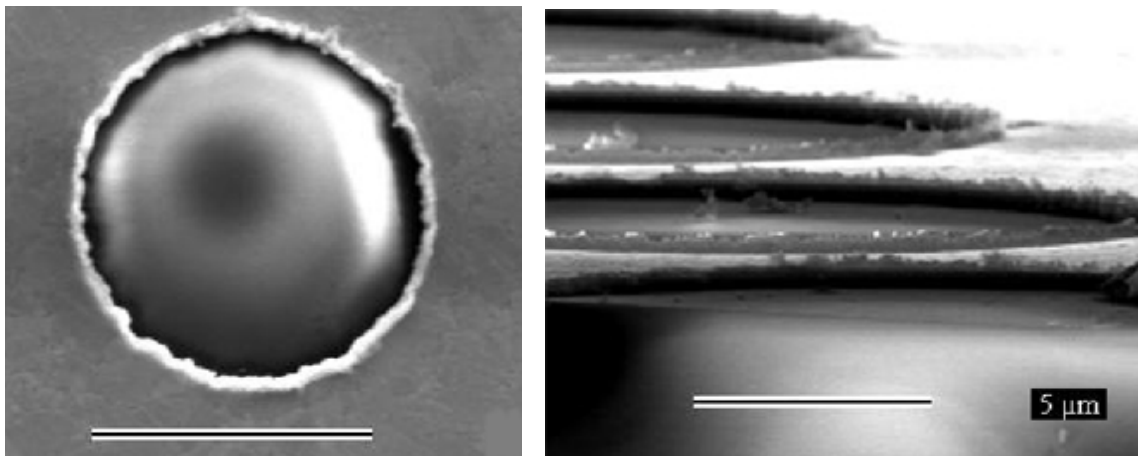


Figure 3-26. SEM micrographs of the veil-like matter at the edge of holes after argon sputtering using only PMMA for an etch mask.

Thus another positive e-beam resist, ZEP7000, was added on the top of PMMA during the coating stage. The ZEP7000 was patterned using e-beam lithography with an “area dose” of $45 \mu\text{C}/\text{cm}^2$ and developed using ZED750 for 2.5 minutes followed by a rinse in IPA. The ZEP7000 with e-beam exposure was dissolved in ZED750. The sample was subjected to argon plasma etching inside a RIE system to etch away the exposed PMMA, silver, and nickel layers. The PMMA and ZEP7000 coatings were then removed by ultrasonicing in acetone. Use of this procedure resulted in clean edges as shown in Figure 3-27. A schematic process flow of this method is shown in Figures 3-28. The direct dry etch process using PMMA plus ZEP7000 was selected to be the standard process to make single- or dual-wavelength photon sieves. No chrome coating and oxygen plasma etching were needed and the silver-etching step took only 30 second rather than 40 minutes as in the reverse image method.

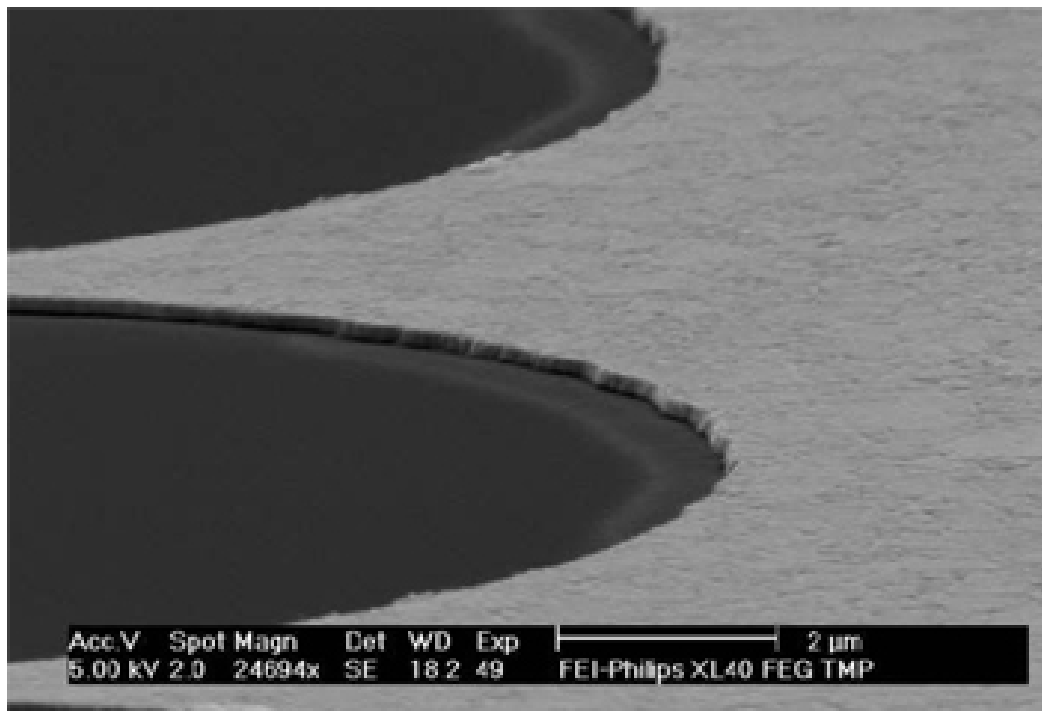


Figure 3-27. A photon sieves with clean edge manufactured by direct dry etching method.

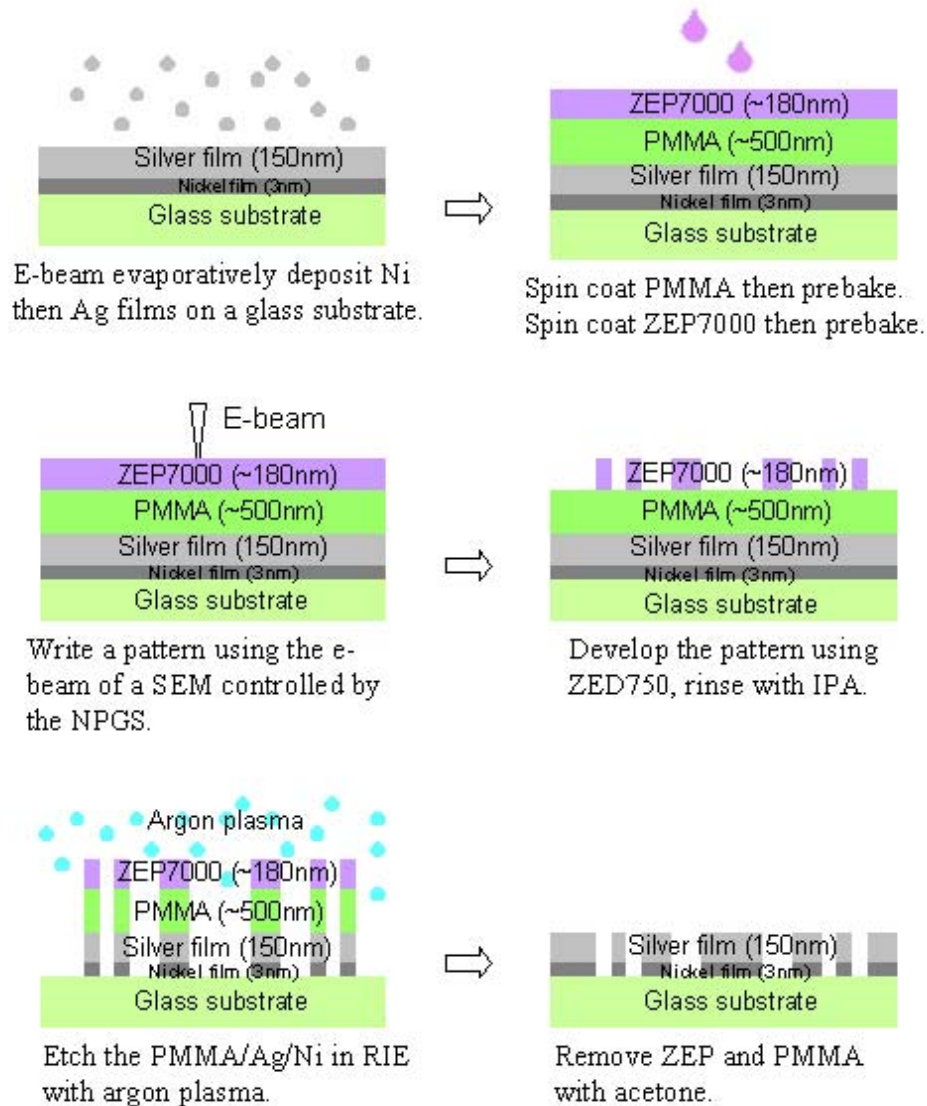


Figure 3-28. Process flow of the “direct dry etching” method. The direction of flow is from left to right, top to bottom.

3.3 Discussions

In the reversed image etching process (section 3.2.6.1), the reason for the excellent selectivity of Cr over Ag with the proprietary $H_2/Ar/CH_4$ RIE recipe [68] is still not clear. It is speculated that the silver atoms and the hydrogen or hydrocarbon molecules form organometallic complexes. Hydrogen atoms and linear or cyclic hydrocarbon groups with π -bond systems, such as ethylene ($H_2C=CH_2$), acetylene ($HC\equiv CH$), π -allyl (C_3H_5),

cyclopentadienyl (Cp, C₅H₅) and benzene (Ph, C₆H₆) are very common ligands in organometallic complexes [71] and are possible to form during the plasma discharge. Because the bonding between silver and carbon or hydrogen is thermodynamically weak [72], the organometallic complexes tend to undergo homolytic dissociation [73], which results in metal and hydrocarbon radicals and been removed by turbopump. The purpose of adding argon atoms in the proprietary recipe [68] is to stimulate the gas-solid reactions, i.e., to remove deposited polymer and increase the etching rate [48].

It is reasonable to speculate that the most probable mechanism of formation of the residual dots formation during RIE of PSs is primary particle agglomeration during plasma etching. This mechanism is consistent with the results shown in section 3.2.6.1. These particles stick onto the substrate surface after the plasma is turned off. Particles can be produced in many ways, such as flaking from substrate or chamber walls, metal clustering and polymerization of the gases or substrate materials, condensation of sputtered material, and aerosols from gases [74-77]. Yellow colored polyimide was found to built-up on the sidewall of the reaction chamber as a result of contamination from other users of the RIE system. This polyimide may flake and become contaminate particles. In addition to contamination from chamber built-up, re-deposited metal atoms, such as Cr and Ni, and polymers formed from CH₄/H₂ radicals and atoms are all possible sources of primary particles.

The mechanism of particle growth during RIE has been investigated by many researchers [74-77]. It is believed that the nanometer size crystallites can be formed and may coalesce into particles when the concentration of crystallites reaches a critical value. The particles further grow by molecular bonding with surface atoms and radicals from

the plasma and formed primary spherical particles about 0.2 μm in size [76]. These primary particles undergo clustering or agglomeration and form large particles about 2~5 μm [76].

From the Auger spectra (Figure 3-22), Cr, Ni, and C peaks were found before sputtering and the peaks and residual dots were absent after sputtering. This suggests that the residual dots contained these three elements. In the reversed image etching process, the final layers exposed to plasma etching were the Cr hard mask and the Ni adhesion layer. It is speculated that these two metal atoms combined with the C from contamination and polymerization were bonded onto the nanoparticles that underwent agglomeration and formed the residual dots.

From the Auger data (Figure 3-22), no silver peak was found in the residual dots. A possible reason is that the silver atoms and the hydrogen or hydrocarbon molecules within the etch gases formed the organometallic complexes that were removed by the vacuum system. It is also possible that some of the silver atoms re-deposited back onto the substrate and were covered by the molecular bonded Cr, Ni, and C elements. As long as the coating of Cr, Ni, and C was thicker than 30 \AA , Auger electrons from the inner portion of the residual dots would not be detected in the Auger spectra.

3.4 Conclusions

Four process methods for photon sieve fabrication were developed and tested. The advantages and disadvantages of each method were described and compared.

First, the reversed image etching method was successful but complicated. It was accomplished by reactive ion etching with a patented RIE recipe to pattern Cr hard masks [68]. The reverse image etching method required deposition of a chromium film over the

Ag film and more than 40 minutes of high-power reactive ion etching (RIE) of silver, which makes this process longer than the other methods. The photon sieves obtained from this method were good, but residual dots within the open holes of photon sieves were observed. It is speculated that the residual dots were formed by primary nanoparticles agglomerating during the plasma etching.

To simplify the process flow and avoid the possibility of residual dots formation, the lift-off method was developed. Good photon sieves were produced by using this method. However, sidewall residue of silver atoms stuck on the patterned resist limited the deposited thickness of silver.

To avoid the problem of sidewall residue and the use of unstable oxygen plasma in the RIE system, the direct wet etching method was studied. The direct wet etching method was simple and fast. However, the manufacturing result was not promising due to the non-uniform etching rate for different sizes of mask openings.

The direct dry etching method was developed to solve the non-uniform etching problems of wet etching. PMMA was shown to be a poor mask for argon sputtering due to residual deposits at the edge of holes. A positive e-beam resist, ZEP700, was used on top of the PMMA because of its excellent dry etching resistance. The direct dry etching method combined with ZEP7000 resulted in the most successful process method in terms of simplicity and repeatability for production of photon sieves.

CHAPTER 4 PHOTON SIEVE PROPERTIES

4.1 Introduction

Refractive optics have long been used for imaging, especially for visible light. However, high absorption coefficients for lens materials limit the use of refractive optics for short wavelengths. Diffractive lenses, for instance Fresnel zone plates (FZP) and photon sieves (PS), are attractive not only because they can be used to focus high or low energy radiation but also because of their small size and weight.

A photon sieve is a diffractive lens composed of many pinholes distributed in the all-even or all-odd Fresnel zones. The lens properties of diffraction optics are wavelength-dependent. If photons with wavelengths different from the designed value pass through a diffractive lens, aberration will occur.

In this research, multiple patterns of dual-wavelength photon sieves were designed, fabricated and tested to characterize the lens properties. The fabrication process of direct dry etching with ZEP7000 e-beam resist, described in Chapter 3, was used. The purpose of this research was to evaluate the advantages and disadvantages of dual-wavelength PS lenses and to verify the feasibility of combining the two diffractive elements for different wavelengths into a single lens. It will be concluded that a single-wavelength PS would be a good focusing filter for polychromatic light since it only focuses the designed wavelength and disperses the rest of the wavelengths. In addition, a dual-wavelength PS is inferior to the single-wavelength PS under monochromatic and polychromatic light sources. However, the dual-wavelength PS is able to focus the image with limited

performance when switching between different light sources and can be used for the imaging device that does not require the filtering of polychromatic light at the cost of intensity.

4.2 Simulation of Photon Sieves Properties

The fundamental theories of Fresnel zone plates and photon sieves have been reviewed in Chapter 2. The photon sieves used in this research were all designed to have a focal length of 50 mm, a lens diameter of 3 mm, a K-factor of 1.2 (the ratio of pinhole diameter over the zone width, i.e., the d/w ratio in section 2.4.1.2), and they were all apodized as discussed below. These factors were determined by simulated results reported by O. Shenderova [43-45]. The simulations were performed using MATLAB-based software [78]. Fresnel-Kirchhoff diffraction theory [9] was used for the large pinholes, while the analytical far-field based expression [28] was used for small pinholes [45]. The point spread function (PSF) on the image plane of a point source was computed to optimize the lens properties. A small full width half maximum (FWHM) and large intensity of the PSF at the focal point were the characteristics used to determine the quality of the design.

4.2.1 Focal Length and Lens Diameter

The two wavelengths that were chosen for the dual-wavelength design were 500 nm and 600 nm. The difference between these two wavelengths is big enough to minimize the influence of each other but is within the visible spectrum for regular photography. Equations 2-12 and 2-13 in Chapter 2 show that once the wavelength and focal length were determined, the lens diameter and the resolution (outermost zone width) were dependent on each other. The bigger the lens diameter, the narrower the outer-most zone width, the better the resolution. One of the simulation results [43]

showed that a photon sieve with a 3 mm diameter had a smaller PSF FWHM than a 1 mm diameter with the same focal length. A smaller FWHM represents a better optical resolution as defined by the Rayleigh Criterion [9] in section 2.3.1.

4.2.2 K-factor

The K-factor is the d/w ratio described in Figure 2-23 and equation (2-20), where d is the pinhole diameter and w is the zone width. According to the simulation results shown in Figure 4-1, 1.2 is a reasonable K value where the peak intensity of the PSF is a maximum while the FWHM is acceptably small.

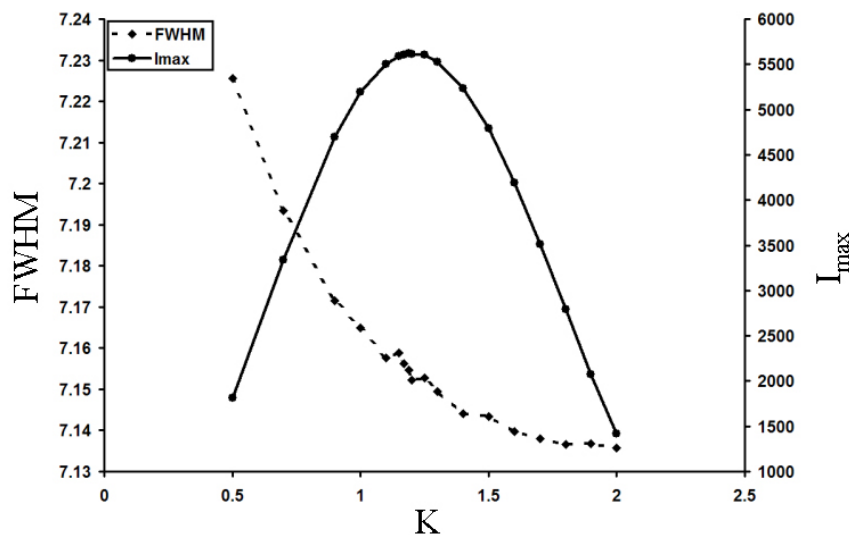


Figure 4-1. Simulation result of the optimum K value. The horizontal axis is the K value, the vertical axis at left is the FWHM in micrometers, and the vertical axis at right is the intensity in arbitrary units [44].

4.2.3 Apodized vs. Unapodized Photon Sieves

As reviewed in section 2.4.3, apodization is the process of modulating the pinhole density on each ring of a photon sieve to create a smooth transmission window and thereby suppress the secondary maxima in the diffraction pattern. The simulated PSFs for apodized (modified Gaussian function; see below) and unapodized photon sieves are shown in Figure 4-2. The apodized photon sieve exhibited better contrast (Equation 2-

21) despite the fact that the absolute transmission (not shown) was about one half of the unapodized lens. The low transmission of an apodized photon sieve was mainly due to fewer holes (2722 pinholes for the unapodized photon sieve and only 818 pinholes for the apodized lens).

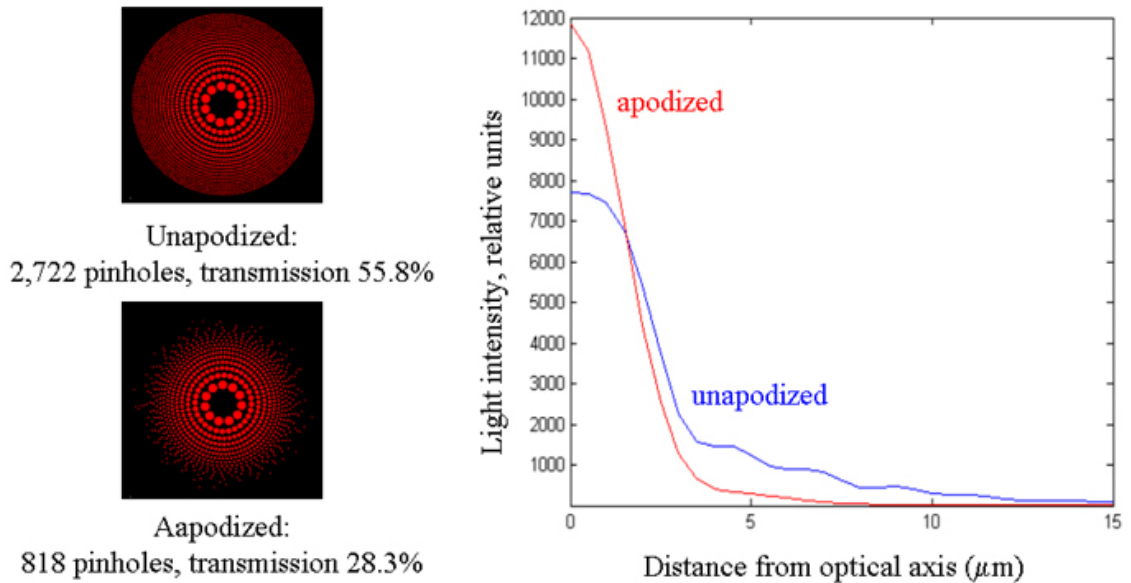


Figure 4-2. Simulated one-dimensional PSFs for apodized and unapodized photon sieves. The light intensity at the vertical axis is in arbitrary units. The absolute intensity for apodized photon sieve is lower than the unapodized one [45].

Figure 4-2 also showed that the secondary maxima in the PSF of an unapodized photon sieve was suppressed by the apodization. The apodization function used for simulation was a modified one-dimensional (1D) Gaussian distribution function, equal to $\exp(-ax^b)$ [44]. The appropriate values of the Gaussian parameters a and b were chosen to reduce the FWHM and increase the intensity for a lens with specific geometric parameters. A typical simulation of the FWHM as functions of a and b is shown in Figure 4-3. It is an example to illustrate that apodization is a compromise between resolution and transmittance. The smallest FWHM was obtained when $a = 15$ and $b = 3.6$ while the peak intensity (I_{\max}) was low with the same a and b parameters.

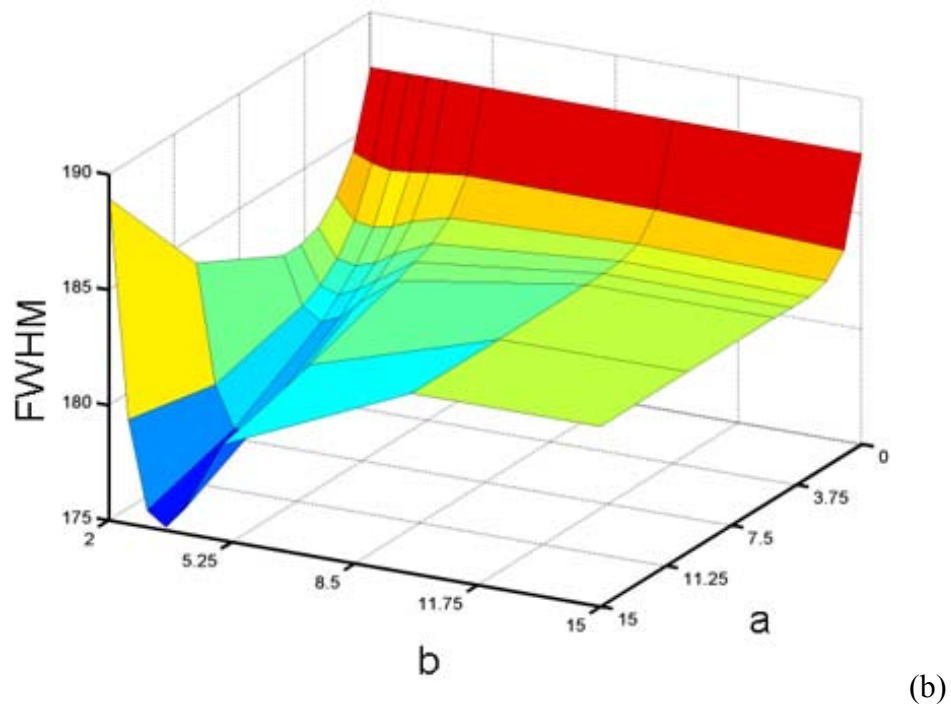
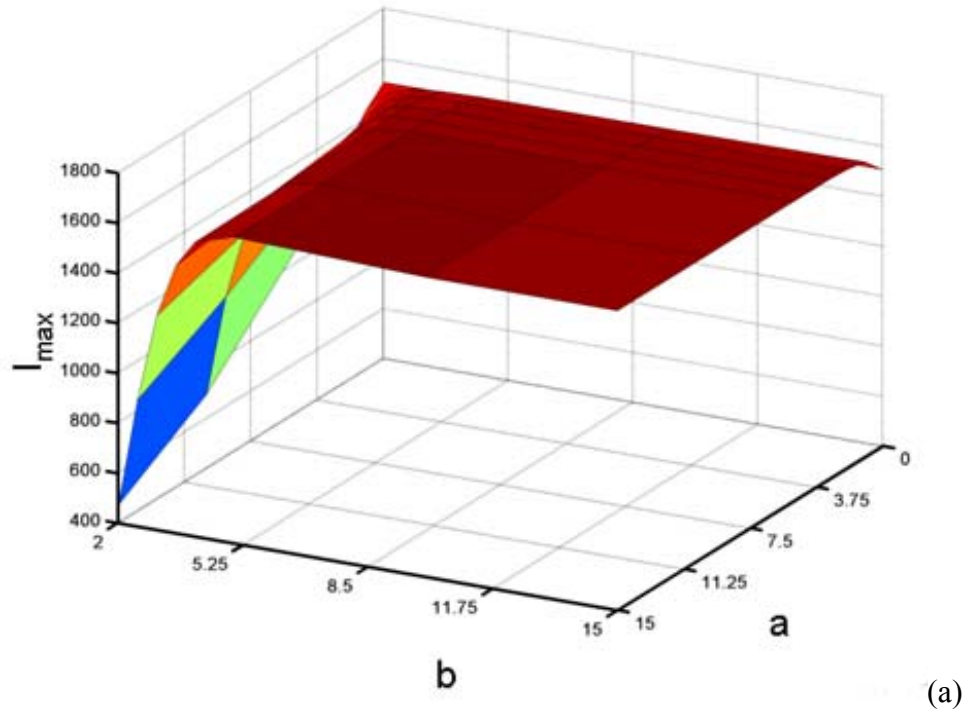


Figure 4-3. A simulation of the PSF (a) peak intensity and (b) FWHM as a function of a and b , the coefficients of a modified Gaussian distribution function, $\exp(-ax^b)$. In this example, the smallest FWHM was obtained when a equaled to 15 and b equaled to 3.6. However with $a = 15$ and $b = 3.6$, the intensity became low. This demonstrated that apodization is a compromise between resolution and transmittance [44].

4.3 Photon Sieve Pattern Generation

The patterned photon sieves were generated by the direct dry etching process described in section 3.2.6.4. The positions of the holes in the PS were generated by entering the desired wavelength, focal length, and lens diameter into the MATLAB-based software. This software generated the hole pattern of single-wavelength photon sieves in a text format containing the X, Y coordinates of the center of each hole and its radius (μm). The text file was inputted into DesignCAD which generated a file for electron beam patterning, that was then loaded into the NPGS for electron-beam lithography.

An example of the text file for a **6-sector** dual-wavelength photon sieve (see below) is shown in Table 4-1. Only the first 9 and last 9 pinholes of each wavelength (500 nm or 600 nm) are shown in the table. The pinhole sequence numbers show that pinholes from 1 to 5280 are for 500 nm light, and pinholes from 5281 to 8973 (3693) are for 600 nm light. The smallest pinhole diameters for 500 nm and 600 nm wavelengths are 10.14 μm and 12.66 μm , respectively. The pinhole pattern of a 6-sector dual-wavelength photon sieve is shown in Figure 4-4. If only the 500 nm pinholes or 600 nm pinholes are used individually, two 3-sector single-wavelength photon sieves, shown as **505** and **605** in Figure 4-5, were formed, with the other 3 sectors remaining unpatterned.

There were a total of thirteen (13) designs of photon sieves patterns used in this research. These patterns are shown in Figures 4-5 and 4-6 and their designated names are shown in bold-faced when used in the text throughout this chapter. The nomenclature used in the names is that the first number (5 or 6) designates the wavelengths of 500 nm and 600 nm. For single-wavelength photon sieve patterns, the second and third numbers indicated the pattern is a complete photon sieve (10) or a half one (05, 3-sectors). For

dual-wavelength photon sieve patterns, the sectional designs were named directly with the number of sectors and the concentric designs were named with the ratios of open hole area of the two wavelengths. For example, **5in6-75%** means that the blue (500 nm) holes are in the center of the concentric designed dual-wavelength PS with nominally 75% hole area and red holes (600 nm) are in the outer zone with 25% hole area.

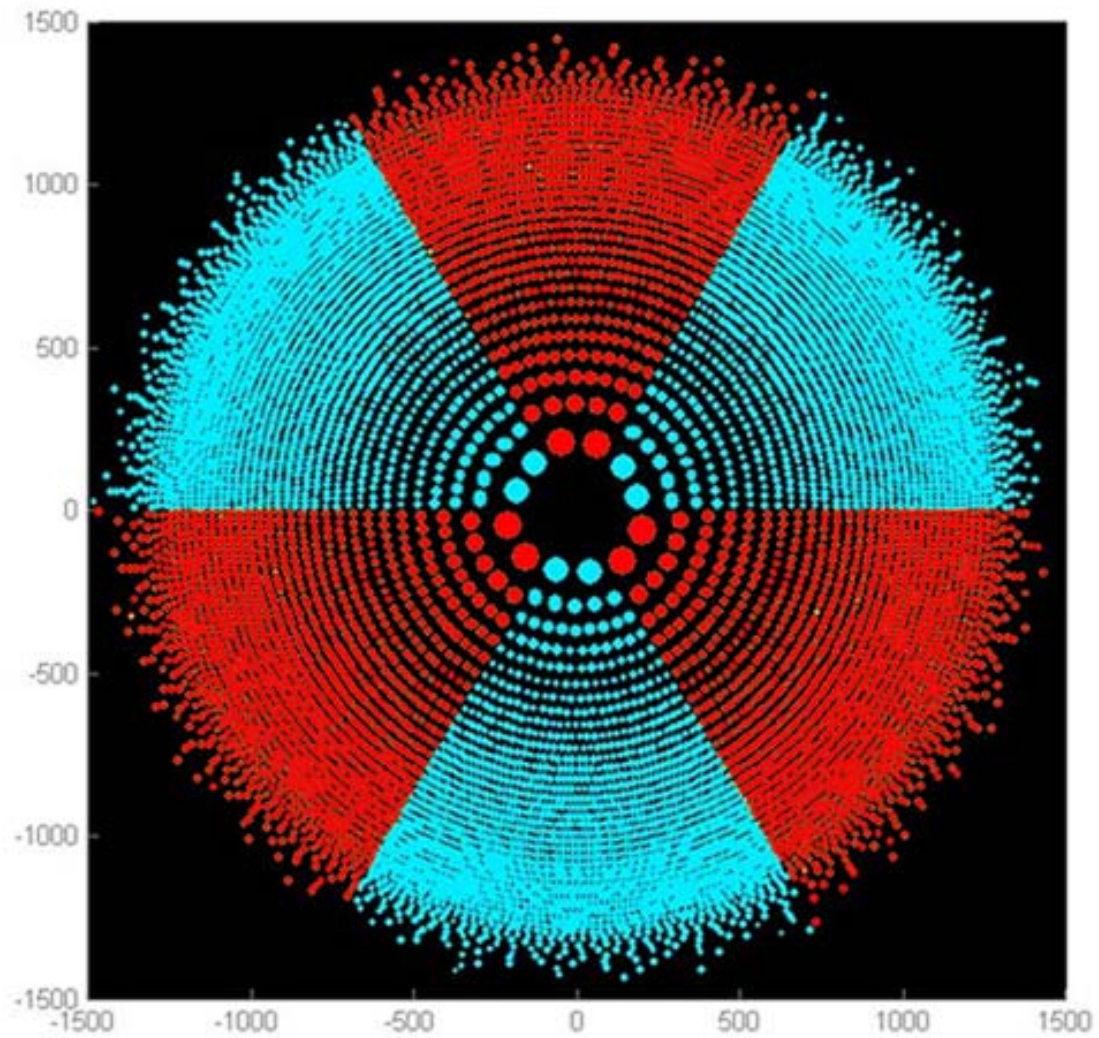


Figure 4-4. The DesignCAD pattern of the **6-sector** dual-wavelength photon sieve. Blue and red pinholes are designed to focus 500 nm and 600 nm wavelengths, respectively.

Table 4-1. Text file of the **6-sector** dual-wavelength photon sieve. Only the first 9 and last 9 pinholes designed for 500 nm and 600 nm wavelengths are shown in the table.

Pinhole Sequence	X (um)	Y(um)	Radius (um)	Wavelength (nm)
1	189.27	40.93	39.3	500
2	143.45	130.09	39.3	500
3	294.51	27.68	25.42	500
4	282.32	88.31	25.42	500
5	257.79	145.07	25.42	500
6	221.99	195.5	25.42	500
7	176.49	237.38	25.42	500
8	370.23	20.74	20.25	500
9	365.32	63.58	20.25	500
~	~	~	~	~ 500
~	~	~	~	~ 500
5272	195.54	-1414.1	5.26	500
5273	438.12	-1358.66	5.26	500
5274	667.39	-1261.94	5.26	500
5275	-352.06	-1401.42	5.19	500
5276	148.49	-1437.32	5.19	500
5277	631.13	-1299.85	5.19	500
5278	-370.33	-1414.5	5.13	500
5279	386.54	-1410.16	5.13	500
5280	718.71	-1292.84	5.07	500
5281	63.56	202.39	43.05	600
5282	-46.15	207.05	43.05	600
5283	129.41	297.07	27.85	600
5284	64.82	317.49	27.85	600
5285	-2.61	324.03	27.85	600
5286	-69.92	316.41	27.85	600
5287	-134.17	294.95	27.85	600
5288	181.64	363.33	22.18	600
5289	138.23	381.96	22.18	600
~	~	~	~	~ 600
~	~	~	~	~ 600
8965	1011.03	-1001.61	6.33	600
8966	1169.6	-810.83	6.33	600
8967	1292.63	-595.41	6.33	600
8968	1376.39	-361.9	6.33	600
8969	1418.32	-117.4	6.33	600
8970	971.07	-1068.86	6.23	600
8971	1278.08	-672.27	6.23	600
8972	1430.93	-194.6	6.23	600
8973	738.09	-1265.18	6.15	600

4.3.1 Single-wavelength Photon Sieve

Figure 4-5 shows four schematic patterns of single-wavelength photon sieves. The red pinholes represent those designed to focus 600 nm light, while the blue ones are designed to focus 500 nm light. Table 4-2 shows the number of holes and the open hole area for the four single-wavelength photon sieves and one of the dual-wavelength photon sieve, 6-sector.

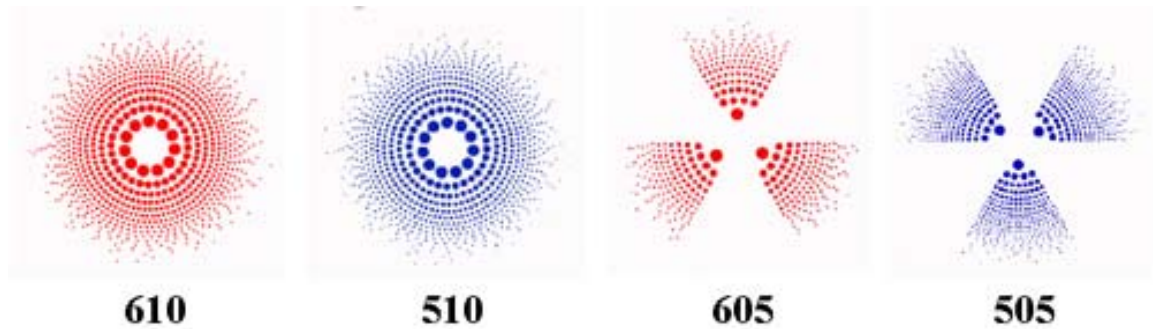


Figure 4-5. Schematic drawing of single-wavelength photon sieve patterns. Red and blue pinholes are the pinholes designed to focus 600 nm and 500 nm wavelength, respectively. Combining **605** and **505** can result the pattern of **6-sector**, as shown in Figure 4-6.

Table 4-2. Number of holes and open hole area for the 4 single-wavelength photon sieves and **6-sector** (the combination of **605** and **505**). The percentage of open hole area are the ratio of open hole area of a specific PS over the one of **610** (**610** was set to be 100%).

	610	510	605	505	6-sector
number of holes	10653	7478	5280	3693	8973
open hole area (μm^2)	2228306	2219339	1106907	1102851	2209758
% of open hole area	100	99.6	49.7	49.5	99.2

Though the number of holes for **610** and **510** are quite different (7478 in **610** and 10653 in **510**), the open hole area for the two complete PS are very close to each other (only 0.4 % difference). Lenses **605** and **505** (3-sector) are half of the complete single-wavelength photon sieves (percentage of open hole area is greater than 49.5%). The open hole area of the 6-sector is 0.8% smaller than that of 610 due to the sectional boundaries,

where no open holes are placed. The open hole area for the photon sieves is slightly different, but the difference is less than 1%. An optical micrograph of a 605 lens is shown in Figure 4-6. Combining the designs of lenses 605 and 505 results in the 6-sector dual-wavelength photon sieve pattern, as discussed above and shown in Figures 4-4 and 4-7.

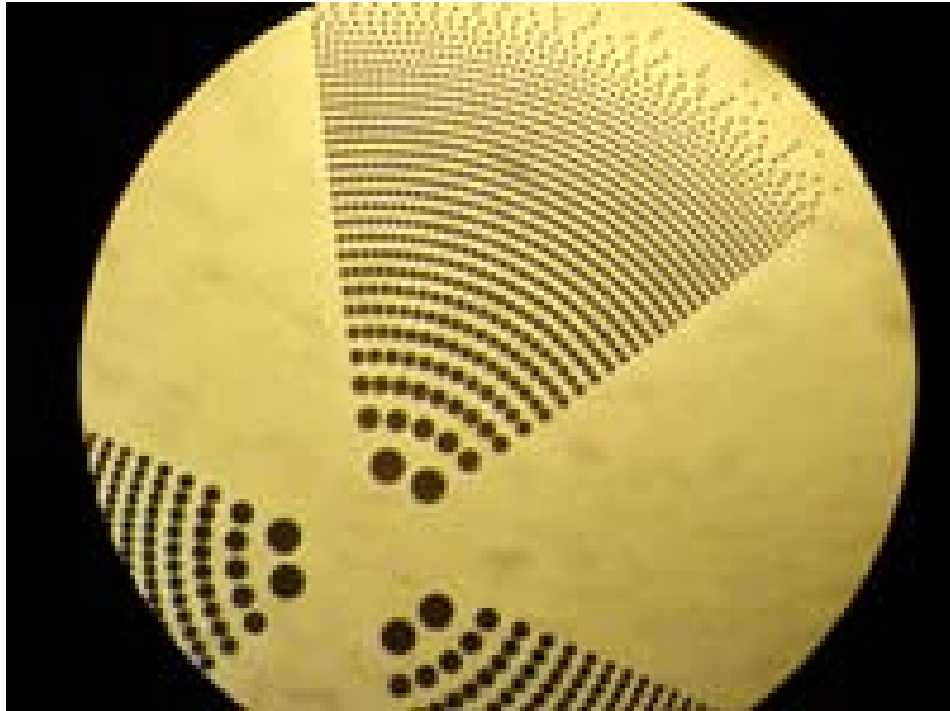


Figure 4-6. Optical micrograph for the **605** single wavelength photon sieve.

4.3.2 Dual-wavelength Photon Sieve

Dual-wavelength patterns were generated with either a sectional or concentric designs. They are shown schematically in Figure 4-7. As before, red and blue pinholes are designed to focus 600 nm and 500 nm light, respectively. The dual-wavelength photon sieve patterns were generated by combining the hole pattern of the two single-wavelength patterns, **610** and **510** in Figure 4-5, with different sector numbers for the sectional designs or area ratios for the concentric designs. Optical micrographs of the **6-**

sector and **5in6-70%** lenses are shown in Figure 4-8. The area ratios shown in the concentric dual-wavelength PSs are rounded percentages based on the radii of the areas containing holes for either 500 nm or 600 nm light. The actual ratios of the open hole areas for the 500 nm and 600 nm pinholes are 51.1% for **6in5-50%** for 500 nm designed pinholes (48.9% for 600 nm designed pinholes).

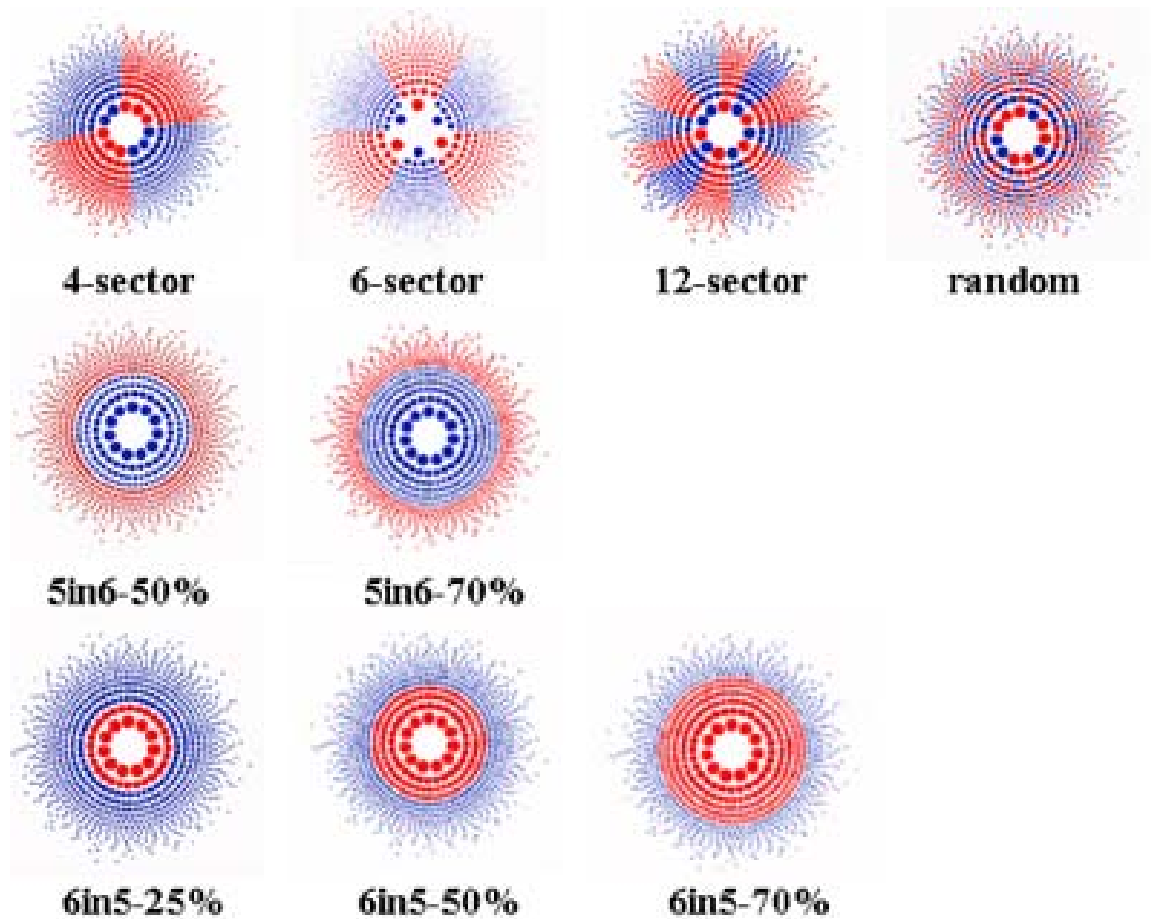


Figure 4-7. Schematic drawing of dual-wavelength photon sieve patterns. Red and blue pinholes are designed to focus 600 nm and 500 nm light, respectively. The percentage shown in the concentric pattern name indicated the area occupied by holes with the wavelength design for the center zone. For example, **5in6-70%** means that the blue (500 nm) holes are in the center of the concentric designed dual-wavelength PS with nominally 70% hole area and red holes (600 nm) are in the outer zone with 30% hole area. The actual percent of open area of holes are very close to these nominal values.

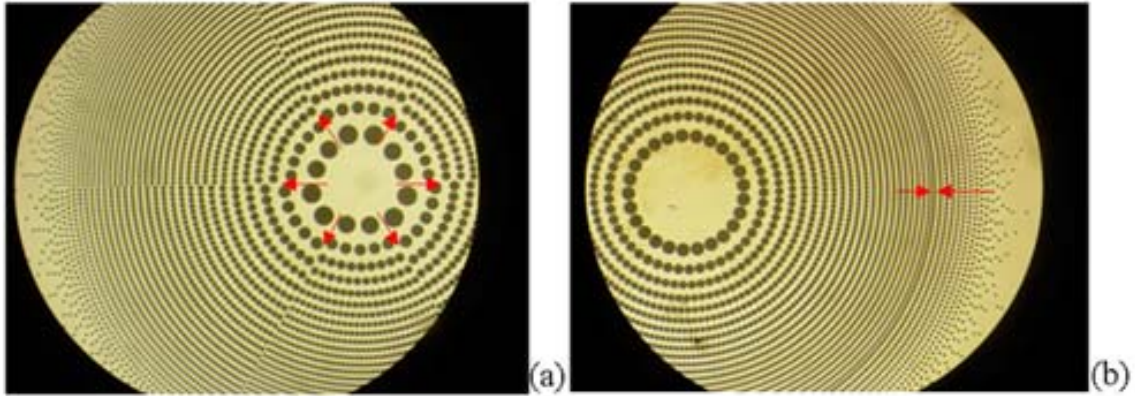


Figure 4-8. Optical micrographs of dual-wavelength photon sieves (a) **6-sector** (b) **5in6-70%**. The red arrows indicate the boundaries between 500 nm and 600 nm pinholes.

4.4 Characterizations

The two primary characteristics used to evaluate the quality of a photon sieve were the FWHM and peak intensity of the corresponding point spread function (PSF). The PSF of each photon sieves was measured with a modified Perkin-Elmer 16U grating spectrometer with a charge-coupled device (CCD) camera. The Perkin-Elmer 16U grating spectrometer, the CCD camera, and the measurements of focal length and PSF are explained in the next three sections below.

4.4.1 Perkin-Elmer 16U Grating Spectrometer

A schematic drawing of the modified Perkin-Elmer 16U grating spectrometer is shown in Figure 4-9. It was capable of measurements in the near-infrared (NIR), visible, and ultraviolet (UV) regions from wavelengths of 2600 nm to 220 nm ($3800 \text{ cm}^{-1} \sim 45000 \text{ cm}^{-1}$; $0.5 \sim 5.8 \text{ eV}$). The system consists of multiple light sources, a grating monochromator, and a series of mirrors allowing collection of transmission data with two photon detectors or measurement of the PSF with a CCD camera. The transmission and the PSF arrangements are shown as (A) and (B), respectively, in Figure 4-9.

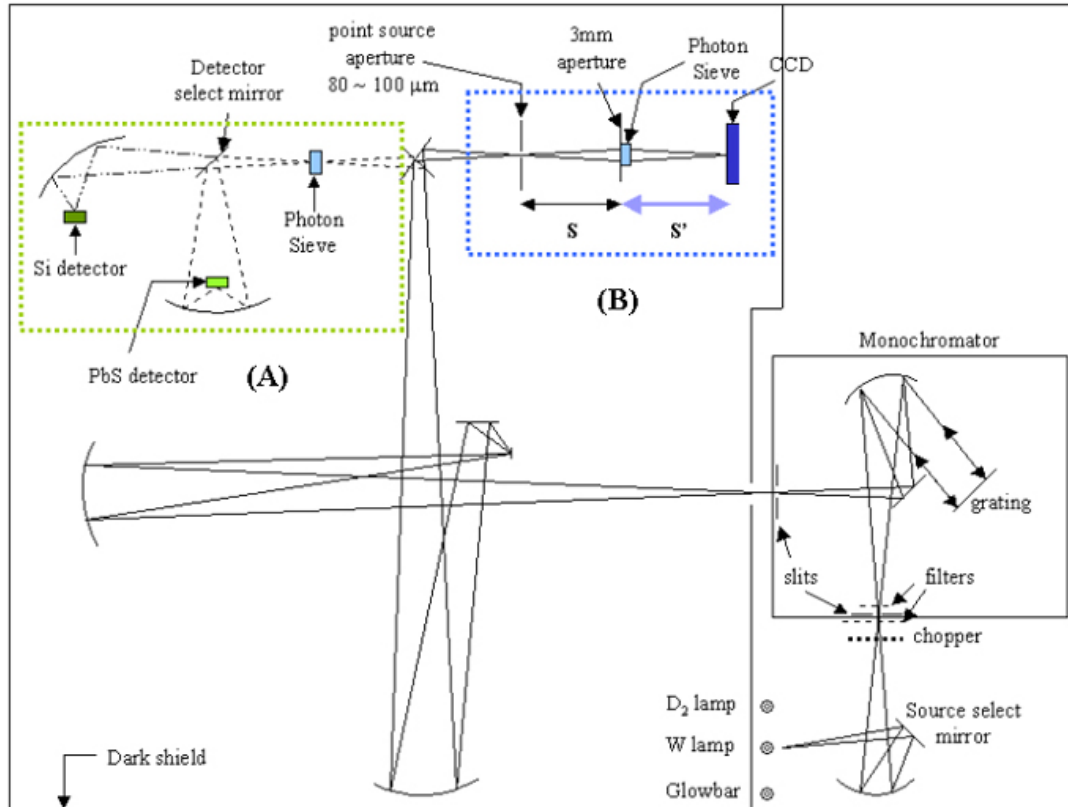


Figure 4-9. Schematic drawing of the modified Perkin-Elmer 16U grating spectrometer. Part (A) and (B) are used to measure transmission and PSF, respectively.

The light sources used for NIR to visible, and UV regions were a tungsten (W) lamp or a deuterium (D₂) lamp, respectively. The tungsten lamp was used to characterize PS lenses designed for 500 nm and 600 nm. The illumination spectra from 496 nm and 773 nm for a W lamp was measured and shown in Figure 4-10. The intensity of light from the W lamp at 600 nm was about 4.6 times stronger than that at 500 nm.

The dispersion element inside the monochromator is a blazed reflection grating, and is shown schematically in Figure 4-11. The grating equation is expressed as [9]:

$$d (\sin\theta_m - \sin\theta_i) = m\lambda \quad (4-1)$$

where d is the groove spacing, θ_m is the diffraction angle at m^{th} order, θ_i is the incident angle and λ is the wavelength. The diffraction angles are dependent on the wavelength

resulting in dispersion of the light. Mirrors increase the path length of the light and therefore the divergence prior to the light reaching the exit slit.

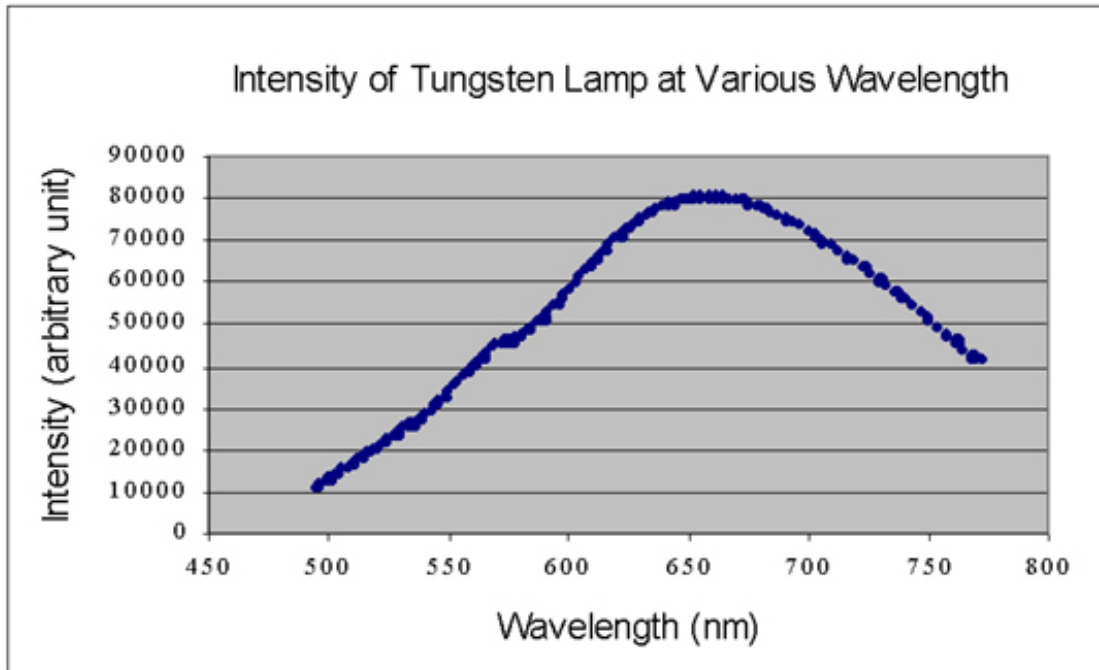


Figure 4-10. The measurement result of intensity versus wavelength for the tungsten lamp used in the optical bench (scan mode). The relative intensity at 600 nm is about 4.6 times higher than at 500 nm.



Figure 4-11. Gratings (a) transmission amplitude grating (b) blazed reflection grating [9].

The wavelength resolution of the monochromator is controlled by the entrance and exit slits. The entrance slit controls the incident beam size which only allows a very small portion of light to enter the monochromator to ensure that the light rays that strike

the grating are parallel. A stepping motor controls the grating rotation and allows a certain portion of the light spectrum to pass through the exit slit. Two filters, a high- and a low-pass filter, are placed in the optical pathway to create a band-pass filter for the wavelength range of interest, which eliminates spurious signals from higher orders of diffraction.

The transmission pathway (part (A) in Figure 4-9) contains a series of mirror and two light detectors (a lead sulfide (PbS) and a silicon (Si) detector) but only the Si detector was used for visible light in this study. The PSF pathway (part (B)) in Figure 4-9) consists of a point source aperture of 100 μm , a 3 mm aperture, and a CCD camera. The point source aperture defines the point source for measurement of the PSF. The 3 mm aperture restricts the measurement to the area of a photon sieve. The CCD camera provides a read-out of intensity versus x and y coordinates for generation of the PSF as described below.

4.4.2 Charge-Coupled Device (CCD) Camera

A CCD is a sensor that consists of grid-like array of coupled capacitors, which can store electric charges after exposure to light. A schematic drawing of a CCD is shown in Figure 4-12 [79]. The electric charge generated on each capacitor, or pixel, is proportional to the light intensity impinging on that location. After capturing an image, the first row of capacitors transfer the amount of charge on each pixel to a readout register, which converts the charges to voltages. The charges are deleted after reading, and the charges from the next row are moved to the readout register. The process is repeated until the charges of the last row of array been read. The voltages from the array form the two dimensional image.

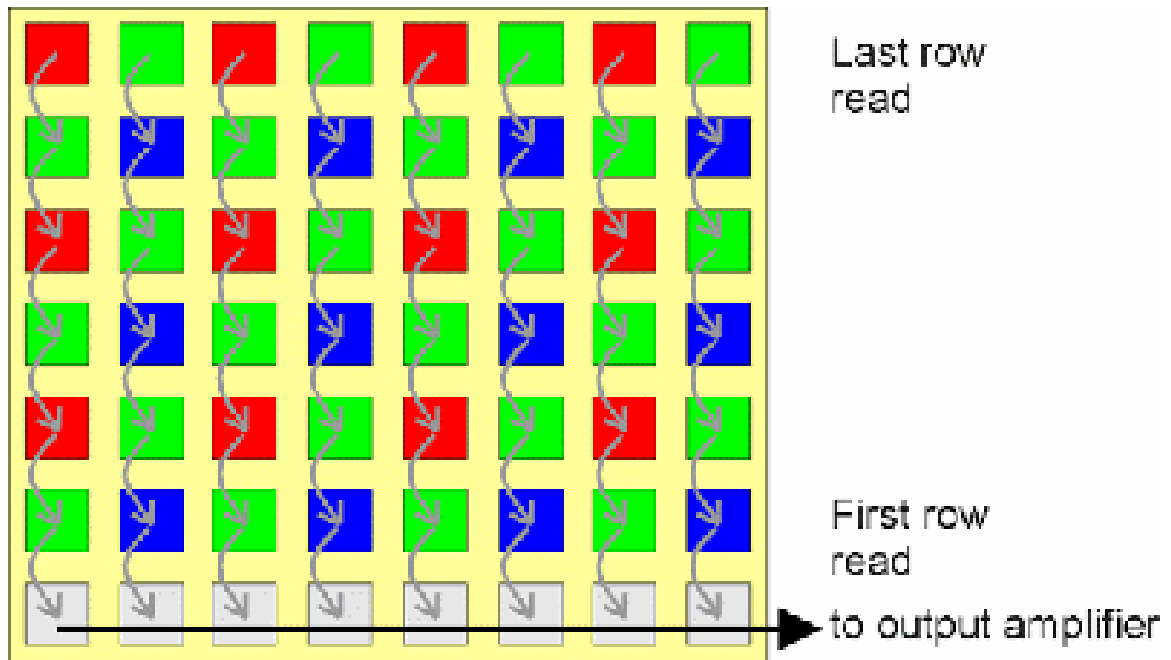


Figure 4-12. An illustration of the CCD read-out mechanism. The white squares are the readout register and are connected to an output amplifier. Charges generated in each row are moved down to the readout register and transformed to voltages for display purposes [79].

The CCD camera used in the experiment is a WinCamD camera with a Sony progressive scan $\frac{1}{2}$ inch CCD that contains 1360 (H) x 1024 (V) $4.65 \mu\text{m}$ square pixels. It also has a 14-bit (16384 level) analog to digital converter (ADC) which provides better resolution for the input signals. The electronic shutter controls the exposure time from 16 to 1048 ms in a 16 ms step. It has two capture modes: full and fast. The full mode gives a pixel size of $4.65 \times 4.65 \mu\text{m}$ while the fast mode gives a larger pixel of $9.3 \times 9.3 \mu\text{m}$ but takes less time to capture images. Only the fast mode ($9.3 \mu\text{m}$ pixel size) was used for the measurement in this research. The CCD inside the WinCamD exhibits a saturation irradiance of 0.15 mW/cm^2 under a monochromatic light with wavelength of 630 nm and exposure time of 25 ms [80]. Saturation of a CCD is the highest possible number of electrons that a pixel can contained and is generally referred to as the “full well” capacity

[81]. Saturation irradiance is the power of incident light per unit area that causes the saturation of a CCD. If the incident intensity is higher than the saturation irradiance, a flat-top (saturated intensity) PSF will form, as shown in Figure 4-13. The damage threshold of the CCD is a few mW/cm^2 . Damage threshold is the highest irradiance that a CCD can tolerate without causing permanent damage [82]. Saturation irradiance and the damage threshold need to be noted in order to prevent artifact or damage, respectively, to the CCD camera. In this research, all the PSFs were measured under the normal condition of the CCD camera without saturation.

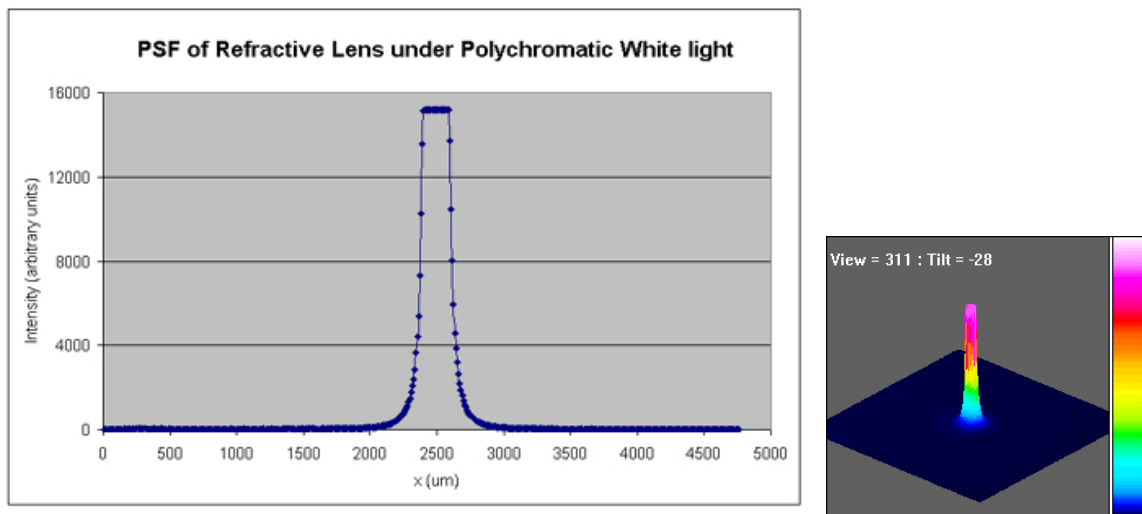


Figure 4-13. Saturated PSF. The flat-top of the PSF indicated the saturation of the CCD camera. The saturated intensity of this 14-bit WinCamD CCD camera was found to be around 15000 (15163 in this example).

A sample screen of a PSF measurement taken by WinCamD CCD camera is shown in Figure 4-14. The two one dimensional (1-D) PSFs shown at the bottom represent the intensity profiles across the focused point along the X and Y axes, which are shown as a 90° crosshair in the image. The image at the right shows the three dimensional (3-D) PSF. The color column at the right side of the 3-D PSF shows the intensity scale from high to low intensity as white, pink, red, yellow, to blue.

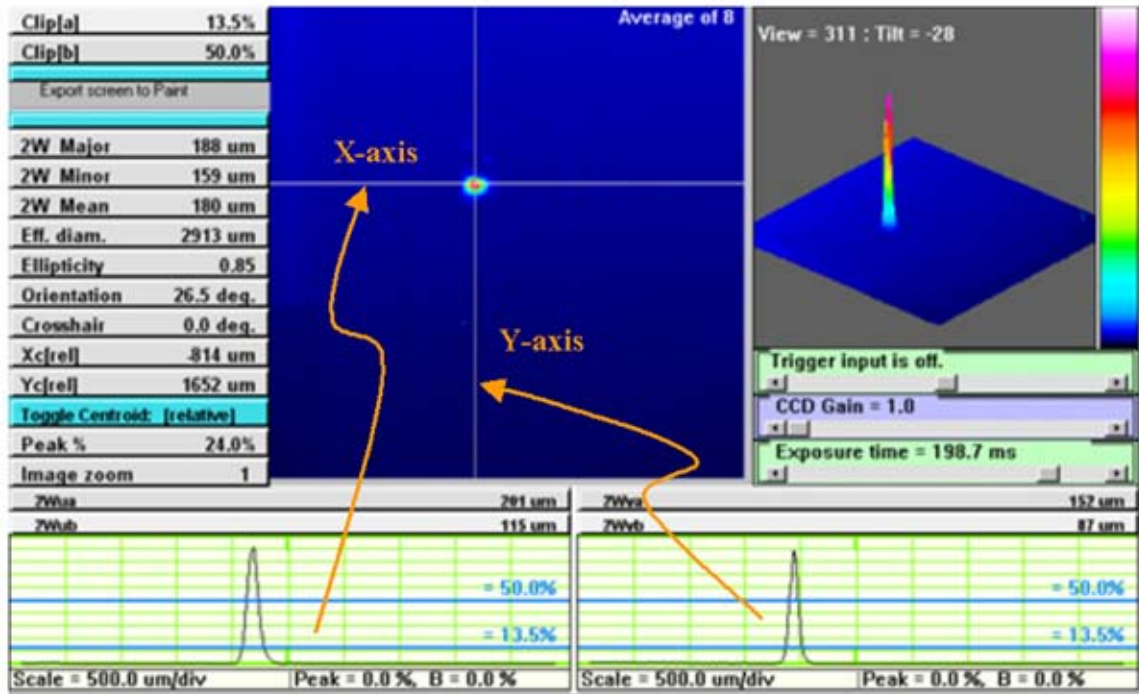


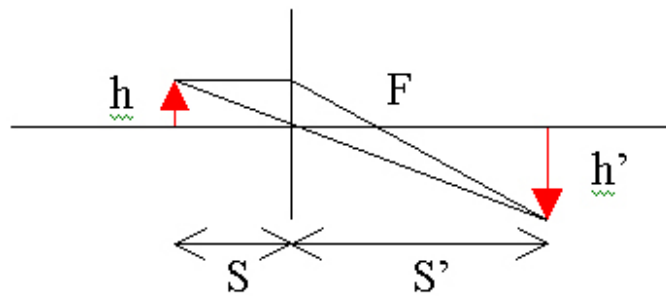
Figure 4-14. A sample of PSF measurement taken by WinCamD CCD camera. The two one dimensional (1-D) PSFs shown at the bottom represent the intensity profiles across the focused spot along the X and Y axes, which are shown as a 90° crosshair in the image.

4.4.3 Focal Length Characterization

As described above, the arrangement shown in part (B) in Figure 4-9 was used to measure the focal length and PSF of photon sieves. Before attaching the photon sieve onto the sample holder, the alignment of the elements was checked by using the 3 mm aperture attached onto a refractive optic lens and focused under white (polychromatic) light from the tungsten lamp. This step ensured that the point source image was captured by the approximately 6 x 4 mm CCD chip. Once the alignment was verified, no transaxial movement (i.e. in the plane of the PS) was allowed for any optical element. The single-wavelength photon sieve, **610** shown in Figure 4-5, was placed on the 3 mm aperture then attached onto the sample holder. The placement of the photon sieve onto

the aperture was carried out under an optical microscope to ensure placement in the center of the aperture and that no pinholes were blocked by the aperture.

Since the lens properties of a single-wavelength photon sieves is wavelength dependent, the light source was changed from the polychromatic white light to the monochromatic 600 nm light for measurement of the focal length. As shown in Figure 4-9 part (B) and the enlarged diagram in Figure 4-15, the distance between the point source aperture and the photon sieve (object distance, S) was fixed while the distance between the photon sieve and the CCD camera (image distance, S') was changed for measurement of the focal length.



$$\text{Magnification} = h'/h = S'/S$$

Figure 4-15. Schematic drawing of the relationship between object distance (S), image distance (S'), and focal length (F). h and h' are the heights of the object and the image, respectively.

The PSF was measured at each S' position, then the peak intensity of each PSF was recorded to identify the best focal point. After finding the image distance S' corresponding to the maximum intensity, the focal length (F) was obtained by the simple equation [9]:

$$1/S + 1/S' = 1/F \quad (4-2)$$

The PS (e.g. **610**) was then retested under both monochromatic 500 nm light and white light to characterize the focusing ability at different wavelengths. The same procedures were repeated for all of the PS patterns (Figure 4-5 and 4-7) in a similar fashion. For example, for lens **510**, the light source was changed from 500 nm to 600 nm and white light accordingly to characterize the focusing ability.

4.4.4 Full Width Half Maximum (FWHM) Characterization

The FWHM of the PSF was measured using three light sources (500 nm, 600 nm, and polychromatic white light). The PSF for each photon sieve under each of the three light spectra were obtained at the characteristic focal length. This tested the image quality (in terms of FWHM and intensity) of each photon sieves when a single detector (CCD camera in this case) was set to the designed, fixed focal plane. This allowed a direct comparison between the single- and dual-wavelength photon sieves.

The PSF from lens **610** tested with monochromatic 600nm light illustrates the principle of obtaining the FWHM, as shown in Figure 4-16.

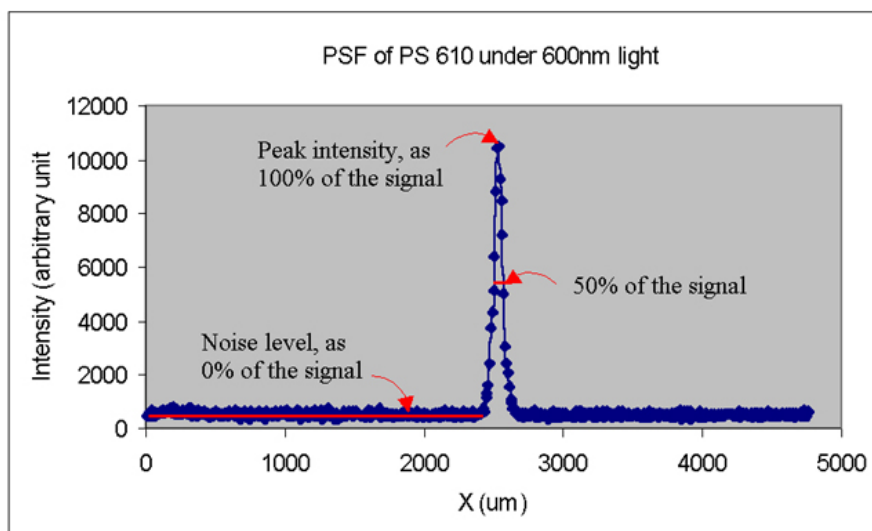


Figure 4-16. A sample PSF (lens **610**) to show the definition of FWHM. The signal is counted from the noise level (0%) to the peak intensity (100%). The FWHM of the PSF was the width across the signal peak at half of its maximum value.

The PSF consisted of an intensity signal and a background noise. The first 200 data points within the noise level were averaged to determine the intensity of noise level and was set to be 0% . The FWHM of the PSF was the width across the signal peak at half of its maximum value corrected for the noise level.

For the FWHM characterization, experiences showed that the peak intensity and the FWHM of a PSF were very sensitive to the optical bench setup and the parameters set in the CCD software, as described below.

The first issue was the magnification effect for the PSFs obtained at different object and image distances. The image obtained with the CCD camera located at the focal plane is the image of the point source with an aperture of 100 μm . As shown by the equation (4-2), a focal length can be obtained by many sets of object and image distances.

However, the size of the image is magnified or reduced dependent on the ratio of S'/S , as shown in Figure 4-15. For example, when two sets of distances (S'/S), 100 mm/100 mm and 106 mm/95 mm, are used to measure a PSF of a photon sieve, the focal length for both cases is 50 mm; however, the FWHMs obtained from the set of 106 mm/95 mm is 12% larger than the one from 100 mm/100 mm (magnification = 1). To minimize random-error, all photon sieves were tested in the same optical setup and finished in one day. The magnification factor of the FWHMs for all the photon sieves was kept constant without any correction. In this research, the trend instead of absolute values of FWHM and intensity was studied. As long as the magnification factor remained constant for all measurements, it is not critical to correct it for the data presented below.

The second issue was the parameters for image capture by the CCD. If the detection system is not saturated, the signal intensity and the noise level should double

when the exposure time is doubled, and the FWHM of the two PSFs remain unchanged. However, the FWHM increased about the size of 1 pixel ($9.3 \mu\text{m}$ in fast-scan mode) when the exposure time was changed from 400 ms to 600 ms. Due to this problem, all the photon sieves were tested with the same exposure time of 800 ms.

The characterization of FWHM was repeated the next day with the same optical bench set up and same exposure time to validate the trend in the experiment results.

For the reference purpose, the PSF measured by using a refractive lens with focal length of 50 mm is shown in Figure 4-17 (measured in different day). The transmission of refractive lenses is much higher than diffractive lenses. To avoid the saturation problem, only 600 nm light was used for PSF measurement and the exposure time was set as 200 ms. The calculated FWHM of this measurement is $70 \mu\text{m}$.

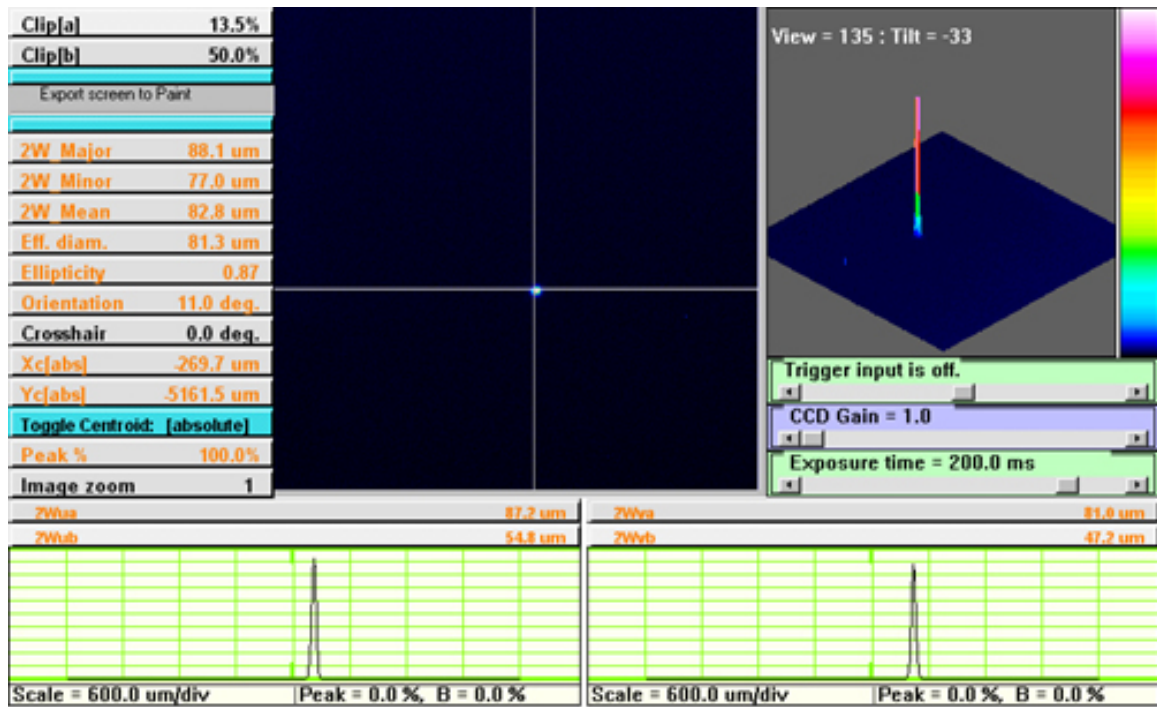


Figure 4-17. PSF of the refractive lens with a focal length of 50 mm measured under 600 nm light with a exposure time of 200 ms.

4.5 Results

4.5.1 Focal Length Characterization

A typical plot of intensity versus CCD detector distance from the PS (lens **510** with monochromatic 500 nm light) is shown in Figure 4-18. As discussed above, the position of maximum intensity was associated with the best focus, which in this case is 106 mm (with the object distance fixed at 101 mm). By applying the simple equation (4-2), the focal length for **510** under 500 nm light is characterized as 51.7 mm, which is 3.4% larger than the designed focal length of 50 mm.

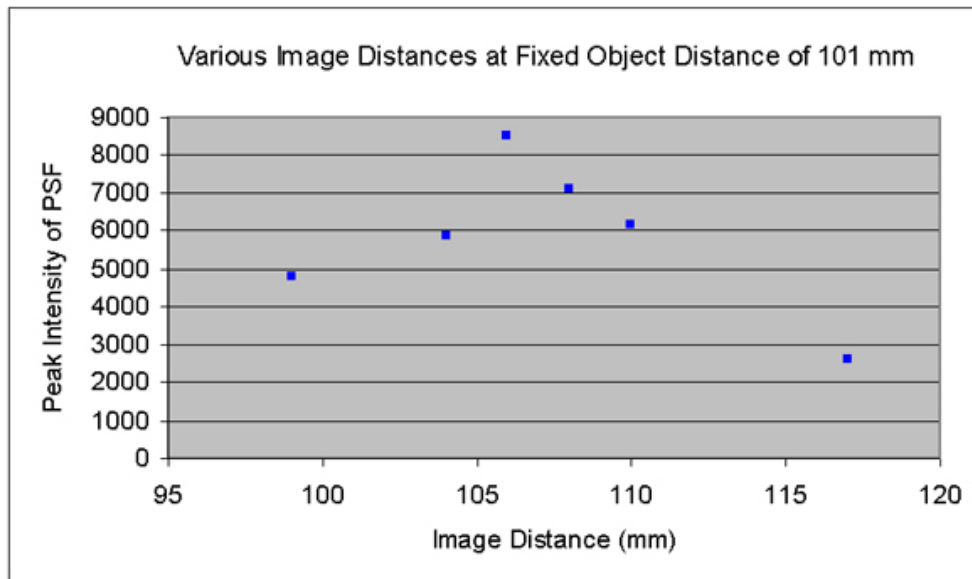


Figure 4-18. Peak intensity of PSFs from **510** with 500 nm light obtained at various image distances. The highest intensity was obtained when the image distance was 106 mm when the object distance was 101 mm, resulting in a focal distance of 51.7 mm.

The focal lengths for the two single-wavelength photon sieves (**510** and **610**) using 500 nm and 600 nm light are summarized in Figure 4-19. When the 600 nm light passed through lens **610** or the 500 nm light passed through lens **510**, the focal length was 51.7mm. The corresponding PSFs are shown in Figure 4-20. When 500 nm light passed

through lens **610** (shown as blue line in Figure 4-19 (a)), the light was focused at a distance greater than 59.5 mm, which is the farthest distance the CCD camera can be moved along the optical axis. When 600 nm light passed through lens **510** (shown as red line in Figure 4-19 (b)), the light was focused with a focal length of 42.4 mm. From the simple Fraunhofer diffraction equation (2-3), the longer the wavelength, the larger the diffraction angle. This is true for all diffraction lenses and can be seen clearly in Figure 4-19. The comparisons between the experiment results and the theoretical values for the diffraction angle and focal length are discussed in section 4-6. The same focal length characteristics were observed for the 3-sector single-wavelength photon sieves, **605** and **505**. The differences between the complete and half (3-sector) photon sieves were the intensity and FWHM of the PSFs.

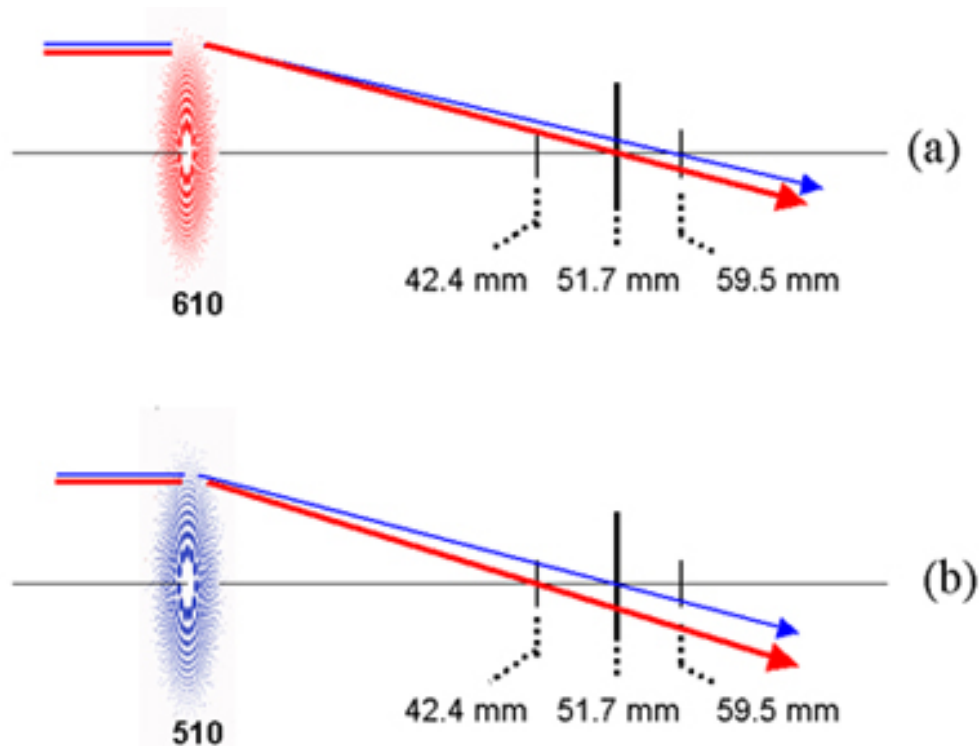


Figure 4-19. Focal length characterization for single-wavelength photon sieves under 500 nm and 600 nm lights. (a) PS **610** (b) PS **510**. The red and blue lines indicated the stronger 600 nm and the weaker 500 nm lights, respectively.

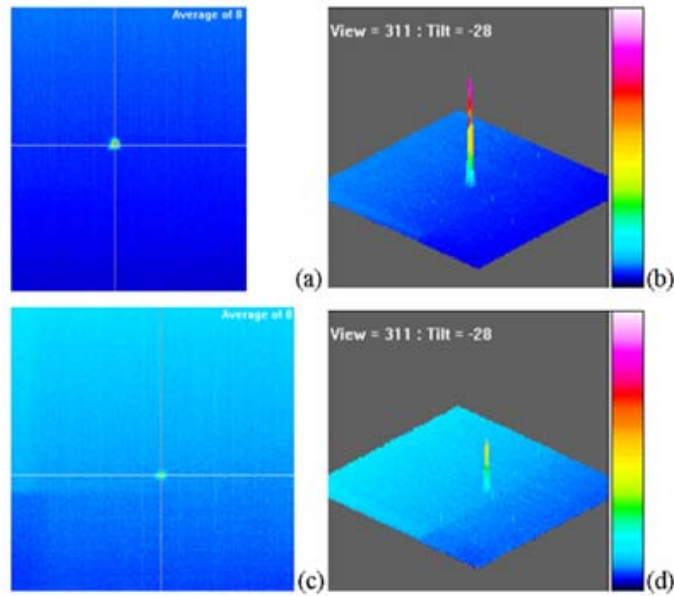


Figure 4-20. PSFs at focal point. (a) top view (b) 3-D tilted view for 600 nm light passed through PS **610**; (c) top view (b) 3-D tilted view for 500 nm light passed through PS **510**. The rainbow column in the 3-D tilted view indicates the magnitude of intensity (red to blue: high to low).

4.5.2 Full Width Half Maximum (FWHM) and Peak Intensity of PSFs

The trend obtained from the repeated measurement of the FWHM versus wavelength and lens designs were identical. A typical set of data are shown below. The CCD camera was always placed at the measured focal length, which is 50.9 mm for these data. Figures 4-21 shows the top view of the PSFs for each photon sieve under 600 nm light source.

In Figure 4-21, no focal spot is detected from single-wavelength photon sieves **505** and **510**. This is because of the pinholes in these two photon sieves were not designed to focus the 600 nm light. From the focal length characterization, when the 600 nm light passed through pinholes designed for 500 nm, it was focused at a focal length of 42.4 mm, which was 9.3 mm in front of the CCD camera. Thus no focused image was observed on the CCD camera.

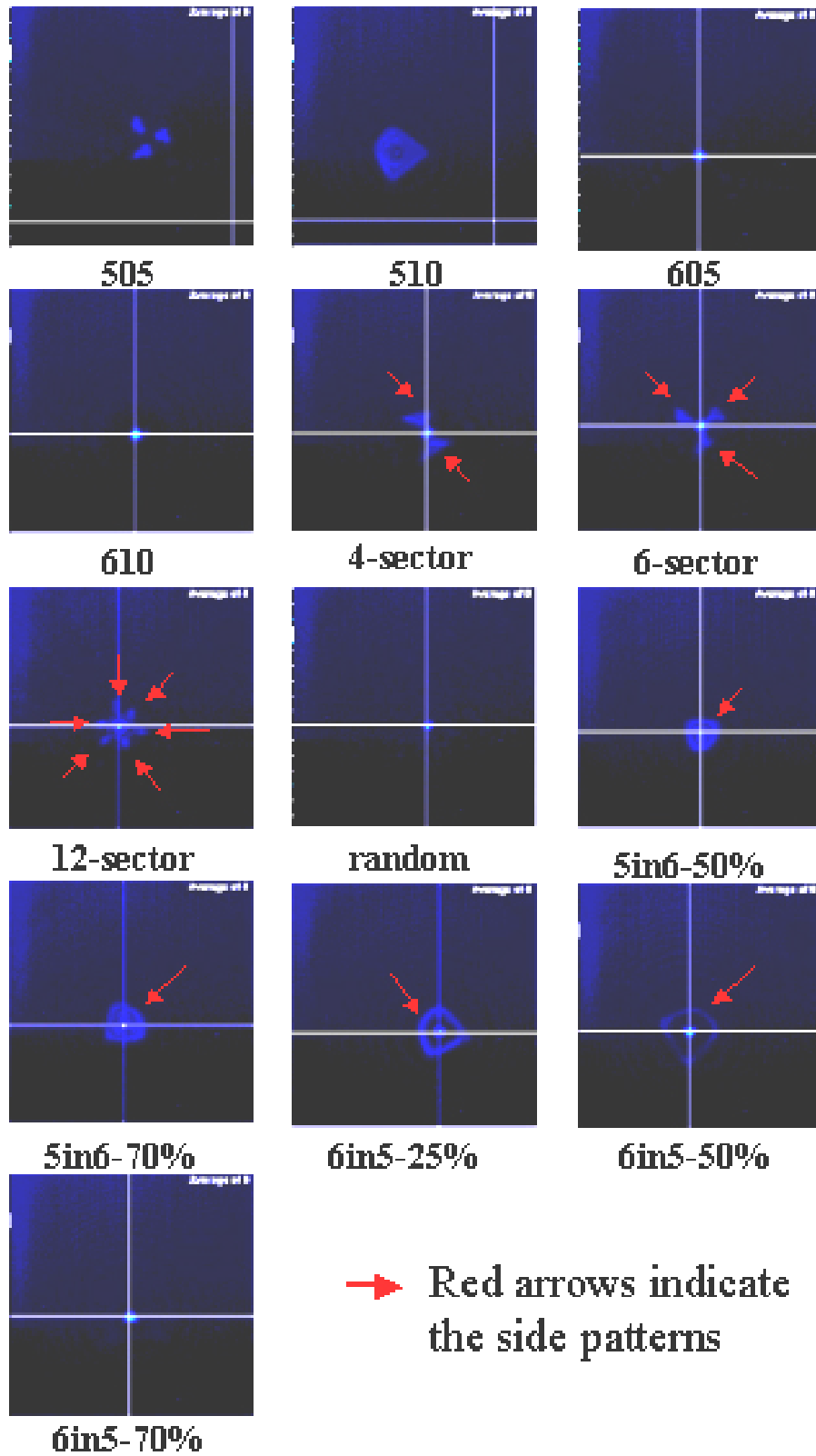


Figure 4-21. Top view of PSF for photon sieves under monochromatic 600 nm light.

In Figure 4-21, the PSFs of PS 605 and PS 610 show clear focal spots and the focal spot of 610 is brighter than that from 605 because of the greater pinhole open area of PS 610. The PSFs of the balance of the dual-wavelength photon sieves show focal spots with different side patterns, which were indicated with red arrows in Figure 4-21. For example, 2-fold, 3-fold, and 6-fold side patterns are found in the PSFs of 4-sector, 6-sector, and 12-sector photon sieves, respectively. For the PSFs of 5in6-50%, 5in6-70%, 6in5-25%, 6in5-50% and 6in5-70%, the side patterns become ring-shape due to the concentric designs of photon sieves. The PSFs for photon sieves under 500 nm light are not shown due to the low intensity of the source at this wavelength (see Figure 4-10).

Figures 4-22 shows the top view of the PSFs for each photon sieve under polychromatic white light source. In Figure 4-22, a focal spot and a bright side pattern was observed for every photon sieve, including all single- and dual-wavelength designs.

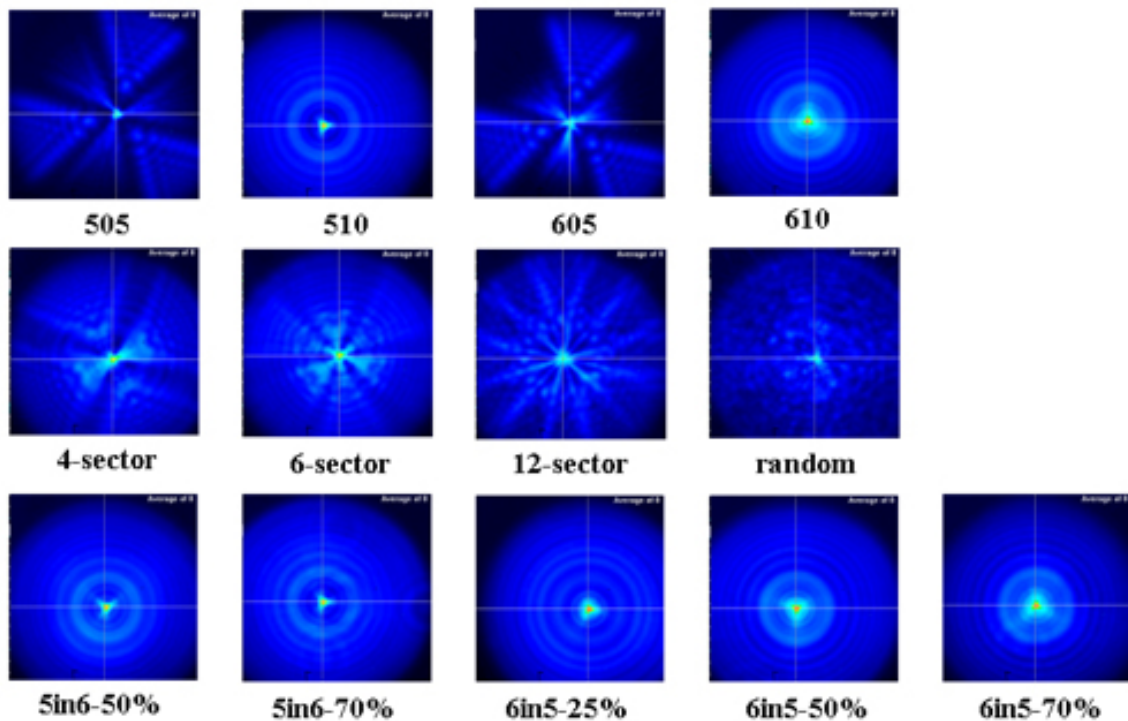


Figure 4-22. Top view of PSF for photon sieves under polychromatic white light.

The side patterns were the bright area outside the focal spots and were dependent on the distribution of pinholes and the design for two wavelengths. The side patterns of **505** and **605** show the design of the photon sieves (3-sector) clearly. In addition, the boundaries of each sector of the sectional designed photon sieves are clearly observed for the **4-sector**, **6-sector**, and **12-sector** lenses. It is difficult to distinguish the side patterns of concentric designed dual-wavelength photon sieves (**5in6-50%**, **5in6-70%**, **6in5-25%**, **6in5-50%** and **6in5-70%**) from the single-wavelength photon sieves (510 and 610), since all the side patterns appear to be similar – a bright focal spot with ring-shape side patterns.

The PSF of each photon sieve measured under 600 nm, 500 nm, and white lights with intensity scales of 7000, 1800, and 14000 are shown in Figure 4-23, 4-24, and 4-25, respectively.

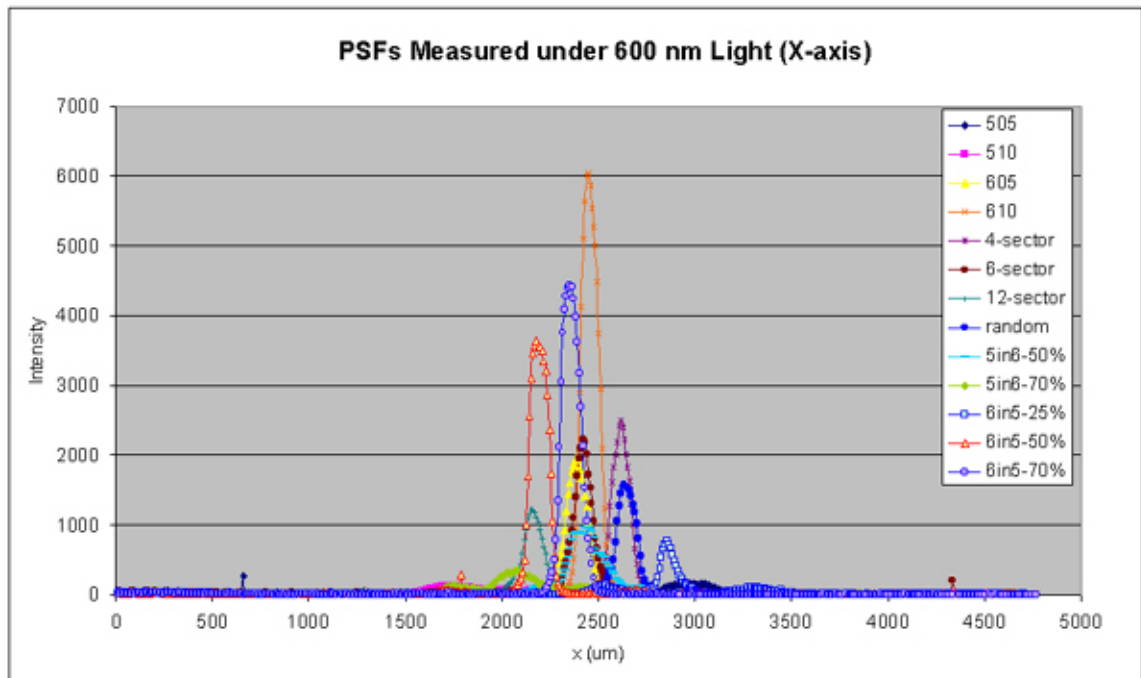


Figure 4-23 PSFs under 600 nm light for all 13 photon sieves.

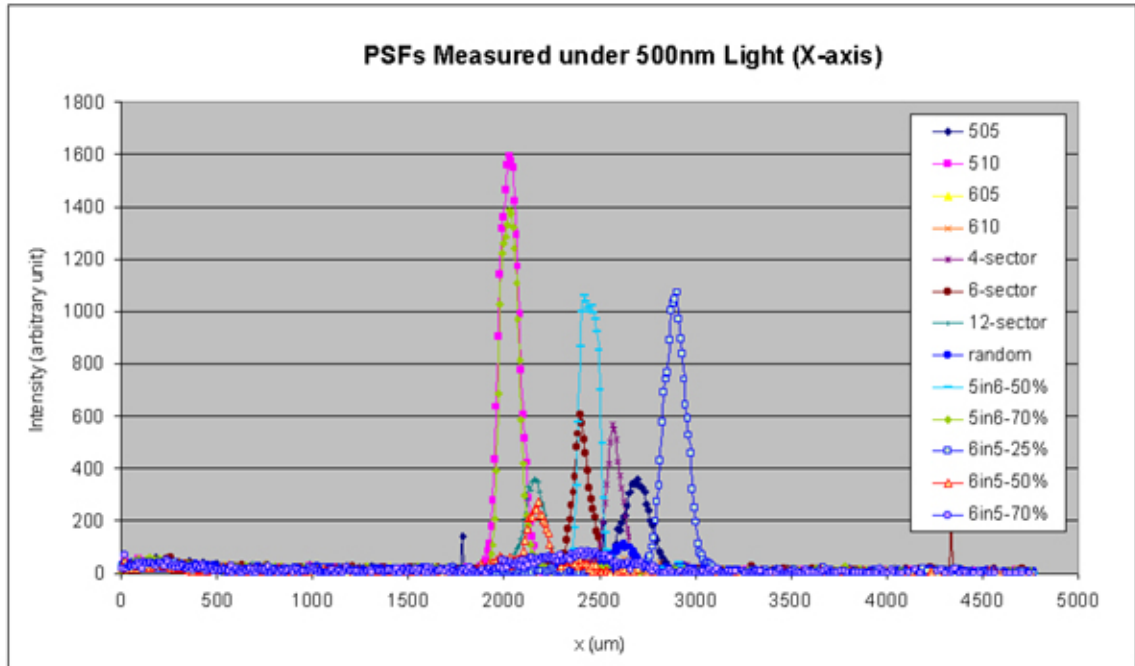


Figure 4-24 PSFs under 500 nm light for all 13 photon sieves.

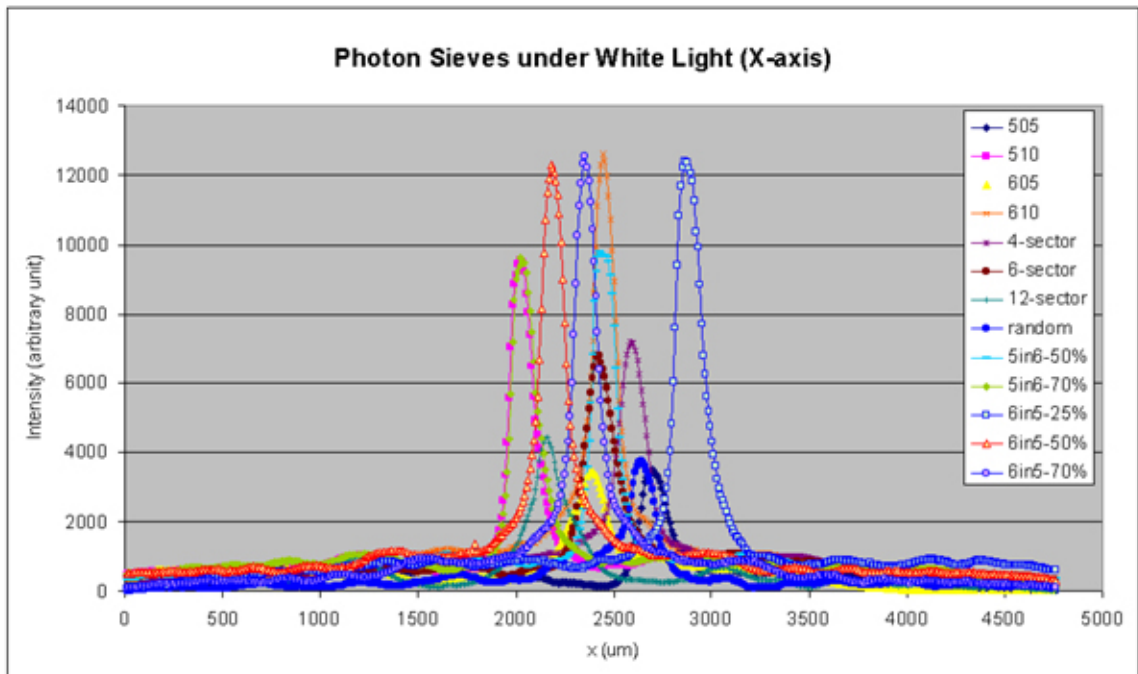


Figure 4-25 PSFs under white light for all 13 photon sieves.

Only the PSFs along the X-axis are shown and the intensities are on a relative scale, which means that an intensity count of 14000 is two times brighter than 7000. PS **610** has the highest signal intensity under 600 nm light (Figure 4-23) while PS **510** has the highest signal intensity under 500 nm light (Figure 4-24). When tested under white light, **610**, **6in5-70%**, **6in5-50%**, and **6in5-25%** have almost equal highest intensities, as shown in Figure 4-25. In addition, the background noise found in Figure 4-25 (polychromatic white light) is much higher (~1000 in relative intensity) than the noise in Figures 4-23 (monochromatic 600 nm light, ~ 100 in relative intensity) and Figure 4-24 (monochromatic 500 nm light, ~ several tens in relative intensity). The FWHMs and peak intensities of each PSF in both X and Y-axes measured with each of the three light spectra were calculated and are summarized in Table 4-3.

The FWHMs and intensities from Table 4-3 for all photon sieves under 600 nm, 500 nm, and white light are plotted in Figures 4-26, 4-27, and 4-28, respectively. The FWHMs in X- and Y-axes ($\text{FWHM}|_x$ and $\text{FWHM}|_y$, respectively), the average (Ave), and the $(X \times Y)/\text{Ave}$ are shown in the figures (see legend of the figure). The average (Ave) is equal to $(\text{FWHM}|_x + \text{FWHM}|_y)/2$ while $(X \times Y)/\text{Ave}$ is equal to $(\text{FWHM}|_x \times \text{FWHM}|_y)/\text{Ave}$. The error bar for all points are in the range of $\pm 10 \mu\text{m}$, which is nearly twice the single pixel size (fast mode, pixel size is $9.3 \mu\text{m}$) in WinCamD CCD camera. The PS with cross mark indicates a focal spot was not detected for that PS under the measurement condition. This condition can be seen in photon sieves **505** and **510** in Figure 4-26 and **605**, **610**, and **6in5-70%** in Figure 4-27. An intensity curve corrected with the open hole area scale (pink dash line with white dots) for all the PSs under white light is shown in Figure 4-28.

Table 4-3. FWHM and peak intensity at X- and Y-axes for each PSF measured with each of the three light spectra – 500 nm, 600 nm, and white lights. “N/A” means that no focused image was formed with the photon sieve under the specific light spectrum.

Light Source (nm)	PS type	FWHM (μm)			Peak Intensity		
		X-axis	Y-axis	Ave	X-axis	Y-axis	Ave
500	505	154	122	138	358	356	357
500	510	123	80	102	1596	1600	1598
500	605	N/A	N/A	N/A	N/A	N/A	N/A
500	610	N/A	N/A	N/A	N/A	N/A	N/A
500	4-sector	87	104	96	568	652	610
500	6-sector	87	97	92	603	589	596
500	12-sector	117	98	108	358	299	328.5
500	random	133	77	105	98	120	109
500	5in6-50%	129	95	112	1057	1057	1057
500	5in6-70%	116	82	99	1386	1401	1394
500	6in5-25%	140	89	115	1071	1047	1059
500	6in5-50%	119	162	141	272	286	279
500	6in5-70%	N/A	N/A	N/A	N/A	N/A	N/A
600	505	N/A	N/A	N/A	N/A	N/A	N/A
600	510	N/A	N/A	N/A	N/A	N/A	N/A
600	605	122	112	117	1943	1875	1909
600	610	109	93	101	6058	6058	6058
600	4-sector	113	88	101	2502	2502	2502
600	6-sector	99	103	101	2218	2218	2218
600	12-sector	116	123	120	1230	1230	1230
600	random	120	92	106	1591	1591	1591
600	5in6-50%	189	138	164	1038	1038	1038
600	5in6-70%	213	123	168	363	391	377
600	6in5-25%	85	82	84	772	978	875
600	6in5-50%	118	97	108	3631	3631	3631
600	6in5-70%	118	84	101	4437	4437	4437
White	505	176	165	171	3526	3526	3526
White	510	149	119	134	9547	9547	9547
White	605	226	263	245	3492	3432	3462
White	610	141	127	134	12604	12604	12604
White	4-sector	180	157	169	7183	7183	7183
White	6-sector	191	199	195	6807	6783	6795
White	12-sector	211	180	196	4454	4301	4378
White	random	161	126	144	3763	3763	3763
White	5in6-50%	149	141	145	9766	9766	9766
White	5in6-70%	155	128	142	9597	9597	9597
White	6in5-25%	158	132	145	12409	12409	12409
White	6in5-50%	148	142	145	12295	12295	12295
White	6in5-70%	139	124	132	12547	12547	12547

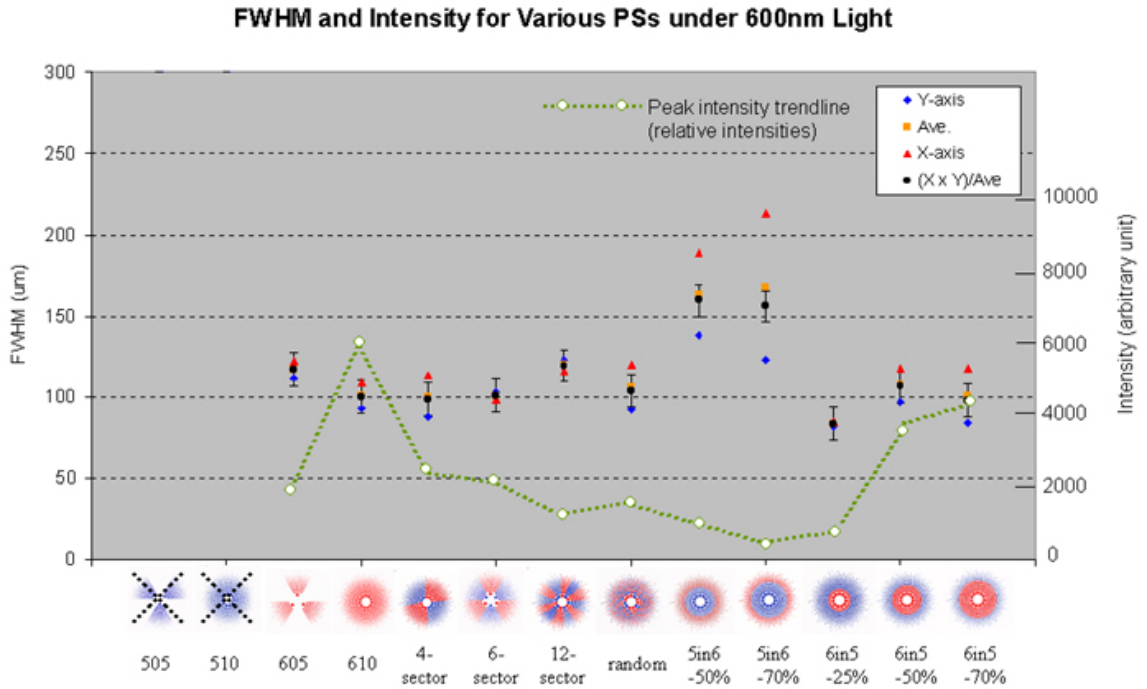


Figure 4-26. FWHM and maximum intensity for photon sieves under 600 nm light. FWHM is the left vertical axis and relative intensity is the right vertical axis. The peak intensity trend line is shown as a green dash line with white dots.

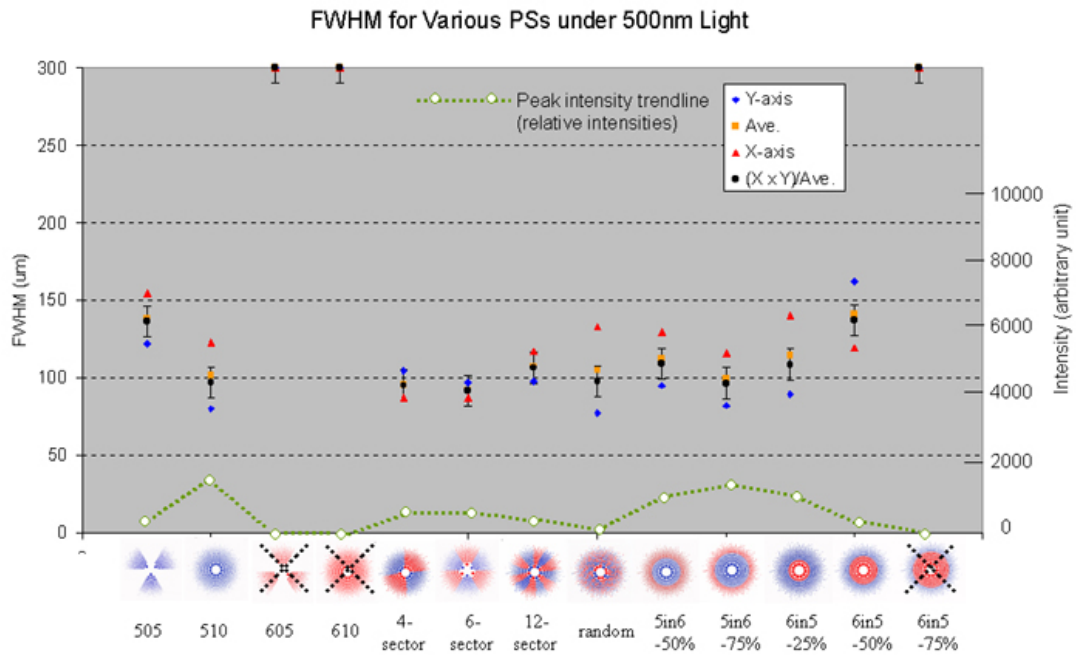


Figure 4-27. FWHM and maximum intensity for photon sieves under 500 nm light. FWHM is the left vertical axis and relative intensity is the right vertical axis. The peak intensity trend line is shown as a green dash line with white dots.

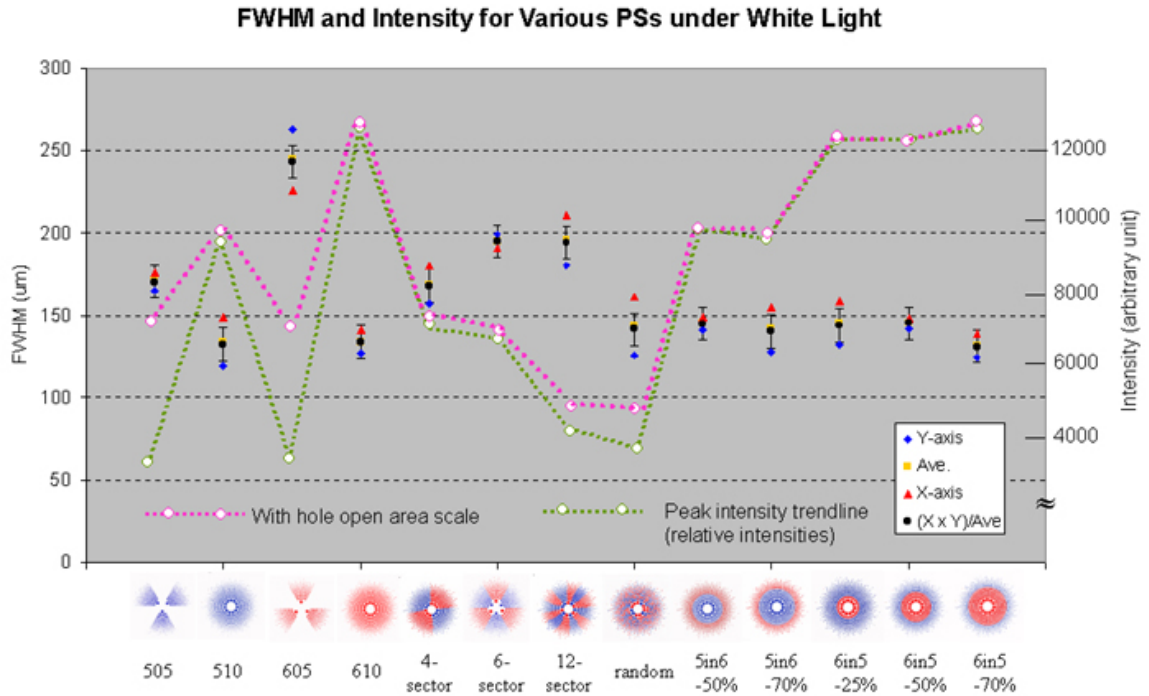


Figure 4-28. FWHM and maximum intensity for photon sieves under white light. FWHM is the left vertical axis and relative intensity is the right vertical axis. The measured and corrected (by open hole area) peak intensity trend lines are shown as a green and pink dash line with white dots, respectively.

Sometimes the focused image of the point source aperture was not round (see Figure 4-29). If only the data in one axis is taken into account, the result may not reflect the real trend in the performance of photon sieves. The separation between the average and $(X \times Y)/Ave$ indicates the difference of the FWHMs obtained from X- and Y-axes. If the focal spot is close to a circle, the FWHM along the X-axis will be close to the one along the Y-axis and the $(X \times Y)/Ave$ data points will fall close to the average data points, as shown in Figure 4-29 (a). On the other hand, if the focal spot is not in a round shape, the FWHM in X- and Y-axes will be very different and the $(X \times Y)/Ave$ data points will be farther from the Ave data points, as shown in Figure 4-29 (b).

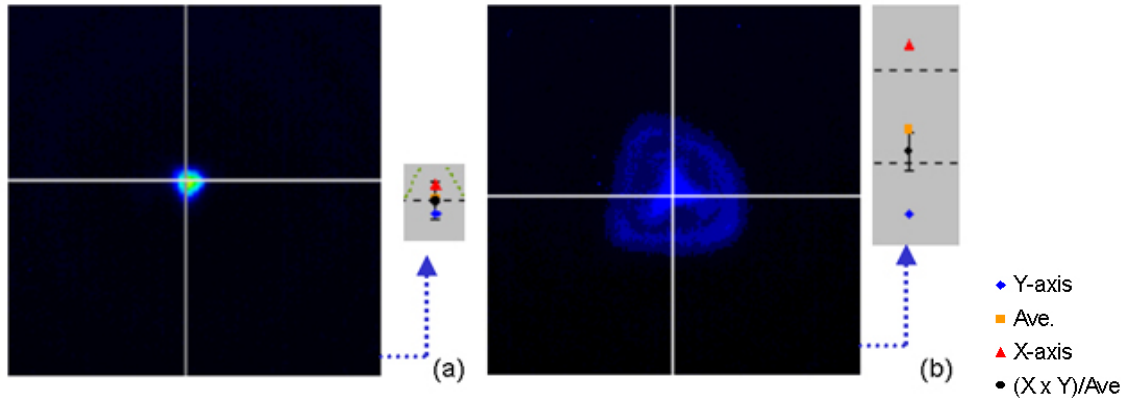


Figure 4-29. Shape of focal spots. (a) focal spot is close to round shape (b) focal spot is not round shape.

4.6 Discussions

From the focal length data, the change of focal length is close to 10 mm (20% of nominal focal length) when switching the monochromatic light source from 500 nm to 600 nm or vice versa for a 3 mm single-wavelength PS with the nominal focal length of 50 mm. This result indicates that for a dual-wavelength photon sieve tested with a polychromatic light source that contained both 500 nm and 600 nm wavelengths would form only the designed wavelength at the 51.7 mm focal plane. The lens properties of diffractive lenses are known to be wavelength dependent. For example, for a pinhole located at the edge of a 500 nm designed FZP (1.5 mm in radius) with a nominal focal length of 50 mm under 500 nm light, the diffraction angle is 1.72° . The theoretical calculation of diffraction angle (Equation 2-3) will change to 2.06° and the focal length (Equation 2-13) will shift to 41.7 mm when the incident wavelength is changed to 600 nm. From the experiment data, the diffraction angle changed from 1.66° to 2.03° and the focal length shifted from 51.7 mm to 42.4 mm when the incident wavelength changed from 500 nm to 600 nm. This comparison indicates that the measured results are consistent with the theoretical calculations. The very large focal length difference

resulted in a large chromatic aberration. From the result of focal length characterization, the longitudinal chromatic aberration was 9.3 mm for 100 nm wavelength differences.

The measured focal length, 51.7 mm, was slightly different from the designed focal length, 50 mm, by a 3% variation. This variation may come from two sources, different wavefront shapes and substrate refraction, as described below. First, in the simulation, the wavefront of incident light was assumed to be planar. However, the wavefront of the incident light in the optical bench was slightly spherical (from a point source with finite distance) with a half angle about 1° of the maximum cone of light picked up by a photon sieve. Second, the refraction of glass substrate was ignored in the simulation; however, the glass substrate was about 1 mm thick with a refractive index of 1.5 in the real sample. The diffracted light may not focus on the designed focus point after being refracted by the glass substrate. It is possible that the 3% variation in the focal length measurement is caused either by the slightly different wavefront shapes or by the inconsistency of substrate refraction between simulation and measurement.

The focal length characterization also helped to understand the formation of image patterns for the photon sieves. For instance, plotting the characteristic light rays of 600 nm light passed through the 500 nm and 600 nm designed pinholes for dual-wavelength photon sieves **6in5-50%** (Figure 4-30 (a)), a ring pattern around the focal spot is formed which matches the image observed during the testing. For PS **6in5-70%**, since the ratio of 500 nm designed pinholes is small (25%), the intensity of this portion of light rays is weak, thus the ring pattern becomes faint and not visible in the image observed during the testing, as shown in Figure 4-30 (b).

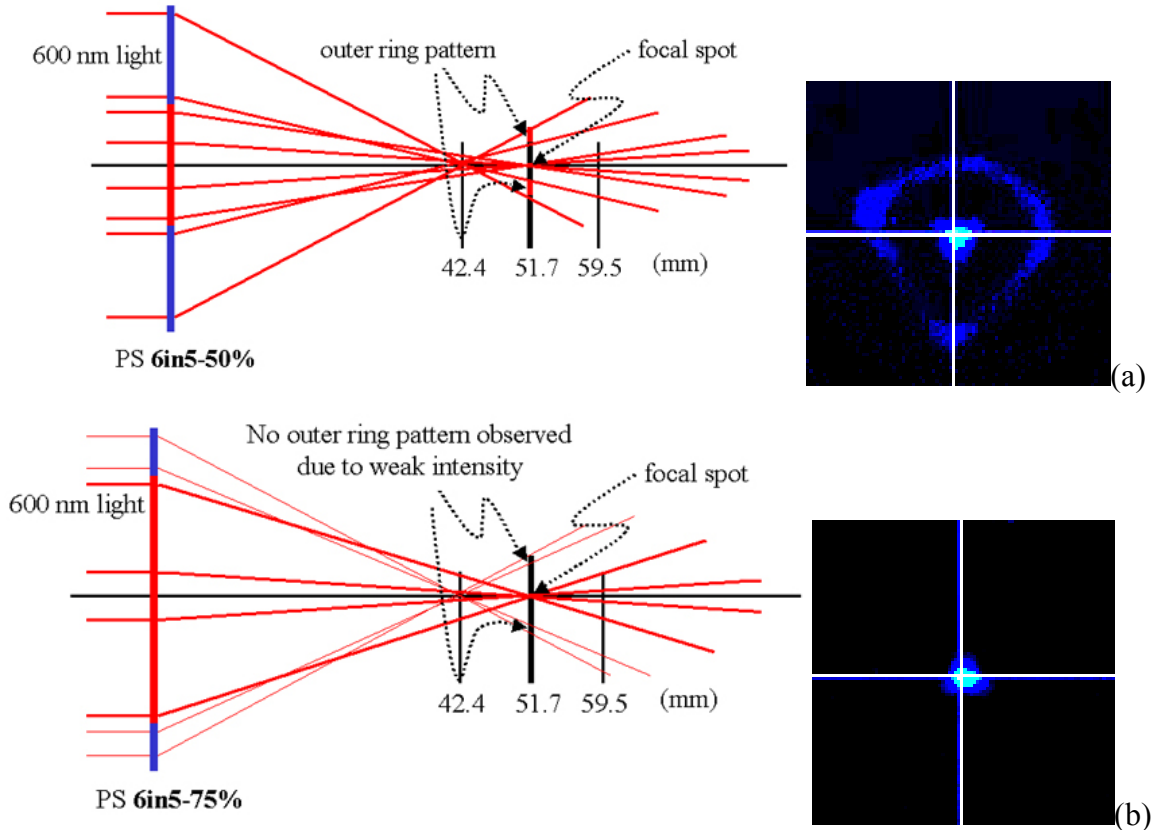


Figure 4-30. Characteristic light rays of 600 nm light passed through (a) **6in5-50%** and (b) **6in5-75%** and explained the formation of ring pattern observed in the images. Thin lines represent weak intensity. Red and blue sections in PS represent the pinholes designed to focus 600 nm and 500 nm light, respectively.

When plotting the same characteristic light rays for PS **5in6-50%**, as shown in Figure 4-31, a smaller ring pattern is formed and matches the image observed for that photon sieve. For PS **5in6-50%**, the pinholes designed for 500 nm are located at the center of the PS. The geometric relation of the undesigned pinholes (designed for 500 nm) makes the unfocused 600 nm light form a smaller ring pattern when comparing to the PS with 500 nm designed pinholes located at the outer area (i.e., **6in5-50%**, Figure 4-30 (a)). The same analyzing technique can be applied to all the photon sieves and explains the PS images obtained for 600 nm monochromatic light shown in Figure 4-21.

From the examples in Figures 4-30 and 4-31, the side patterns (ring shape), were mainly caused by the 600 nm light passed through the 500 nm designed pinholes and focused at the different focal spot as described in above.

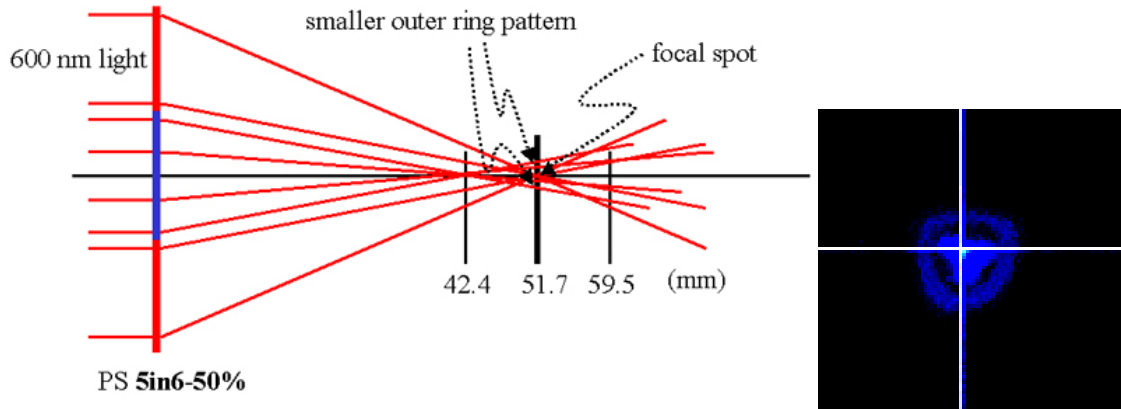


Figure 4-31. Characteristic light rays of 600 nm light passed through PS **5in6-50%** and formed a smaller ring pattern compared to the photon sieves with 600 nm designed pinholes at the central zone.

For the images in Figure 4-22 from all PS designs with white light, the rule is similar but more complicated since the light source is polychromatic and the light intensity is much stronger than the monochromatic light. When white light passed through the PS **610**, the stronger light rays (red lines, 600 nm in wavelength) were focused at the focal plane (51.7 mm, Figure 4-32 (a)). However, when white light passed through the PS **510**, the stronger light rays were focused at a spot in front of the focal plane (42.4 mm) and the weak light rays (blue lines, 500 nm in wavelength) were focused at the CCD detector plane which resulted in a less bright focal spot, as shown in Figure 4-32 (b).

Though this analysis gives a simple prediction of the image formation, it did not explain all the sources that caused the high background noise and side patterns of the images.

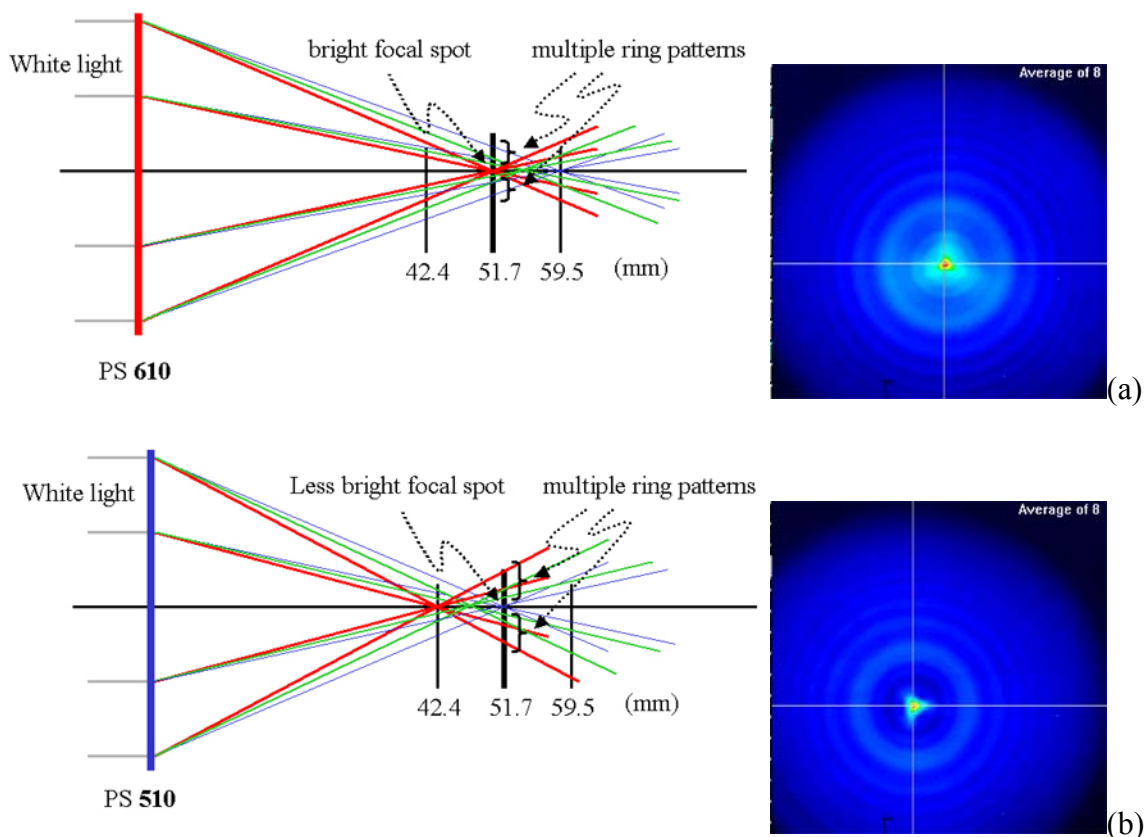


Figure 4-32. Characteristic light rays of polychromatic white light which have passed through a PS lens of (a) **610** and (b) **510**. Red and blue lines represent light rays with intense 600 nm and weakened intensity 500 nm wavelengths, respectively. Green lines represent the light rays with wavelength in-between 600 and 500 nm. The peak intensity obtained from **610** is higher (red center, 12604 in intensity) than the one obtained from **510** (yellow center, 9547 in intensity).

The undiffracted light (zeroth-order intensity) for the pinholes located far from the optical axis were projected on the focal plane instead of focused at the focal point (see Chapter 2) which contributed to the high background noise. In addition, the light rays from higher order diffraction do not focus at the focal spot which also give rise to high background noise. A more realistic plot of the characteristic light rays is shown in the Figure 4-33. The image background noise shown in the Figure 4-22 consists of light from undiffracted light rays, higher orders of diffraction, and light rays passing through

PS pinholes which were not designed for that specific wavelength. The contribution of each source to background noise is not quantified in this research. However, from the results shown in Figure 4-21, if the intensity of light source is low (monochromatic 600 nm), the effect of undiffracted light rays and higher order diffraction is weak since the background intensity is low (~ 100 in relative intensity).

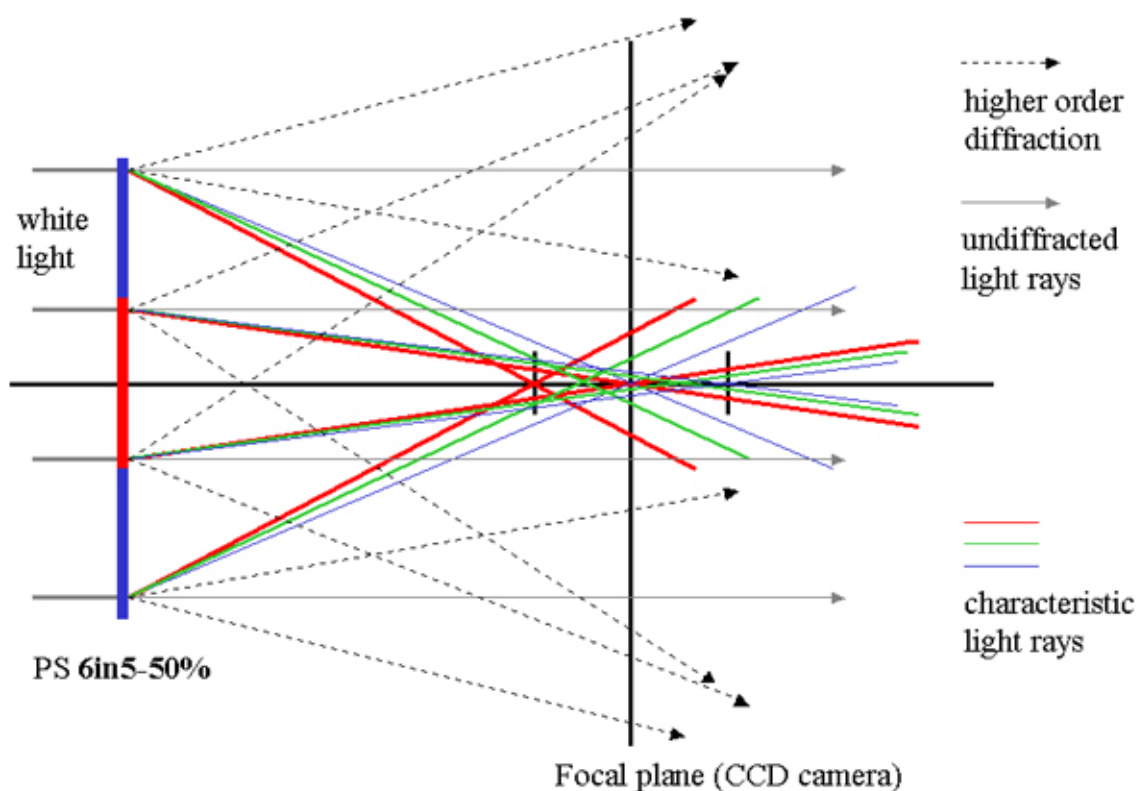


Figure 4-33. Realistic sketch of the image formation for a dual-wavelength photon sieve with white light illumination. Undiffracted light rays, the higher orders of diffraction, and the light rays passed through the pinholes, which were not designed for that specific wavelength are the sources of high background noise of the image.

From data in Figures 4-26 to 4-28, in general, larger FWHMs correspond to lower focal spot intensities. This is because the source light intensity is spread out over a large area at the focal spot. In Figure 4-26, the average FWHMs of most of the photon sieves illuminated by 600 nm light are $\sim 100 \mu\text{m}$, except for **5in6-50%** and **5in6-70%** which are

~150 μm . PS **505** and PS **510** did not focus 600 nm light at all. This indicates that the focusing ability and image quality of most of the photon sieves is very similar at the design wavelength. However, the highest intensity is observed for PS **610** which makes it the better diffractive lens under 600 nm light.

In Figure 4-27, the average FWHMs of most of the photon sieves illuminated by 500 nm light are again ~100 μm except for PS **505** and PS **6in5-50%** which are ~140 μm (PSs **605**, **610**, and **6in5-75%** did not focus 500 nm light). The highest intensity has been observed for PS **510** which makes it the better diffractive lens under 500 nm light.

From the data shown in Figures 4-26 and 4-27, a couple of conclusions can be drawn. The first conclusion is that the pinholes located at the center zone of the concentric dual-wavelength PSs dominate the performance of these photon sieves. Figure 4-34 shows a comparison of the FWHMs and focal spot intensities of PSs **6in5-50%** and **5in6-50%** under 500 nm and 600 nm illumination. Both photon sieves have equal open area for 500 nm and 600 nm designed pinholes. When illuminating the photon sieves with 600 nm light, a smaller FWHM and higher intensity were obtained from the PS with the 600 nm designed pinholes located in the center zone (**6in5-50%**) versus PS **5in6-50%**. For 500 nm illumination, smaller FWHM and higher intensity were obtained from the PS **5in6-50%** (500 nm designed pinholes in the center). Since the central zone is close to the optical axis, the light rays that are diffracted and focused by the pinholes closer to the center are mainly from low order diffraction, which exhibit stronger intensity than the higher order diffraction (see Chapter 2 Literature Review). The light rays diffracted and focused by the pinholes located far from the optical axis are from higher order diffraction, which contribute lower intensity to the focal point intensity

(equations 2-3 to 2-5). Thus the pinholes located in the central zone dominate the performance of photon sieves.

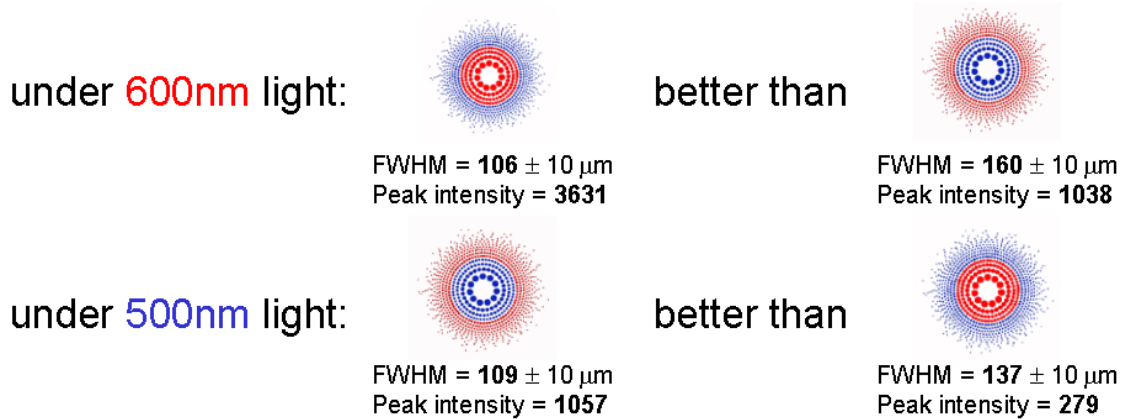


Figure 4-34. Comparison of FWHMs and intensities between **6in5-50%** (red center PS) and **5in6-50%** (blue center PS) under 500 nm and 600 nm light sources. The pinholes located in the central zone dominate the performance of the photon sieves.

The second, under monochromatic light, the intensity of a single-wavelength photon sieve is better than the dual-wavelength photon sieves, while the FWHMs are similar. However, the single-wavelength photon sieves do not function at wavelengths 100 nm from the design wavelength. Due to the existence of the two diffraction elements, the dual-wavelength photon sieves are capable of focusing two wavelengths of light but at lower intensity (transmission), as shown in Figure 4-35.

In Figure 4-28, the result showed that the concentric dual-wavelength PSs had the same FWHMs and intensities as the single-wavelength PSs under polychromatic white light. However, the sector designed photon sieves (**505**, **605**, **4-sector**, **6-sector**, and **12-sector**) exhibit larger FWHMs and lower intensities as compared to the single-wavelength or concentric dual-wavelength designed photon sieves. It is not clear why the sectional designed dual-wavelength PS have worse performance.

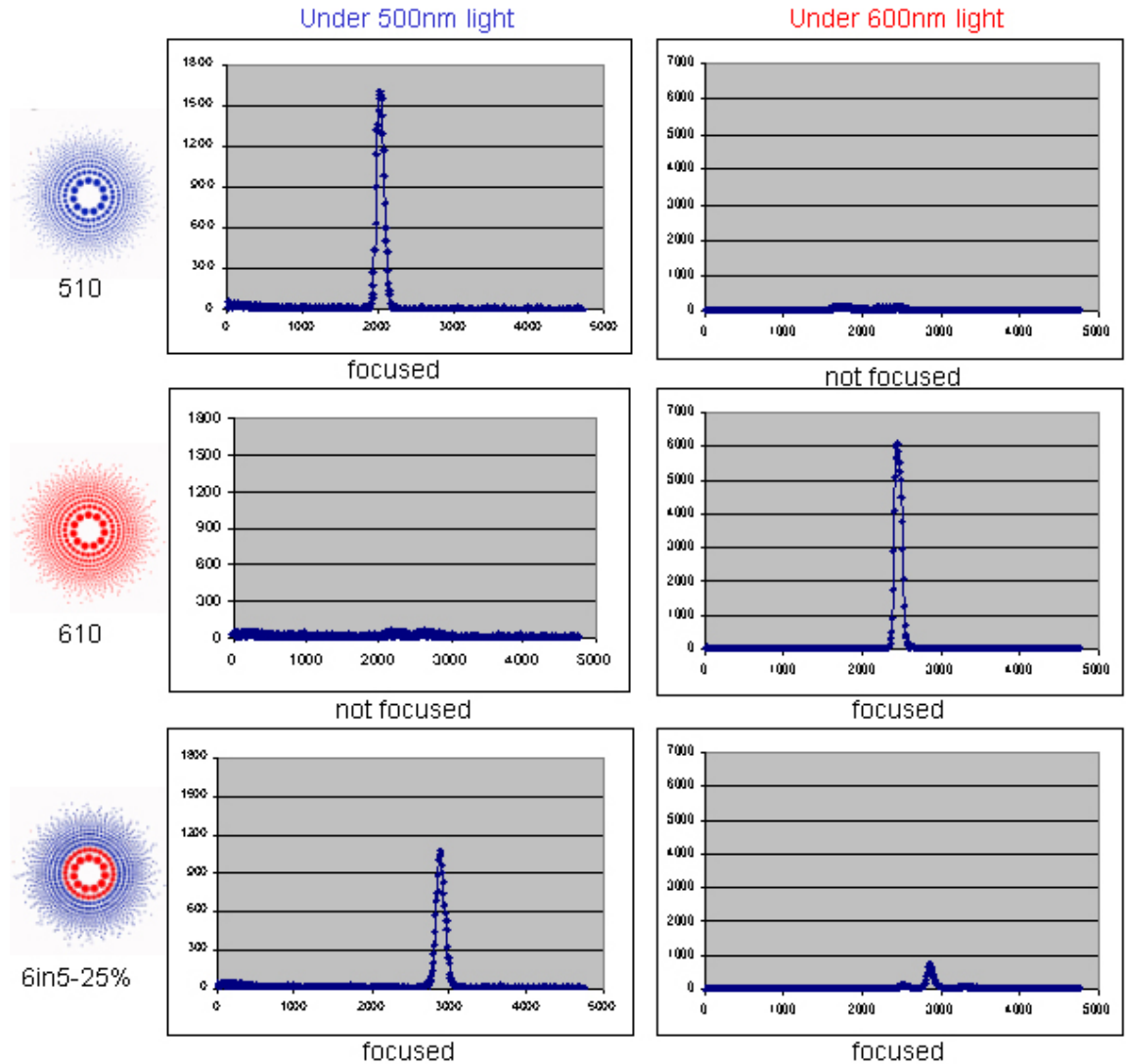


Figure 4-35. The performance of photon sieves when switching the light sources from 500 nm to 600 nm. X-axis is position in μm and Y-axis is relative intensity in arbitrary units. The intensity scales are 1800 and 7000 under 500 nm and 600 nm light, respectively. Single-wavelength PSs, **510** and **610**, cannot focus the light other than the designed wavelength. Dual-wavelength PS, **6in5-25%**, can focus two light sources simultaneously (focal spots were found in both images) but with limited performance.

From the literature review (Chapter 2), the resolution of a photon sieve is controlled by the K factor and the diameter of the pinholes located at the outermost zone. The smallest pinholes for the PS designs in this research have $\sim 10 \mu\text{m}$ in diameter with a K factor of 1.2 which implies that the resolution of the PSs is $\sim 10 \mu\text{m}$. However, this

resolution effect was not observed in this research. A possible reason is that the PSF measured by the CCD camera is essentially an image of the point source. Since the point source aperture in the optical bench is 100 μm in diameter with a finite distance, the FWHM of the PSF measured by the CCD camera will be $\sim 100 \mu\text{m}$. In addition, the pixel size of the CCD used in this research is 9.3 μm , which is close to the theoretical resolution of the PS. Thus the FWHMs obtained in this research are indications of the image quality of the point source rather than the resolution of the photon sieves.

The overall result shows that a single-wavelength PS would be a good focusing filter for polychromatic light since it only focuses the designed wavelength and disperses the rest of the wavelengths. The result also indicates that the dual-wavelength PS exhibits lower intensity but equal FWHM to the single-wavelength PS under monochromatic and polychromatic light sources. The dual-wavelength PS is able to focus the image with reduced intensity when switching between different light sources. Dual-wavelength PSs can be used for the imaging device that requires filtering of polychromatic light at two wavelengths at the cost of intensity.

4.7 Conclusions

Single- and dual-wavelength photon sieves (PSs) were designed and tested in this research project. Based on simulations of the PS properties, the lens diameter was fixed at 3 mm, designed focal length was 50 mm, K factor (d/w ratio) was set to be 1.2, and all the photon sieves were apodized by a modified Gaussian function. PS sieves were fabricated having hole sizes and spacing appropriate to focus either 500 or 600 nm light, and dual-wavelength PS were created by mixing the holes for each wavelength in a

sector, concentric or random pattern. The PS sieves were tested in a modified Perkin-Elmer 16U grating spectrometer with a WinCamD CCD camera.

The PSs were tested for focal length, FWHM and maximum intensity of the image of a 100 μm point source either monochromatic 500 or 600 nm light, or polychromatic white light from a tungsten halogen lamp. The focal length data show that a clear focal spot was formed with a focal length of 51.7 ± 1 mm when monochromatic 500 or 600 nm light passed through the PSs with pinholes designed for 500 nm or 600 nm, respectively. The measured focal length has a 3% variation of the designed focal length (50 mm). This variation may be caused either by the slightly different wavefront shapes (planar versus spherical) or by the inconsistency of the substrate refraction between simulation and measurement. When 600 nm light passed through the PS with pinholes designed for 500 nm, the best image of the point source was formed at a focal length of 42.4 ± 1 mm. For 500 nm light through PS with pinholes designed for 600 nm, the focal length was greater than 59.5 mm. From the result of focal length characterization, the longitudinal chromatic aberration was 9.3 mm for 100 nm wavelength differences, resulting in defocused images of the point source at a focal plane of 51.7 mm. The experiment data is consistent with the theoretical calculation for the focal length shifting.

When the CCD camera was placed at the measured focal length of 51.7 mm, a 2-D image was formed of a center focused spot with a FWHM of 100-200 μm , and intensity patterns over the balance of the CCD area (6 x 4 mm) which were termed side patterns. The side patterns were dependent on the PS design and the light spectrum. The side pattern formation can be explained and predicted by plotting the characteristic light rays through photon sieves. The high background noise (bright side patterns) observed under

polychromatic white light was caused by the higher order diffraction, undiffracted light rays, and the light rays diffracted through the non-designed pinholes.

For dual-wavelength PSs, the pinholes located near the central zone lead to higher intensity of the focal spot without degrading the FWHM. This was attributed to the fact that light rays diffracted and focused by the pinholes near the central zone are mainly from lower order diffraction, which exhibit stronger intensity than those higher order diffraction from outlying pinholes.

The FWHM measurements demonstrated that the dual-wavelength PSs focus a lower intensity as compared to single-wavelength PSs under either the monochromatic or polychromatic light spectra. However, the single-wavelength PSs were not able to focus the light rays at the non-designed wavelength, while the dual-wavelength PSs were able to focus both monochromatic wavelengths with low intensity. The property of high dispersion of a single-wavelength PS for non-designed wavelengths would make it a good candidate for a focusing filter for polychromatic light. Dual-wavelength PSs can be used for the imaging device that requires filtering of polychromatic light at two wavelengths at the cost of lower intensity.

The FWHM data also showed that the focus of sectional designed PSs were broader and less intense than from concentric designed dual-wavelength PSs.

CHAPTER 5 CONCLUSIONS

5.1 Photon Sieve Fabrication

Four process methods of photon sieve fabrication were developed and tested as summarized below. The first method, reversed image etching, was successful but complicated. It required deposition of a chromium film over the Ag film and more than 40 minutes of high-power reactive ion etching (RIE) of silver, which makes this process more time consuming than the other methods. In addition, formation of residual dots within the open holes of the photon sieves was observed. It is speculated that the residual dots were formed by the primary metals/hydrocarbon particles agglomerating during plasma etching. Contamination from chamber build-up, re-deposited metal atoms, and polymer formed from CH_4/H_2 radicals are possible sources of primary particles. More experiments are needed to verify this speculation about the mechanism for residual dots formation during reversed image etching.

To simplify the process flow and avoid the possibility of residual dots formation, a second method, the lift-off method, was developed. However, the deposited silver atoms stuck on the sidewalls of the patterned resist and limited the deposition thickness of silver.

To avoid the problem of sidewall deposits and the use of unstable oxygen plasmas in the reactive ion etching (RIE) system, a third method, the direct wet etching method, was studied. The direct wet etching method was simple and fast. However, non-uniform etching rates for different feature sizes resulted in a poor quality of the photon sieves.

The fourth method, the direct dry etching method, was developed to solve the non-uniform aqueous etching problems. PMMA was shown to be a poor mask for argon sputter etching due to deposits of residual contaminants at the edge of holes. A positive electron beam resist, ZEP700, was used to cover the PMMA because of its excellent resistance to dry etching. The direct dry etching method using the ZEP7000 plus PMMA resulted in the most successful process method in terms of simplicity and repeatability for the production of photon sieves.

5.2 Photon Sieve (PS) Properties

Single- and dual-wavelength photon sieves (PSs) were designed and tested in this research project. Based on simulations of the PS properties, the diameter was fixed at 3 mm, designed focal length at 50 mm, K factor (the ratio of the hole separation to hole diameter) was set at 1.2, and all the photon sieves were apodized by a modified Gaussian function. PSs were fabricated having hole sizes and spacing appropriate to focus either 500 or 600 nm light, and dual wavelength PSs were created by mixing the holes for each wavelength in a sector, concentric or random pattern. The PS sieves were tested in a modified Perkin-Elmer 16U grating spectrometer with a WinCamD CCD camera.

The PSs were tested for focal length, FWHM and maximum intensity of the image of a 100 μm point source either monochromatic 500 or 600 nm light, or polychromatic white light from a tungsten halogen lamp. The focal length data show that a clear focal spot was formed with a focal length of 51.7 ± 1 mm when monochromatic 500 or 600 nm light passed through the PSs with pinholes designed for 500 nm or 600 nm, respectively. When 600 nm light passed through the PS with pinholes designed for 500 nm, the best image of the point source was formed at a focal length of 42.4 ± 1 mm. For 500 nm light

through PS with pinholes designed for 600 nm, the focal length was greater than 59.5 mm.

The measured focal length has a 3% variation of the designed focal length (50 mm). This variation may be caused either by the slightly different wavefront shapes (planar versus spherical) or by the inconsistency of the substrate refraction between simulation and measurement. From the result of focal length characterization, the longitudinal chromatic aberration was 9.3 mm for 100 nm wavelength differences, resulting in defocused images of the point source at a focal plane of 51.7 mm. The experiment data is consistent with the theoretical calculation for the focal length shifting.

When the CCD camera was placed at the measured focal length of 51.7 mm, a 2-D image was formed of a center focused spot with a FWHM of 100-200 μm , and intensity patterns over the balance of the CCD area (6 x 4 mm) which were termed side patterns. The side patterns were dependent on the PS design and the light spectrum. The side pattern formation can be explained and predicted by plotting the characteristic light rays through photon sieves. The high background noise (bright side patterns) observed under polychromatic white light was caused by the higher order diffraction, undiffracted light, and the light rays diffracted through the non-designed pinholes.

For dual-wavelength PSs, the pinholes located near the central zone lead to higher intensity of the focal spot without degrading the FWHM. This was attributed to the fact that light rays diffracted and focused by the pinholes near the central zone are mainly from lower order diffraction, which exhibit stronger intensity than those higher order diffraction from outlying pinholes.

The FWHM measurements demonstrated that the dual-wavelength PSs focus a lower intensity as compared to single-wavelength PSs under either the monochromatic or polychromatic light spectra. However, the single-wavelength PSs were not able to focus the light rays at the non-designed wavelength, while the dual-wavelength PSs were able to focus both monochromatic wavelengths with low intensity. The property of high dispersion of a single-wavelength PS for non-designed wavelengths would make it a good candidate for a focusing filter for polychromatic light. Dual-wavelength PSs can be used for the imaging device that requires filtering of polychromatic light at two wavelengths at the cost of lower intensity.

The FWHM data also showed that the focus of sectional designed PSs were broader and less intense than from concentric designed dual-wavelength PSs.

CHAPTER 6 FUTURE WORKS

There were some speculative explanations of some of the experiment results in this research that require further study. An example is the mechanism of silver etching with the proprietary RIE recipe [68]. It was speculated that silver organometallic complexes were formed. This should be verified by in-situ analysis with proper instruments, such as mass spectroscopy. Second, the charging problem in Auger analysis for the residual dots observed during the reversed image etching process can be solved by terminating the etching near the half way point, where the silver film is not completely etched. The remaining silver film on the top of glass substrate would serve as a charge dissipation path, which should make the Auger analysis on the surface of a single dot more reliable.

With respect to the properties of the 3% difference between the designed and measured focal length may be caused either by the slightly different wavefront shapes (planar versus spherical) or by the inconsistency of the substrate refraction between simulation and measurement. This could be verified by either modifying the simulation equations or adjusting the optical bench set up to create a planar wave source. The effect of the substrate refraction could be verified by testing the sample from both sides. It is also important to quantify the various source of the background noise (undiffracted light, higher order diffraction, etc.). This will allow a better understanding of the complicated diffraction behaviors of photon sieves.

The question of why sectional designed PSs are inferior to concentric designed dual-wavelength PSs remains unanswered. The major difference between the sectional

and concentric designs is the symmetry of pinholes distribution. This may be a hint to the answer of this question. In addition, in this research, the effect of theoretical resolution ($10\ \mu\text{m}$) of the photon sieves was not observed and probably was due to the large point source ($100\ \mu\text{m}$) with a finite distance and the large pixel ($9.3\ \mu\text{m}$) of the CCD camera. Further studies would be necessary to solve these questions

It would be very useful to test the photon sieves with imaging. Comparing the PSFs with photographs taken with refractive lenses would help to understand the image formation by the photon sieves. It would be very interesting to further investigate the performance of a single-wavelength photon sieve as a focusing filter in an imaging system.

LIST OF REFERENCES

1. Chao, W., Anderson, E., Denbeaux, G. P., Harteneck, B., Kiddle, J. A., Olynick, D. L., Pearson, A. L., Salmassi, F., Song, C. Y., and Attwood, D. T. (2003). 20-nm-resolution soft x-ray microscopy demonstrated by use of multilayer test structures:erratum. *Opt. Lett.*, 28, 2530.
2. Gil, D., Menon R., and Smith, H. I. (2003). The case for diffractive optics in maskless lithography. *J. Vac. Sci. Technol. B*, 21, 2810-2814.
3. Kipp, L., Skibowski, M., Johnson, R. L., Berndt, R., Adelung, R., Harm, S., and Seemann, R. (2001). Sharper images by focusing soft X-ray with photon sieves. *Nature*, 414, 184-188.
4. Kato, M., Maeda, S., Yamagishi, F., Ikeda, H., and Inagaki, T. (1989). Wavelength independent grating lens system. *Applied Optics*, 28(4), 682-686.
5. Ferriere, R., and Goedgebuer, J. P. (1983). Achromatic system for far-field diffraction with broadband illumination. *Applied Optics*, 22(10), 1540-1545.
6. Bennett, S. J. (1976). Achromatic combinations of hologram optical elements. *Applied Optics*, 15(2), 542-545.
7. Pedrotti, F. L., and Pedrotti, L. S. (1992). *Introduction to optics*. (pp. 30-36). Englewood Cliffs: Prentice-Hall.
8. Meyer-Arendt, J. R. (1989). *Introduction to classical and modern optics*. (pp. 247-269). Englewood Cliffs: Prentice-Hall.
9. Hecht, E. (2002). *Optics*. (pp. 443-446). San Francisco: Addison Wesley.
10. Wikipedia. (n.d.). Diffraction. Retrieved October 19, 2005, from Wikipedia. Web site: <http://en.wikipedia.org/wiki/Diffraction>
11. MathPages. (n.d.). Huygens' principle. Retrieved October 10, 2005, from MathPages, Physics. Web site: <http://www.mathpages.com/home/iphysics.htm>
12. O'Connor, J. J. and Robertson, E. F. (2002). Gustav Robert Kirchhoff biography. Retrieved October 20, 2005, from TURNBULL WWW server, U. of St. Andrew, UK. Web site: <http://www-groups.dcs.st-and.ac.uk/~history/Mathematicians/Kirchhoff.html>

13. Nave, C. R. (2005). Fraunhofer diffraction geometry. Retrieved October 23, 2005, from HyperPhysics, Georgia State U. Web site: <http://hyperphysics.phy-astr.gsu.edu/hbase/phyopt/sindoub.html#c1>
14. Nave, C. R. (2005). Circular aperture diffraction. Retrieved October 23, 2005, from HyperPhysics, Georgia State U. Web site: <http://hyperphysics.phy-astr.gsu.edu/hbase/phyopt/cirapp2.html>
15. Weisstein, E. W. (1999). Bessel function of the first kind. Retrieved October 24, 2005, from MathWorld, A Wolfram web resource. Web site: <http://mathworld.wolfram.com/BesselFunctionoftheFirstKind.html>
16. Nave, C. R. (2005). Comparison: Fraunhofer and Fresnel slit. Retrieved October 25, 2005, from HyperPhysics, Georgia State U. Web site: <http://hyperphysics.phy-astr.gsu.edu/hbase/phyopt/fresli.html#c2>
17. Weisstein, E. W. (1999). Fresnel number. Retrieved November 1, 2005, from MathWorld, A Wolfram web resource. Web site: <http://scienceworld.wolfram.com/physics/FresnelNumber.html>
18. Fabrizio, E., Romanato, F., Gentili, M., Cabrini, S., Kaulich, B., Susini, J., and Barrett, R. (1999). High-efficiency multilevel zone plates for keV X-rays. *Nature*, *401*, 895-898.
19. Cao, Q., and Jahns, J. (2003). Modified Fresnel zone plates that produce sharp Gaussian focal spots. *J. Opt. Soc. Am. A*, *20*(8), 1576-1581.
20. Kipp, L. (2002). Focusing soft X-ray with photon sieves. Retrieved November 20, 2005, from U. of Kiel, Germany. Web site: <http://www.photonsieve.de/home.htm>
21. Kriz, J. (1974). Phase zone plate for X-ray and the extreme UV. *J. Opt. Soc. Amer.* *64*, 301.
22. Schelokov, I. A., Roshchupkin, D. V., Kondakov, A. S., Irzhak, D. V., Brunel, M., and Tucoulou, R. (1999). Second generation of grazing-incidence-phase Fresnel zone plates. *Optics Communications*, *159*, 278-284.
23. Morgan, B., Waits, C. M., Krizmanic, J., and Ghodssi, R. (2004). Development of a deep silicon phase Fresnel lens using gray-scale lithography and deep reactive ion etching. *J. of MEMS*, *13*(1), 113-120.
24. Yasumoto, M., Tamura, S., Kamijo, N., Suzuki, Y., Awaji, M., Takeuchi, A., and Takano, H. (2003). Sputtered-sliced fabrication of kinoform zone plate for hard X-ray focusing. *J. Phys. IV France*, *104*, 189-192.

25. Pelka, D. (2003, October). Kinoform-based diffusers help lighting designers leverage unique LED advantages. Retrieved December 2, 2005, from SPIE's oe magazine database. Web site: <http://oemagazine.com/fromTheMagazine/oct03/kinoforms.html>
26. Lesem, L. B., Hirsch, P. M., and Jordan, J. A. (1969). The kinoform: A new wavefront reconstruction device. *IBM J. Res. Develop.*, 13(2), 150-155.
27. Horan, P. (2005). T222/4 Applied optics, module 7: diffractive optical elements lenses. Retrived November 13, 2005, from Resources and downloads, DIT School of Physics, Ireland. Web site: <http://physics.dit.ie/resources/physicstech4/optics/module%207%20B&W.ppt>
28. Cao, Q., and Jahns, J. (2002). Focusing analysis of the pinhole photon sieve: Individual far-field model. *J. Opt. Soc. Am. A*, 19(12), 2387-2393.
29. Cao, Q., and Jahns, J. (2003). Nonparaxial model for the focusing of high-numerical-aperture photon sieves. *J. Opt. Soc. Am. A*, 20(6), 1005-1012.
30. Weisstein, E. W. (1999). Paraxial approximation. Retrieved November 25, 2005, from MathWorld, A Wolfram web resource. Web site: <http://scienceworld.wolfram.com/physics/ParaxialApproximation.html>
31. Pfeifer, D. C., and Ferris, L. D. (1973). Optical image formation with a Fresnel zone plate using vacuum-ultraviolet radiation. *J. Opt. Soc. Amer.*, 63, 91.
32. Niemann, B., Rudolph, D., and Schmahl, G. (1974). Soft X-ray imaging zone plate with large zone numbers for microscopic and spectroscopic applications. *Opt. Comm.*, 12, 160.
33. Wikipedia. (n.d.). Gaussian blur. Retrieved December 19, 2005, from Wikipedia. Web site: http://en.wikipedia.org/wiki/Gaussian_blur
34. Graham, D. T., and Cloke, P. (2003). *Principles of radiological physics*. Churchill Livingstone: Elsevier.
35. Menon, R., Gil, D., Barbastathis, G., and Smith, H. I. (2005). Photon-sieve lithography. *J. Opt. Soc. Am. A*, 22(2), 342-345.
36. Engel, A., and Herziger, G. (1973). Computer-drawn modulated zone plate. *Applied Optics*, 12(3), 471-479.
37. Amie, C., Soummer, R., and Ferrari, A. (2001). Interferometric apodization of rectangular apertures – application to stellar coronagraphy. *A & A*, 379, 697-707.
38. Wang, H., and Gan, F. (2002). Phase-shifting apodizers for increasing focal length. *Applied Optics*, 41(25), 5263-5266.

39. Kasdin, N. J., Vanderbei, R. J., Littman, M. G., and Spergel, D. N. (2005). Optimal one-dimensional apodizations and shaped pupils for planet finding coronagraphy. *Applied Optics*, 44(7), 1117-1128.
40. Gao, X., Fei, Z., Xu, W., and Gan, F. (2005). Tunable three-dimensional intensity distribution by a pure phase-shifting apodizer. *Applied Optics*, 44(23), 4870-4873.
41. Ledesma, S., Campos, J., Escalera, J. C., and Yzuel, M. J. (2004). Symmetry properties with pupil phase-filters. *Optics Express*, 12(11), 2548-2559.
42. Weisstein, E. W. (1996). Apodization. Retrieved November 11, 2005, from Eric Weisstein's home page, Thesis: Millimeter/submillimeter fourier transform spectroscopy of jovian planet atmospheres. Web site: <http://www.ericweisstein.com/research/thesis/node37.html>
43. Shenderova, O. (2005). Multicolor photon sieves: number of sectors and symmetry of paraxial point spread function. Private project report. International Technology Center, N. Carolina.
44. Shenderova, O. (2004, October). Photon sieves simulation – I. Presentation for private internal project review. International Technology Center, N. Carolina.
45. Shenderova, O. (2004, February). Photon sieves simulation – II. Presentation for private internal project review. International Technology Center, N. Carolina.
46. Smith, H. I. (1996). A proposal for maskless, zone-plate-array nanolithography. *J. Vac. Sci. Technol. B*, 14, 4318-4322.
47. Wikipedia. (n.d.). Chromatic aberration. Retrieved December 19, 2005, from Wikipedia. Web site: http://en.wikipedia.org/wiki/Chromatic_aberration
48. S. Mahajan and Sree Harsha, K. S. (1999). *Principles of growth and processing of semiconductors*. (pp. 408-480). Singapore: McGraw-Hill.
49. O'Hanlon, J. F. (1989). *A user's guide to vacuum technology*. New York: JohnWiley & Sons.
50. DeVoe, D. (2002, spring). Thin film deposition. Retrived November 21, 2005, from ENME 489F Course intruction, Dept. of Mech. Eng., U. of Maryland. Web site: http://www.glue.umd.edu/~ddev/me489f/slides/2b_deposition_x6.pdf
51. Cotronakis, J., Clarke, M., Lawrence, R., Campbell, J., and Gaw, C. (2004). Continuous defectivity improvements and impact on high-density metal-insulator-metal (HDMIM) capacitor yields. Retrieved November 23, 2005, from International Conf. on Compound Semiconductor Technology, On-line digest, 2004. Web site: <http://www.gaasmantech.org/Digests/2004/2004Papers/12.3.pdf>

52. Mattox, D. M. (2001). Educational guide to vacuum coating processing. Retrieved November 18, 2005, from SVC Educational Program. Web site: http://www.svc.org/EP/EP_FeatureGuide.html
53. Ash, G. (2005) Cryogenic high vacuum pump. Retrieved October 29, 2005, from Brookes Automation technology articles. Web site: <http://www.helixtechnology.com/technology/page81.html>
54. Operation manual for Inficon deposition controller XTC/2. Inficon Corp.
55. Miller, J. G., and Bolef, D. I. (1968). Sensitivity enhancement by the use of acoustic resonators in cw ultrasonic spectroscopy. *J. Appl. Phys.*, 39, 4589-4593.
56. Miller, J. G., and Bolef, D. I. (1968). Acoustic wave analysis of the operation of quartz-crystal film-thickness monitors. *J. Appl. Phys.*, 39, 5815-5816.
57. Lu, C. S., and Lewis, O. (1972). Investigation of film-thickness determination by oscillating quartz resonators with large mass load. *J. Appl. Phys.*, 43, 4385-4390.
58. Inficon (2004). Thin film deposition controllers and monitors. Retrieved November 16, 2005, from Inficon: product listing. Web site: <http://www.inficon.com/download/en/Thin%20Film%20Family%20Brochure%2012-04.pdf>
59. Conway, J. (2005). E-beam lithography resist processing. Retrieved November 22, 2005, from Stanford Nanofabrication Facilities: Process, Stanford University. Web site: <http://snf.stanford.edu/Process/Lithography/ebeamres.html>
60. Dow Corning (2002). FOX (R)-14 flowable oxides. Retrieved: November 21, 2005, from Dow Corning: Product list. Web site: http://www.dowcorning.com/applications/product_finder/pf_details.asp?l1=009&pg=00000037&prod=02334917&type=PROD
61. Zeon Chemicals. (n.d.). ZEP7000 technical report and ZEP7000 info sheet. Retrieved November 20, 2005, from Zeon Chemicals: Products. Web site: <http://www.zeonchemicals.com/productgrade.asp?id=234>
62. Birnie, D. P. (1997). Combined flow and evaporation during spin coating of complex solutions. *Journal of Non-Crystalline Solids*, 218, 174-178.
63. Haas, D. E., and Birnie, D. P. (2001). Real-time monitoring of striation development during spin-on-glass deposition. In X. Feng, L.C. Klein, E.J.A. Pope, and S. Komarneni (Ed.), *Sol-Gel Commercialization and Applications*. (pp. 133-138). Westerville: Amer Ceramic Society.
64. Birnie, D. P. (2000). Coating quality and spin coating. Retrieved December 1, 2005, from Dept. of MSE, U. of Arizona. Web site: <http://www.mse.arizona.edu/faculty/birnie/Coatings/index.htm>

65. Ghandhi, S. K. (1994). *VLSI fabrication principles – silicon and gallium arsenide*. New York: John Wiley & Sons.
66. Brubaker, C. (2004, November 11). Oven/hot plate bake. mems-talk. Retrieved December 3, 2005, from memsnet.org. Message posted to: <http://mail.mems-exchange.org/pipermail/mems-talk/2004-November/014370.html>
67. Georgia Insititute of Technology. (n.d.). MSDS of Microposit MF-322 developer. Retrieved November 27, 2005, from Microelectronics Research Center, Georgia Insititute of Technology. Web site: <http://groverc.mirc.gatech.edu/data/msds/273.html>
68. VI Microsystem Inc. (2003). *Proprietary etching recipe (patent pending)*. VI Microsystem Inc, Gainesville, FL.
69. Yacobi, B. G., and Holt, D. B. (1990). *Cathodoluminescence microscopy of inorganic solids*. New York: Plenum Press.
70. Brundle, C. R., Evans, C. A., and Wilson, S. (1992). *Encyclopedia of materials characterization*. Boston: Butterworth-Heinemann.
71. Miessler, G. L., and Tarr, D. A. (1990). *Inorganic chemistry*. Englewood Cliffs: Prentice-Hall.
72. Denk, M. K. (2005). Polar organometallic compound. Retrieved December 14, 2005, from Denk group: Lecture: Chem 462, University of Guelph, Canada. Web site: http://131.104.156.23/Lectures/CHEM_462/462_Alkali.html
73. Wang, K., Zhang, W., Xian, M., Hou, Y. C., Chen, X. C., Cheng, J. P., and Wang, P. G. (2000). New chemical and biological aspects of S-Nitrosothiols. *Current Medicinal Chemistry*, 7(8), 821-834.
74. Yoo, W. J., and Steinbruchel, C. (1992). Kinetics of particle formation in the sputtering and reactive ion etching. *J. Vac. Sci. Technol. A*, 10(4), 1041-1047.
75. Boufendi, L., Hermann, J., Bouchoule, A., Dubreuil, B., Stoffels, E., Stoffels, W. W., and de Giorgi, M. L. (1994). Study of initial dust formation in an Ar-SiH₄ discharge by laser induced particle explosive evaporation. *J. Apl. Phys.*, 76(1), 148-153.
76. Setyawan, H., Shimada, M., Hayashi, Y., Okuyama, K., and Yokoyama, S. (2004). Particle formation and trapping behavior in a TEOS/O₂ plasma and their effects on contamination of a Si wafer. *Aerosol Science and Technology*, 38, 120-127.
77. Moriya, T., Nakayama, H., Nagaike, H., Kobayashi, Y., Shimada, M., and Okuyama, K. (2005). Particle reduction and control in plasma etching equipment. *IEEE Transactions on Semiconductor Manufacturing*, 18(4), 477-486.

78. Stark, C. (1997). Matlab summary and tutorial. Retrieved December 5, 2005, from Dept. of Mathematics, University of Florida. Web site: <http://www.math.ufl.edu/help/matlab-tutorial/>
79. Curtin, D. P. (2006). Image sensors. Retrieved November 18, 2005, from The Home of Short Courses Publishing Company. Web site: <http://www.shortcourses.com/choosing/sensors/05.htm#Types%20of%20image%20sensors>
80. Data Ray Inc. (2002). *User manual for WinCamD CCD beam imager*. Boulder Creek: DataRay Inc.
81. Cooper, A. (1996). CCD problems. Retrieved December 15, 2005, from Silicon Owl. Web site: <http://www.siowl.com/index.html?CCDproblems/CCDProblems.html>
82. Tucker, R. (2001). Damage threshold for over illumination. Retrieved December 18, 2005, from CCD-world. Web site: <http://www.ctio.noao.edu/pipermail/ccd-world/2001/000502.html>

BIOGRAPHICAL SKETCH

Hsiu-hsin Chung was born in Taiwan. She obtained her BS degree in chemistry at National Tsing-Hua University, Hsinchu, Taiwan, in 1994. After worked as a packaging engineer for four years, she enrolled at San Jose State University and received her MS degree in materials engineering in 2004. While she was studying at San Jose State University, she worked as a co-op in the Packaging Technology Group in the National Semiconductor Corporation for over 2 years. She was admitted to the University of Florida, Department of Materials Science and Engineering, in 2001 and obtained her Ph.D. in 2006. She is a recipient of three FLAVS student poster awards (2003-2005) and she holds two US patents (1998).